



Delft University of Technology



Non-linear FEM modelling of steel fibre reinforced concrete

*for the analysis of tunnel segments in the thrust
jack phase*

Main Report

September 2006
Author: Remko Burgers

Author:

Remko Burgers

Study number: 1142747

Delft University of Technology

Faculty of Civil Engineering and Geosciences

Master Structural Engineering

Concrete Structures

Stevinweg 1, Delft, Netherlands

Master thesis committee:

Prof.dr.ir. J.C. Walraven

Dr.ir. C.B.M. Blom

Ir. W.J.M Peperkamp

Dr.ir. P.C.J. Hoogenboom

Ir. L.J.M. Houben

Prof. G.A. Plizzari

Delft University of Technology

Delft University of Technology/ Gemeentewerken Rotterdam

Delft University of Technology

Delft University of Technology

Delft University of Technology

Brescia University

Preface

This document is the thesis I have made to obtain my master's degree in Civil Engineering at the Delft University of Technology. This study has been carried out for the mayor part at the Brescia University in Italy. In this thesis the performance of crack models in FEM programs is studied and non-linear crack modelling is applied on steel fibre reinforced tunnel segments under thrust jack action.

The master thesis committee consists of the following members:

Prof.dr.ir. J.C. Walraven	Delft University of Technology
Dr.ir. C.B.M. Blom	Gemeentewerken Rotterdam
Ir. W.J.M Peperkamp	Delft University of Technology
Dr. ir. P.C.J. Hoogenboom	Delft University of Technology
Ir. L.J.M. Houben	Delft University of Technology
Prof. G.A. Plizzari	Brescia University

I would like to thank Brescia University to give me the opportunity to study at their university. My gratitude goes to my committee and in particular Giuseppe Tiberti for his great support during my stay in Brescia.

Furthermore, I would like to thank the students of the Brescia University who have made me feel at home in Italy by showing a great hospitality. They have become great friends for me.

Finally I tank my family and friends for their help and understanding.

Delft, September 2006

Remko Burgers

Summary

In general, several cracks appear during the assembly phase of shield driven tunnels. These cracks are undesirable, so one tries to find solutions to reduce the number of cracks and the crack widths. Steel Fibre Reinforced Concrete has favourable properties when it comes to cracking of concrete. The steel fibres reduce crack widths and crack developments in cracked zones of structures. The first aim of this thesis is to study the influence of steel fibres in the application in tunnel segments. The Barcelona line 9 metro tunnel is taken as example project.

The above mentioned goal is reached by FEM simulations of a tunnel segment with the FEM program DIANA. To study crack development, it is necessary to use a non-linear material model to describe the occurring cracks. When, as a test, the same simulation was done with two different FEM programs (ABAQUS and DIANA) with two generally accepted material models, the results were completely different. There are several non-linear material models, but it is not always easy to understand how they function and for which applications they can be used in the field of research on concrete structures. In order to make the non-linear simulations of the tunnel segment and concrete structures in general with a reliable model, the functioning and numerical stability of the available DIANA models and the earlier applied ABAQUS model is studied.

Firstly, the background of the material models is studied in order to gain insight in how they function, theoretically. From the theoretical background is derived how they approach the real behaviour of concrete and in which field of application they can be used. Secondly, the material models are tested by simulating three experimental tests: a four point bending test, which describes the uni-axial tensile behaviour, a splitting test with a line load, which describes a bi-axial stress state and a splitting test with a point load, which describes a tri-axial stress state. The studied models are the Total Strain rotating crack, Total Strain fixed crack and Drucker/Prager + multi directional fixed crack of DIANA and Concrete Damaged Plasticity of ABAQUS.

The DIANA models are all crack models with orthotropic softening, which means they show softening in the direction perpendicular to the crack and not in the directions in plane with the crack. These models are, theoretically, suitable to model concrete cracking in a multi-axial stress state. Instead, the ABAQUS model (Concrete Damaged Plasticity) has isotropic softening, so after cracking the stiffness reduces in all directions. This property makes this model only suitable for crack modelling in a uni-axial stress state and not for a multi-axial stress state. From the experimental tests it becomes clear that the Total Strain fixed crack and the Drucker/Prager + multi directional fixed crack model are numerically unstable or give bad approximations due to the requirement of the reimplementation of the shear modulus. The Total Strain rotating crack model is the most suitable for the simulations in this thesis and will be used for the analyses on the tunnel segment. The limitation of this model is the rotating crack mechanism, which makes the model not suitable for phased analyses.

When the situation of the Barcelona line 9 metro tunnel is simulated, some cracks which have been observed in practice can be reproduced in DIANA. The cracks are caused by eccentricity or inclination of the thrust jacks in radial direction or non-smoothness of the ring joint. With an equal load, the crack widths reduce significantly with an increased amount of steel fibres. In particular when high amounts of steel fibres are applied, the addition of extra steel fibres has a relatively large influence on the crack widths. When more than 45 kg/m³ fibres is applied, the ultimate load is caused by reaching the compressive strength, so adding more steel fibres does not influence the ultimate load. Another way to reduce the splitting

cracks is to change the thrust jack configuration. The Japanese configuration shows significantly smaller cracks, but is sensitive for a non-smooth support in the ring joint. The French configuration is not sensitive for the latter case, but displays larger splitting cracks.

Samenvatting

Er treden over het algemeen veel scheuren op in boortunnel segmenten tijdens de montage fase. Deze scheuren zijn onwenselijk, dus men zoekt naar methoden om het aantal scheuren en de scheurwijdte terug te dringen. Staalvezelbeton heeft gunstige eigenschappen met betrekking tot het nascheur gedrag van beton. De staal vezels reduceren de scheurwijdtes en scheurontwikkeling in gescheurde zones. Het eerste doel van deze studie is het bestuderen van de invloed van staal vezels bij het toepassen in tunnel segmenten. De Barcelona lijn 9 metro tunnel wordt hierbij als voorbeeld project gebruikt.

Het bovengenoemde doel wordt bereikt met behulp van eindige elementen berekeningen met het programma DIANA. Om de scheurontwikkeling te kunnen bestuderen is het nodig om een niet-lineair materiaalmodel te gebruiken. Wanneer twee verschillende, algemeen geaccepteerde materiaalmodellen van twee verschillende EEM programma's (DIANA en ABAQUS) met elkaar worden vergeleken door middel van het uitvoeren van dezelfde simulatie, blijken de resultaten ver uit elkaar te liggen. Er zijn veel verschillende materiaal modellen voor het beschrijven van scheuren in beton, maar deze zijn niet altijd even gemakkelijk te begrijpen hoe ze werken en voor welke toepassingen ze geschikt zijn. Om niet-lineaire simulaties van het segment model (en andere betonconstructies) te kunnen maken met een betrouwbaar model, wordt een studie gedaan naar de werking en de numerieke stabiliteit van de DIANA modellen en van het eerder toegepaste ABAQUS model.

In eerste instantie worden de achtergronden van de verschillende materiaalmodellen bestudeerd om inzicht te krijgen hoe ze in theorie functioneren. Van de theoretische achtergrond kan worden afgeleid hoe ze het gedrag van beton simuleren en voor welke toepassingen ze geschikt zijn. Daarna worden de materiaalmodellen getest door drie experimentele testen te simuleren: een vier punts buig test, welke het één-assige trek gedrag simuleert, een splijt test met lijn belasting, welke het twee-assige gedrag simuleert en een splijtttest met punt last, om het drie-assige gedrag simuleert. De geteste modellen zijn het Total Strain rotating crack model, het Total Strain fixed crack model en het Drucker/Prager + multi directionaal fixed crack model van DIANA en het Concrete Damaged Plasticity model van ABAQUS.

Alle DIANA modellen zijn scheur modellen met orthotrope softening. Dit betekent dat softening intreedt in de richting loodrecht op de scheur en niet in de richtingen in het vlak van de scheur. Deze modellen zijn in theorie in staat het meer-assige gedrag van scheurvorming in beton te simuleren. Het Concrete Damaged Plasticity mode van ABQUS daarentegen heeft isotrope softening. Het gevolg hiervan is dat softening intreedt in alle richtingen tegelijk in dezelfde mate. Hierdoor is dit model enkel toe te passen voor het modelleren van een één-assige spanningstoestand. Uit de simulaties van de experimenten blijkt dat het Total Strain fixed crack model en het Drucker/Prager + multi directionaal fixed crack model numeriek instabiel zijn of slechte benaderingen geven door herinvoering van de schuifmodulus. Het Total Strain rotating crack model is het meest geschikt voor de simulaties in dit verslag en zal dus worden gebruikt voor de analyses van het tunnel segment. De beperking van dit model is het mechanisme dat de scheur meedraait met de hoofdspansingen. Dit maakt het model ongeschikt voor simulaties met gefaseerde belastingen.

De simulaties van de Barcelona lijn 9 metro tunnel laten scheuren zien die vergelijkbaar zijn met in de praktijk geconstateerde scheuren. Deze scheuren worden veroorzaakt door het excentrisch of onder een hoek plaatsen van de vijzel op het segment in radiale richting of het optreden van een onvlakke ringvoeg. Met gelijkblijvende belasting wordt de scheurwijdte

veel kleiner wanneer de hoeveelheid staalvezels wordt vergroot. Vooral bij hoge hoeveelheden staalvezels zorgen extra staalvezels voor een relatief grote reductie van de scheurwijdtes. Wanneer meer dan 45 kg/m³ staal vezels wordt toegepast, wordt de bezwijkbelasting gelimiteerd door de druksterkte van het beton. Het toevoegen van vezels heeft hierbij dus geen invloed meer op de bezwijkbelasting. Een andere manier om de scheurwijdtes te beperken is het veranderen van de vitzelconfiguratie. De Japanse configuratie heeft kleine scheurwijdtes in de normale belastingsituatie, maar is gevoelig voor een niet-vlakke ringvoeg oplegging. De Franse configuratie is niet gevoelig voor dat laatste, maar heeft grotere slijtscheuren, omdat de belasting meer geconcentreerd wordt geplaatst.

Table of Contents

Preface	III
Summary	V
Samenvatting	VII
Table of Contents	XI
1 Introduction	1
2 Barcelona line 9 metro tunnel	5
3 Material properties	7
3.1 Material properties according to EuroCode 2	7
3.1.1 Mix design.....	7
3.1.2 Material properties	8
3.1.3 Compressive behaviour	9
3.2 Post cracking behaviour	10
4 Models of the tunnel segment	15
4.1 Models based on four separate thrust jacks.....	15
4.1.1 Imported ABAQUS model.....	15
4.1.2 DIANA model.....	17
4.2 Model based on two pairs of thrust jacks	18
5 Validation of the models.....	19
6 Modelling of SFRC in a FEM program	23
6.1 Discrete crack models.....	23
6.2 Implementation of the material behaviour	23
6.3 Smearred crack models.....	25
6.3.1 Principle of smeared cracking	25
6.3.2 Total Strain crack models	26
6.3.3 Drucker/Prager – Multi directional fixed crack	28
6.4 Damage models.....	29
6.4.1 Concrete Damaged Plasticity	29
7 Simulation of experimental tests.....	33
7.1 Four point bending test on a notched beam	33
7.1.1 Total strain rotating crack.....	34
7.1.2 Total strain fixed crack	35
7.1.3 Drucker/Prager – Multi directional fixed crack	37
7.1.4 Concrete Damaged Plasticity – ABAQUS model	37
7.2 Splitting test with line load	38
7.2.1 Total strain rotating crack.....	41
7.2.2 Drucker/Prager + Multi directional fixed crack	42
7.2.3 Total strain fixed crack.....	43
7.2.4 Concrete Damaged Plasticity	43
7.3 Splitting test with point load	44
7.4 Conclusions with respect to the material models.....	50
8 Calibration of the model	53
8.1 Choice of the element type.....	53
8.2 Choice of the boundary conditions	56
8.2.1 Support of the ring joint in z-direction	56
8.2.2 Support of the ring joint in lateral direction	57
8.2.3 Support of the lateral joint.....	57
9 Simulation of the thrust jack forces in the Barcelona line 9 metro tunnel	59
9.1 Introduction	59
9.2 The normal loading situation.....	60
9.3 Eccentricity of the thrust jack	67

9.3.1	Eccentricity outside	68
9.3.2	Eccentricity inside	72
9.4	Inclination between segment and the thrust jack.....	76
9.4.1	Inclination outside.....	77
9.4.2	Inclination inside.....	80
9.5	Non-smooth support of the ring joint.....	82
9.5.1	Missing support in the middle of the segment.....	83
9.5.2	Missing support on the side of the segment	86
10	Influence of the material properties	91
10.1	Different amounts of FF1 steel fibres	91
10.2	Ultra high performance concrete	96
11	Alternative thrust jack configurations.....	101
11.1	Japanese thrust jack configuration	102
11.1.1	The normal loading situation	102
11.1.2	Missing support at the side of the segment	104
11.2	The French thrust jack configuration.....	105
11.2.1	The normal loading situation	105
11.2.2	Eccentricity or inclination of the thrust jack.....	107
11.3	Conclusions with respect to the segment analyses	110
11.3.1	Conclusions with respect to the application of SFRC in tunnel segments...	110
11.3.2	Conclusions with respect to the thrust jack configuration.....	110
12	General conclusions and future perspectives	111
12.1	Conclusions	111
12.2	Future perspectives	113
	Literature.....	115

1 Introduction

There are several ways to build an underground structure. Normally open methods, like the cut and cover method, are applied, because they are cheap and there is a lot of experience with these methods. Nowadays, the Netherlands is densely populated and wherever an underground structure is built, there is hindrance to the environment. This hindrance is minimised when shield tunnelling is applied. This method is in general more expensive than open methods, but the fact that the environment does not experience any hindrance during the building process, makes it an attractive alternative.

As described in the Literature Survey, there are different loading situations in the service condition and in the building phase. During the building phase, the thrust jack forces and the grout pressure are the most critical factors. Cracks appear often in the tunnel lining in the phase in which these forces occur. Some examples of often occurring cracks which have been observed in the Barcelona line 9 metro tunnel are given below. The locations of the cracks are displayed by the small drawings, which support the pictures.

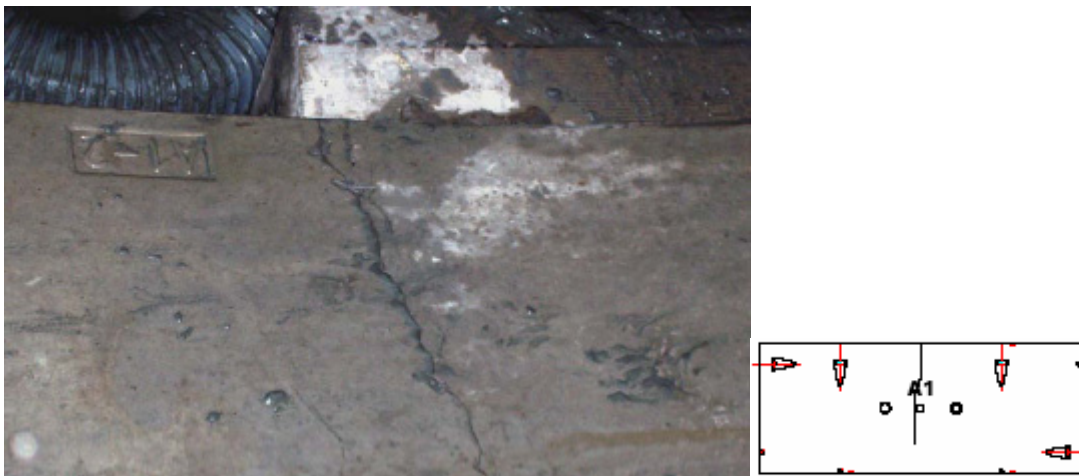


Figure 1-1: Spalling cracks between the loads, observed in the Barcelona line 9 metro tunnel



Figure 1-2: Spalling cracks observed in the Barcelona line 9 metro tunnel

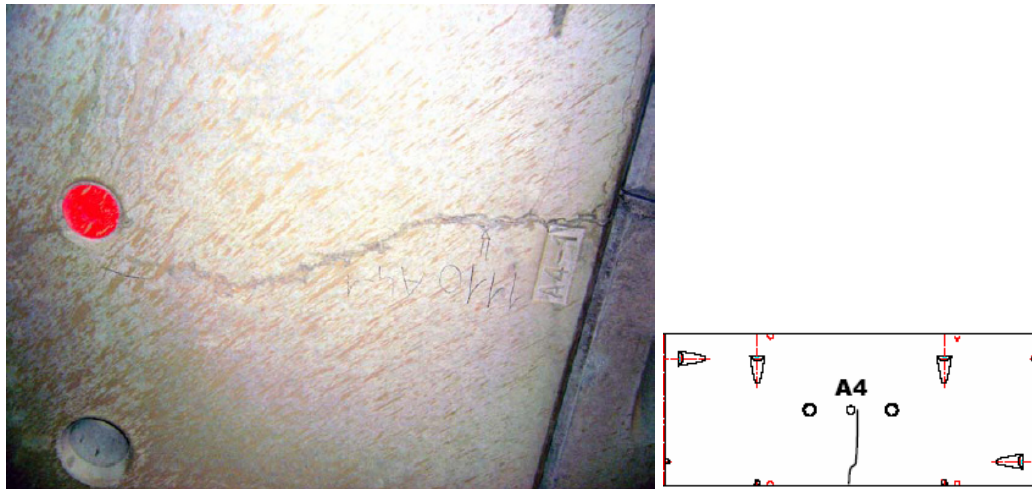


Figure 1-3: Spalling cracks observed in the Barcelona line 9 metro tunnel

The cause of the cracks is studied in several reports ([3], [5]). Usual causes are:

- Eccentricity of the thrust jack
- Inclination of the thrust jack
- A number of phenomena caused by the trumpet shape, the most important are:
 - Torsional deformation
 - A non-smooth support of the ring joint

It is desirable to mitigate or reduce these cracks as much as possible, because they cause a loose of quality and leakage and the repair costs are high. The cracks can be avoided by a change of the design of the tunnel. The forces must then be introduced into the tunnel lining in such a way that they do not cause peak stresses.

Another possibility is to change the material properties in order to reduce the cracks widths. Steel Fibre Reinforced Concrete (SFRC) has favourable solutions when it comes to cracking of concrete. The steel fibres add a post cracking stiffness to the concrete, which reduces crack widths and crack development in cracked zones of structures. The first aim of this thesis is to study the influence of steel fibres in the application in tunnel segments. The Barcelona line 9 metro tunnel is taken as example project to reach this goal.

The study of the influence of steel fibres in tunnel segments is done by Finite Element Method (FEM) simulations of a single tunnel segment with the FEM program DIANA. To study crack development, it is necessary to use a non-linear material model to describe the occurring cracks. When, as a test, the same simulation was done with two different FEM programs (ABAQUS and DIANA) with two generally accepted material models, the results were completely different. There are several non-linear material models, but it is not always easy to understand how they function and in which applications they can be used in the field of research on concrete structures. In order to make the non-linear simulations of the tunnel segment and concrete structures in general with a reliable model, the functioning, stability and user friendliness of the available DIANA models is studied, so this is the second aim of this thesis.

There are now two main questions to study in this thesis:

How do the available material models function and for which applications can they be used?

What is the influence of steel fibres on the crack development in steel fibre reinforced tunnel segments in the thrust jack phase?

This thesis starts with the description of the Barcelona line metro tunnel, the determination of the material properties of the concrete type which is used in the Barcelona line 9 tunnel and the definition of the model in Chapter 2, 3 and 4. After verification of the DIANA model with the previously used ABAQUS model in Chapter 5, the wish for more insight in modelling of SFRC in an FEM program arises.

To answer the first question, firstly the insight in the functioning of the models is increased by studying their background theory. This is done in Chapter 6. From the theoretical background is derived how they approach the real behaviour of concrete and in which field of application they can be used. Secondly, the material models are tested by simulating three experimental tests in Chapter 7: a four point bending test, which describes the uni-axial tensile behaviour, a splitting test with a line load, which describes a bi-axial stress state and a splitting test with a point load, which describes a tri-axial stress state. The studied models are the Total strain rotating crack, Total strain fixed crack and Drucker/Prager + multi directional fixed crack of DIANA and Concrete damaged plasticity of ABAQUS.

The study in these chapters results in a choice for a certain material model, which is used in the remaining part of the thesis. When the boundary conditions and the element choice of the model are defined in Chapter 8, there can be started with simulations of the thrust jack forces on a tunnel segment.

Boundary conditions which are representative for the Barcelona line 9 metro tunnel are simulated in Chapter 9. In this way, it can be checked if the above mentioned reasons for cracks do also cause cracks in this tunnel. In the subsequent chapters is searched for methods to avoid or reduce these cracks. In Chapter 10 the influence of the material type on the crack development is studied and the influence of the thrust jack configuration is studied in Chapter 11.

2 Barcelona line 9 metro tunnel

A new Metro line (Line 9) is currently being built in the Mediterranean city of Barcelona in Spain. The tunnel has a diameter of approximately 12 m and a length of 41.4 km. The tracks and platforms will be accommodated in a double deck configuration. The metro line has 43 stations and 15 interchanges. The line will be an important connection to the airport, the law district, the Barcelona fair and the high speed railway and for this reason traffic of 90 million trips per year is expected. The trace of the metro line is given in Figure 2-1.

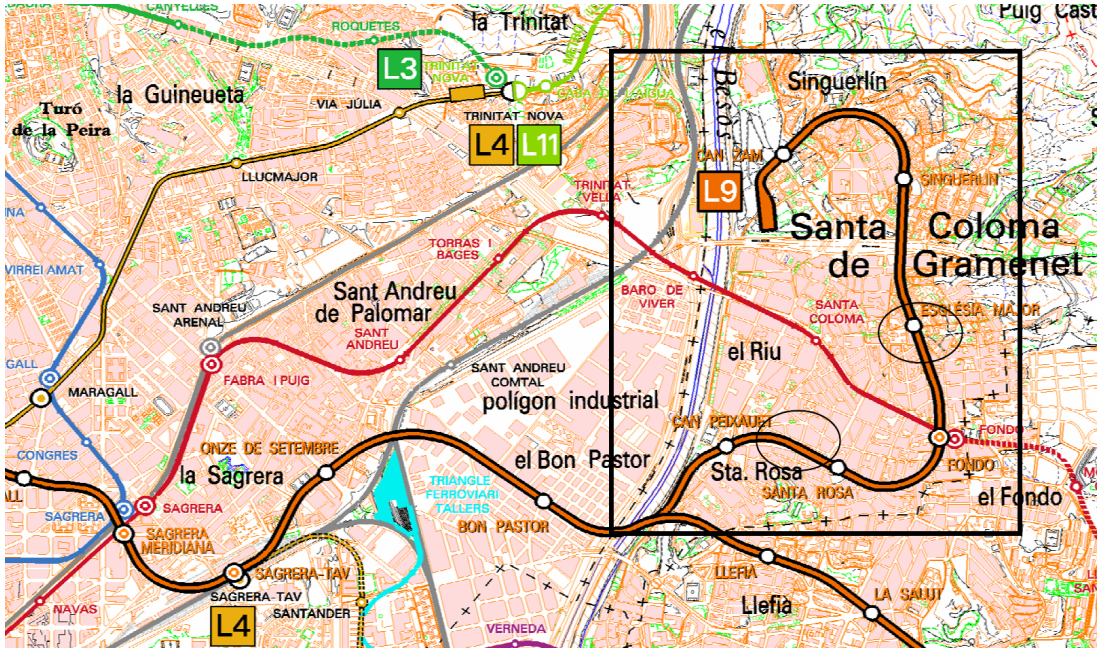


Figure 2-1: Trace of Barcelona metro line 9 (N. Della Valle, 2005)

The tunnel is being excavated, at a depth of 30 to 70 m below the surface, with an EPB-type (Earth Pressure Balanced) Tunnel Boring Machine (TBM). As the excavation progresses, a robot arm of the TBM places the prefabricated segments of the tunnel lining to complete it ring by ring. As the excavation progresses, the TBM applies a reaction force through 30 hydraulic jacks as the shield cuts into the rock and/or soil ahead of it. This reaction, which can reach values of up to 140 MN, acts on the lining last placed ring. In the service condition, the force exerted by each hydraulic jack is approximately 3 MN, which comes down to 12 mN per segment. The geometrical properties of the tunnel lining are given in Table 2-1.

Thickness	350 mm
Number of segments	7 + 1 key segment
External diameter	11.60 m
Internal diameter	10.90 m
Angle per segment	48°, key segment 24°
Medium ring depth	1.80 m

Table 2-1: Geometrical properties of the Barcelona line 9 tunnel lining

A cross section of the tunnel lining is given in Figure 2-2.

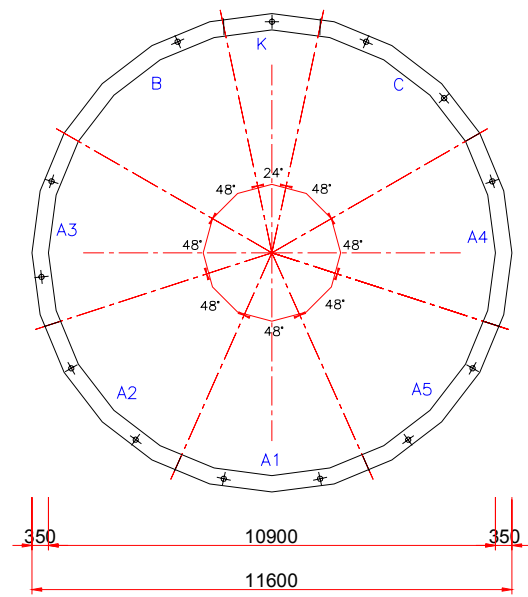


Figure 2-2: Cross section of the tunnel lining (Gettu, 2004)

3 Material properties

For Steel Fibre Reinforced Concrete (SFRC), the properties before cracking are similar to the properties of unreinforced concrete. The main reason for the addition of steel fibres is a tough post cracking behaviour, which is a favourable property of SFRC. To make use of this advantage in the design, it is necessary to determine the post cracking behaviour. Therefore, a four point bending test was carried out according to the Italian Standard UNI 11039. The four point bending test is described in Section 3.2. The remaining properties are taken from EuroCode 2 (EC2) [10], see Section 3.1.

All material properties which are used in this thesis are characteristic values. In this way, the real behaviour of the structure can be approximated as closely as possible. In practice, design values must be used to simulate the ULS.

3.1 Material properties according to EuroCode 2

3.1.1 Mix design

In practice, in the Barcelona line 9 metro tunnel, the segments are reinforced by conventional reinforcement and an addition of steel fibers, of which the contribution to the bearing capacity of the segment is not taken into account. A C50/60 concrete with 30 kg/m³ (0.38 weight-%) Wirand FF1 and 97 kg/m³ of conventional reinforcement have been used.

In this thesis the behaviour of a tunnel segment with only steel fibers is studied. An SFRC segment with a dosage of 45 kg/m³ (0.57 weight-%) Wirand FF1 hooked end steel fibres is modelled for the numerical simulation of the thrust jack action (Chapter 9). For simulation of the splitting test with line load, (Section 7.2) the same concrete mixture is used with 35 kg/m³ (0.45 weight-%) Wirand FF3 hooked end steel fibres. The composition of the concrete is given in Table 3-1, the grain size distribution of the aggregate is given in Table 3-2.

	Weight [kg]	Volume[dm ³]
Cement Portland 52.5 R	425.00	134.92
Water	142.00	142.00
Plasticizer	3.20	3.20
Aggregate	1885	699.88
Air assumed		20.00
Water/cement ratio	0.33	1.05

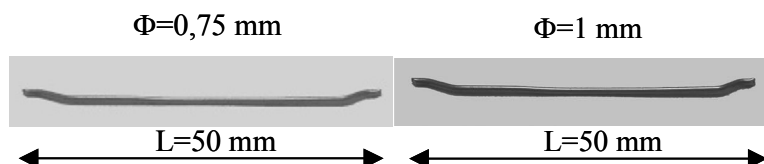
Table 3-1: Composition of the C50/60 mixture

Grain classes [mm]	Nominal diameter [mm]	p [%]	Weight (referring 1m ³) [kg]
0 – 0.35	0.35	8.42	163.00
0.35-0.45	0.45	10.63	42.00
0.40-0.6	0.60	13.53	54.00
0.6-1.5	1.50	26.09	236.00
1.5-2.5	2.50	36.04	187.00
2.5-3.5	0.35	8.42	163.00
4.0-6.0	6.00	60.27	236.00
7.0-12.0	10.00	80.17	374.00
10.0-15.0	15.00	100.00	373.00

Table 3-2: Grain classes of the C50/60 mixture

The data concerning the steel fibres is summarised in Table 3-3 and the geometry of the steel fibres is given in Figure 3-1.

	Wirand FF3	Wirand FF1
Type of steel	Carbon	Carbon
Shape	Hooked	Hooked
Cross Section	Circular	Circular
Ultimate Tensile Strength [MPa]	≥ 1100	≥ 1100
Modulus of Elasticity [MPa]	210000	210000
Length [mm]	50	50
Diameter [mm]	0.75	1
Aspect Ratio [l/d]	≥67	50

Table 3-3: Data steel fibres

Figure 3-1: Geometry of the Wirand FF3 (Left) and the Wirand FF1 steel fibre

3.1.2 Material properties

The material properties of the C50/60 concrete are mainly derived from EC2. The values of importance for this report taken from EC2 are given in Table 3-4. The post cracking behaviour is not defined in EC2 and is therefore determined by experimental tests. This is described in Section 3.2.

Material property	Symbol	Value [MPa]
Medium cubic compressive strength	$f_{cm,cube}$	69.6
Medium cylindrical compressive strength	$f_{cm,cylinder}$	58.0
Medium tensile strength	f_{ctm}	4.10
Modulus of Elasticity	E_{cm}	37000

Table 3-4: Material properties by EuroCode 2

3.1.3 Compressive behaviour

Even though the compressive stress-strain responses of aggregate and cement paste are linear, the compressive stress-strain response of concrete is nonlinear. This is caused by interaction between the cement paste and the aggregate. Micro cracks occur at the aggregate-paste interfaces at relatively low stress levels. The development and propagation of these cracks soften the concrete, resulting in a "rounded" stress-strain curve. Prior to failure, significant longitudinal cracking develops and considerable lateral expansion occurs.

There are several ways to express the uni-axial compressive stress-strain response of concrete. For relatively low concrete compressive strengths (<40 MPa) a parabola is a suitable method to describe the compressive stress-strain function. The expression of the parabola is:

$$f_c = f'_c \left(2 \frac{\varepsilon_{cf}}{\varepsilon'_{c'}} - \left(\frac{\varepsilon_{cf}}{\varepsilon'_{c'}} \right)^2 \right)$$

The curve of the parabola for C50/60 concrete is given in Figure 3-2. A more suitable curve for the 50/60 concrete is the Thorenfeldt curve. This curve is described by the formula:

$$f = -f_p \frac{\alpha}{\alpha_p} \left(\frac{n}{n-1 + \left(\frac{\alpha}{\alpha_p} \right)^{nk}} \right) \text{ in which}$$

$$n = 0.80 + \frac{f_c}{17} \text{ and}$$

$$k = \begin{cases} 1 & \text{if } \alpha \leq \alpha_p \\ 0.67 + \frac{f_c}{62} & \text{if } \alpha_p < \alpha < 0 \end{cases}$$

In EC2 a stress-strain relation for non-linear structural analysis is given:

$$\frac{\sigma_c}{f_{cm}} = \frac{k\eta - \eta^2}{1 + (k-2)\eta}$$

Where:

$$\eta = \varepsilon_c / \varepsilon_{c1}, \quad \varepsilon_{c1} \text{ is the strain at peak stress (} = 2.45\text{‰ for C50/60).}$$

$$k = 1.05 E_{cm} * |\varepsilon_{c1}| / f_{cm} \quad (f_{cm} = 58 \text{ MPa for C50/60}).$$

This expression is valid for $0 < |\varepsilon_c| < |\varepsilon_{cu1}|$ where ε_{cu1} is the nominal ultimate strain (= 3.50‰ for C50/60).

The aforementioned curves are presented in Figure 3-2.

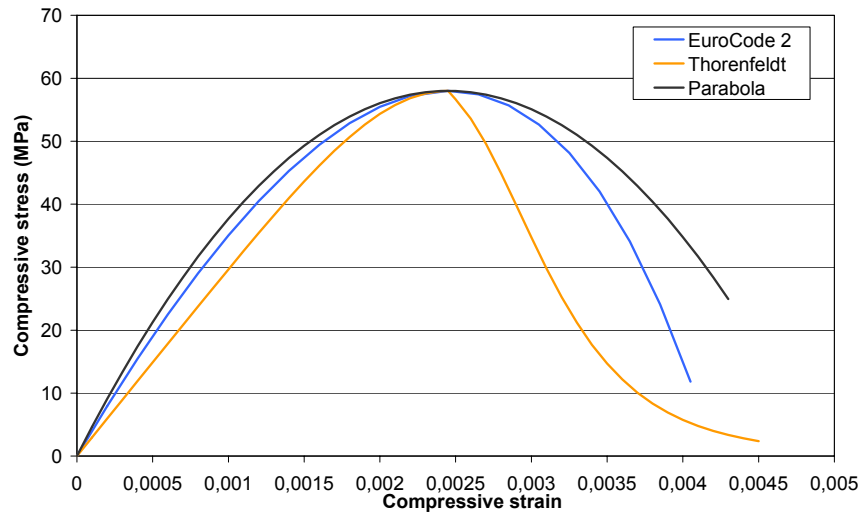


Figure 3-2: Compressive stress-strain curves for C50/60 concrete

Using DIANA, as described in the literature survey, it is possible to apply the parabola or Thorenfeldt curve in the total strain models. The curve by EC2 can be approximated by a multi-linear stress-strain function. In the Drucker/Prager + smeared cracking model, the compression function is given by a yield function, see Literature Survey. A uni-axial compression function like given above is not used in this case.

3.2 Post cracking behaviour

To determine the uni-axial constitutive relations after cracking, experimental tests have been carried out by Tiberti [20]. The tests have been done according to the Italian standard for fibre reinforced concrete (UNI 11039). The test specimen is a notched beam on two supports, subjected to two concentrated loads, as showed in Figure 3-3.

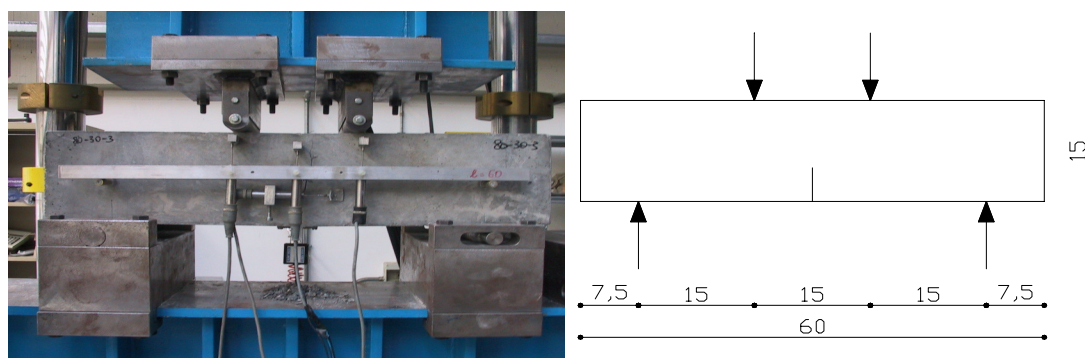


Figure 3-3: Experimental test; Test arrangement (left) and dimensions (right)

As displayed in Figure 3-4, in-between the loads no shear force and a constant bending moment occurs.

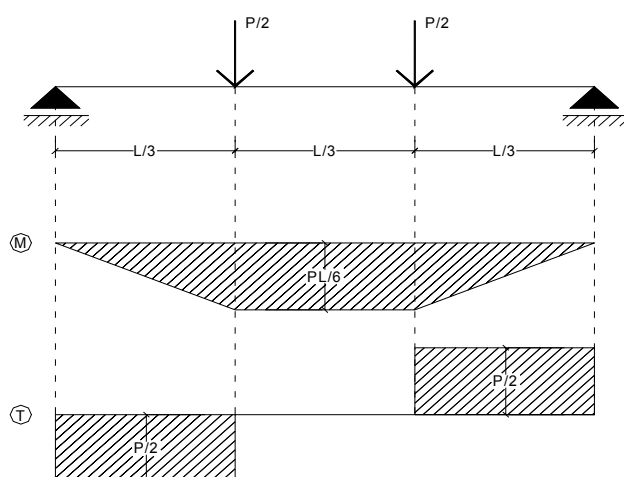


Figure 3-4: Distribution of bending moments and shear forces in the notched beam

According to the test arrangement and the distribution of forces in the notched beam, the main crack is expected above the notch (Figure 3-5). Therefore, the measurements during the test are focused on the region around the notch.

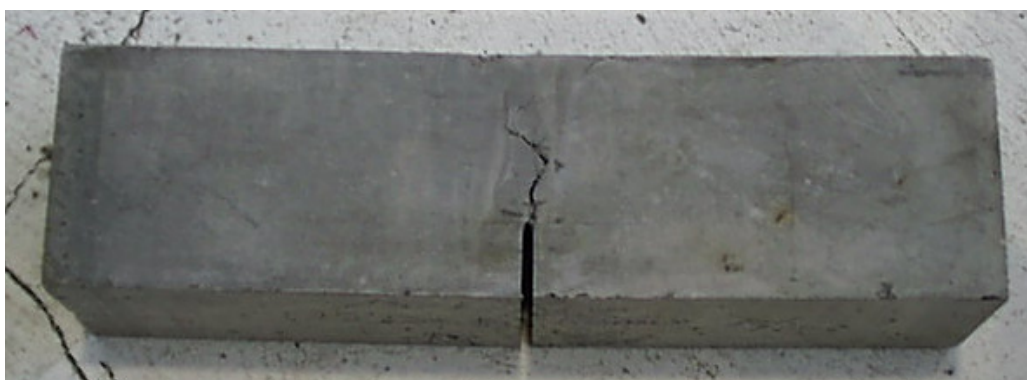


Figure 3-5: Crack above the notch after testing

From the measurements a graph is derived in which the CTOD (Crack Tip Opening Displacement) is plotted against the applied load (Figure 3-7). To find the constitutive relations, an inverse analysis is performed. DIANA is used to approximate the experimental results. The compressive strength, the tensile strength and the modulus of elasticity are taken from EC2, so the constitutive relation after cracking remains as the variable parameter. There are different types of tension post-cracking laws: parabolic and Hordijk are examples. There has been chosen for a bi-linear tension softening diagram to describe the post cracking behaviour. This is displayed in Figure 3-6.

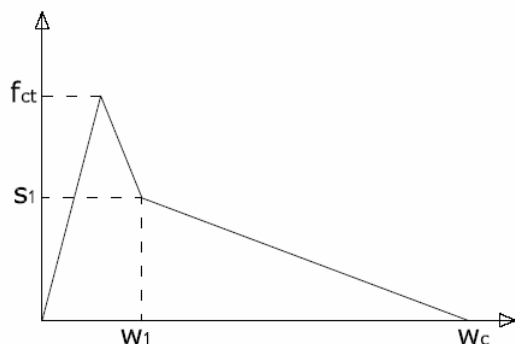


Figure 3-6: Bi-linear tension softening function

Fracture of plain concrete or concrete reinforced with a single type of fibre is approximated by a bi-linear law. The first branch is steeper and simulates the bridging of the early micro-cracks. The second branch simulates the aggregate interlocking in plain concrete or the fibre links in fibre reinforced concrete. When more than one type of fibre is adopted, it may be necessary to use a polylinear law with more branches since different fibres activate at different cracks. In this thesis one type of fibre is applied, so a bi-linear law is sufficient.

The variable parameters are w_1, s_1 and w_c , see Figure 3-6. w_1 and w_c are the crack widths and s_1 is the stress corresponding to w_1 . A discrete crack model with a predefined crack above the notch is used to determine these parameters. This is done by trial and error. The discrete crack model is used for this iterative method, because it is fast. Reasonable values are found when the CTOD curve of the discrete crack model is approximately at the middle of the scatter of the experimental results. The highest and the lowest experimental curves are considered as unimportant, because they might be exceptions of the normal scatter. Figure 3-7 shows the comparison between the numerical and the experimental curves, obtained from a SFRC with 45 kg/m^3 Wirand FF1 steel fibres.

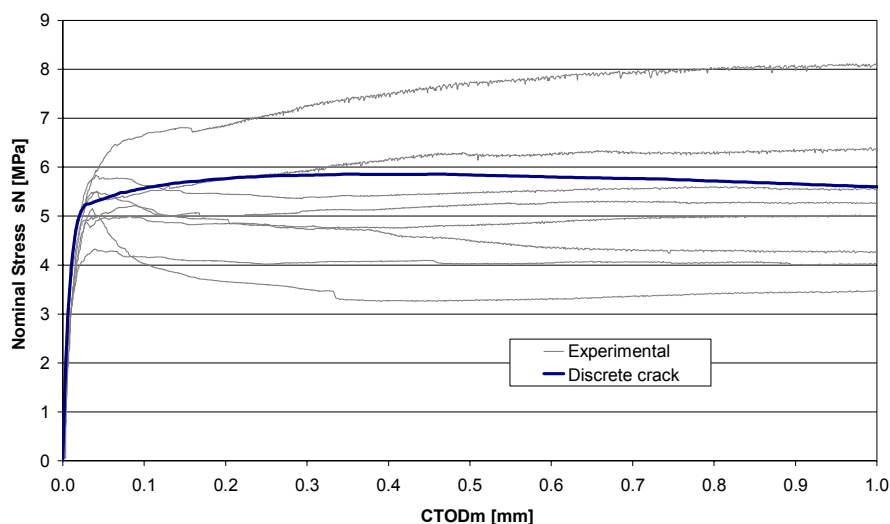


Figure 3-7: Approximation of the experimental results by a discrete crack model

The values of the parameters which fit for the post cracking behaviour are given in Table 3-5.

Fiber type	Volume fibers [%]	E [MPa]	f_{ct} [MPa]	s_1 [MPa]	w_1 [mm]	w_c [mm]	G_f [N/m]
Wirand FF1	0,57	37000	4,10	2,134	0,023	5,35	5,755
Wirand FF3	0,45	37000	4,10	1,505	0,028	3,90	2,992

Table 3-5: Parameters of the bi-linear tension softening diagram

The use of the discrete crack model is limited by models in which the locations of the cracks are known on forehand. In the model of a tunnel segment this is not the case, so this model is not suitable. To create the possibility of having cracks on an arbitrary location, a smeared crack model or a plasticity model must be used. In these cases the post cracking behaviour is described in the elements. When the tension strength of the concrete in a certain element is reached, its σ - ε law changes. When a smeared crack or plasticity model is used, it is necessary to transform the σ - w relation of the discrete crack model into a σ - ε relation. By doing this it is assumed that an element can have one crack, which is described by ε_{cr} . The crack with a width w is smeared over the element, so:

$$\varepsilon_{cr} = \frac{w}{l}$$

in which l is the length of the element perpendicular to the crack.

Because the shapes of the elements are in general not regular and equal l is approximated by a characteristic length l_c . In a two dimensional model:

$$l_c = \sqrt{A},$$

with A the average area of an element.

In a three dimensional model:

$$l_c = \sqrt[3]{V},$$

with V the average volume of an element.

In order to have a good approximation of the post cracking behaviour, the elements should have dimensions as equal as possible.

This method is used to determine the post cracking relation for different material models in the later chapters.

[20], [9], [8], [7], [10]

4 Models of the tunnel segment

DIANA is used to analyse the stress distribution in the segment due to the thrust jack forces. The first step is to validate the model. To do this, a comparison is made with the FEM program ABAQUS [20]. The input file of the ABAQUS model is modified and implemented in DIANA.

In 2004 Tiberti [20] assumed a Japanese thrust jack configuration. Therefore the ABAQUS analyses were made with a model with four separate thrust jacks. To compare DIANA with Tiberti's ABAQUS analyses, it is necessary to make exactly the same model and loading situation. Therefore firstly a model with four separate thrust jacks is made.

In practice, two pairs of thrust jacks are used. During the process of this thesis, a part of the tunnel was finished and several cracks were reported. One of the goals of this thesis is to show in which situation these cracks occur. Therefore it is necessary to use a model which is close to practice, so a model with two pairs of thrust jacks was made.

In the first section the models which are used for the comparison between DIANA and ABAQUS are described and in the second section the DIANA model for analyses of thrust jack loading situation is described.

4.1 Models based on four separate thrust jacks

4.1.1 *Imported ABAQUS model*

For the Barcelona line 9 metro tunnel, a calculation has been made to determine the behaviour of a SFRC segment loaded by thrust jack forces by Tiberti [20]. For this calculation the FEM program ABAQUS has been used. The input file of the ABAQUS model is modified and implemented in DIANA in order to have the same mesh for a comparison. The ABAQUS-model consists of 4032 8-node brick elements and the material is modelled by the Concrete Damaged Plasticity model which consists of the combination of a yield model with a nonassociated flow potential (Drucker/Prager).

The Japanese thrust jack configuration is considered in the ABAQUS simulations. Each of the four thrust jacks works on a single steel plate with the same dimensions as the bearing pads (Figure 4-2). These pads are positioned in the rear face of the tunnel segment in order to realise the contact surface between two tunnel rings.

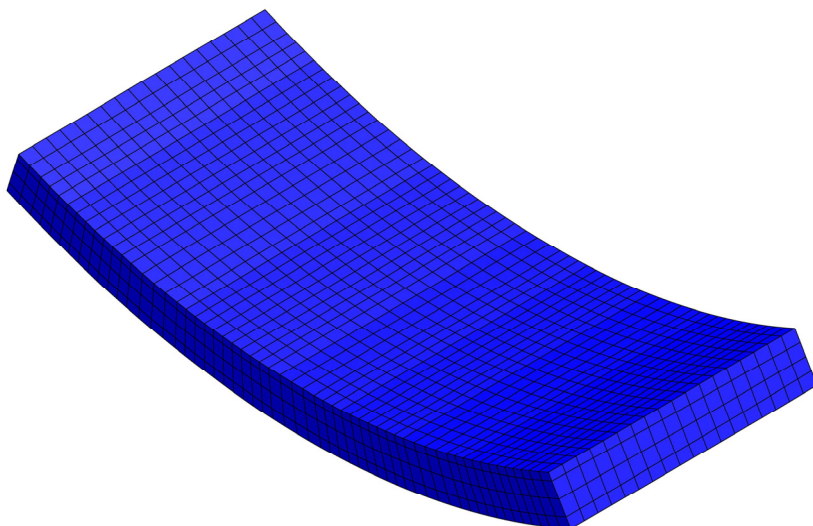


Figure 4-1: ABAQUS model imported in DIANA

The thrust jacks are modelled as four equally distributed forces on the defined surfaces. The segment is supported by the segments of the previously assembled ring. The bearing pads are just two mm thick and are made of PEBD, which is an easy compressible material. Therefore a uniform support over the ring joint, which is visualised by the orange springs in Figure 4-2, is assumed. The bearing pads are not taken into account. This support is modelled by discrete no-tension springs in z-direction on the nodes of the elements.

In this thesis, because of the presence of the four bearing pads and the difficulties in placing process, this boundary condition is investigated (Section 8.2).

In a discontinue boring process the thrust jack forces are significantly higher during the boring process. In this situation the total ring has been assembled. Therefore the ring is assumed to be completely assembled in the ABAQUS simulations. The adjacent segments give a support in tangential direction in the lateral joints. This support is modelled by no-tension springs too. These springs are placed on the element nodes of the surface of the lateral joints. They act in the direction normal to the plane of the lateral joints.

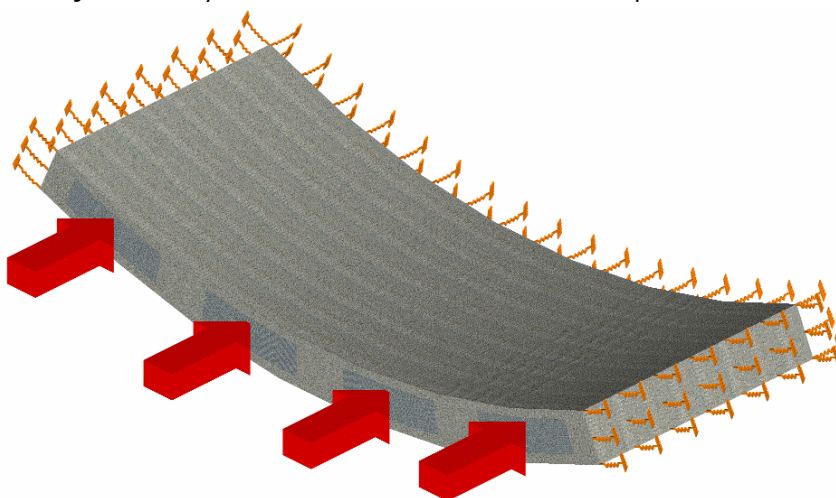


Figure 4-2: Schematization of the load and the boundary conditions in the ABAQUS simulations

To approximate the stiffness of these springs, a linear displacement imposed analysis, as shown in Figure 4-3, has been done.

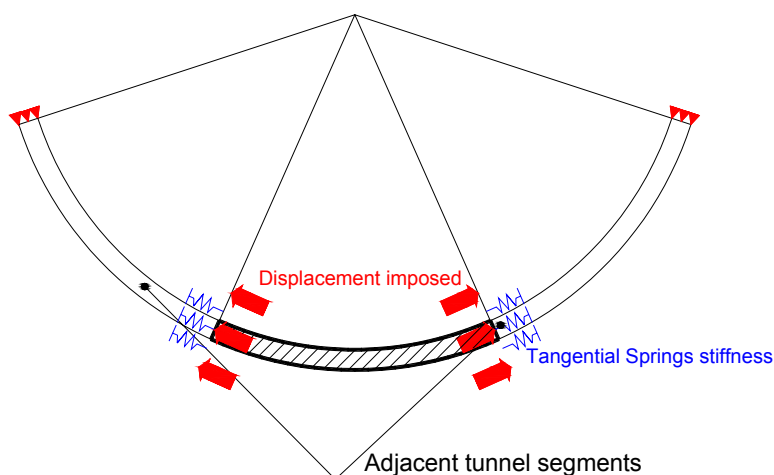


Figure 4-3: Schematization of the boundary conditions to determine the tangential spring stiffness

The stiffness of the springs acting on the rear face of tunnel segment has been determined according to the scheme which is shown in Figure 4-4.

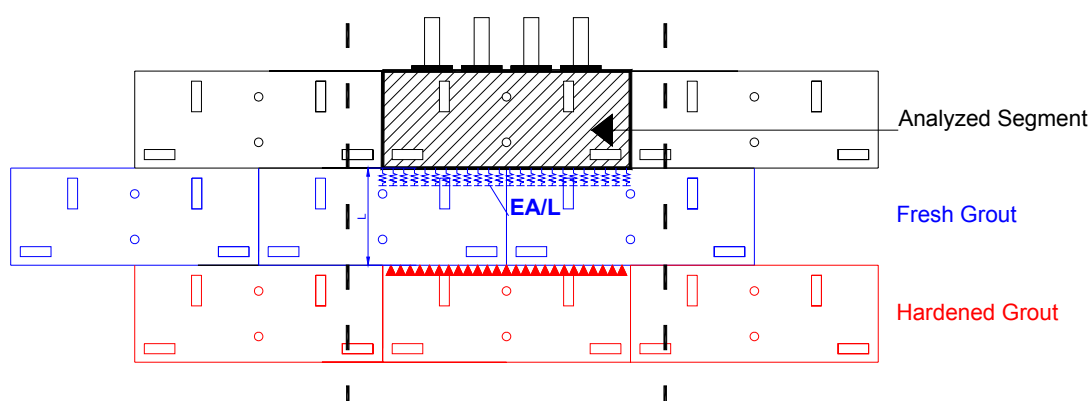


Figure 4-4: Schematization of the boundary conditions to determine the longitudinal spring stiffness

The completed part of the tunnel is subjected by ground and grout loading. On the last placed rings the grout layer is not completely hardened. Going from the TBM in the direction of the earlier placed rings, the stiffness of the grout layer increases. Therefore, the friction between the grout layer and the tunnel lining increases in this direction. A simplification has been made to determine the stiffness of the springs in longitudinal direction. The second ring (the last but one placed ring) is assumed to be in completely liquid grout, so there is no friction. The other rings are assumed to be in completely hardened grout and are therefore infinitely stiff. In the scheme in Figure 5-1, this means that the red ring is a rigid support and the blue ring is completely elastic. By using this simplification, the stiffness of the blue ring is determined by EA/L , where E is the modulus of elasticity of the concrete, A is the area of the surface of the ring joint and L is the depth of the ring.

4.1.2 DIANA model

The results of the comparison between the ABAQUS simulation and the DIANA simulation of the imported ABAQUS model are presented in Chapter 5. Because the analyses show completely different results, the same model is made in the DIANA pre-processor. This is done in order to investigate whether the imported model is correct. The DIANA model

consists of 5184 8-node brick elements and has the same dimensions and boundary conditions as the model which is imported from ABAQUS. The model with its mesh is presented in Figure 4-5.

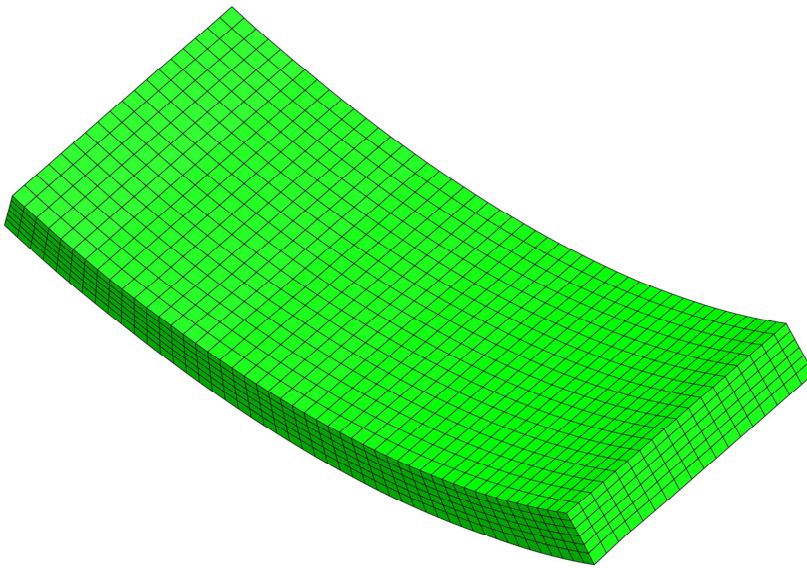


Figure 4-5: DIANA model based on four separate thrust jacks

4.2 Model based on two pairs of thrust jacks

In order to simulate the practice as well as possible, the analyses in this thesis are done with a DIANA model which is based on two pairs of thrust jacks. The mesh of this model is presented in Figure 4-6 and the element type and the boundary conditions are determined in Chapter 8. The difference with the previously presented model is that extra surfaces are defined on the ring joint. These surfaces have the dimensions of the thrust jack plates. In this way, the mesh generator creates element borders on the edge of the surfaces, which makes it possible to define the load exactly on the load surfaces.

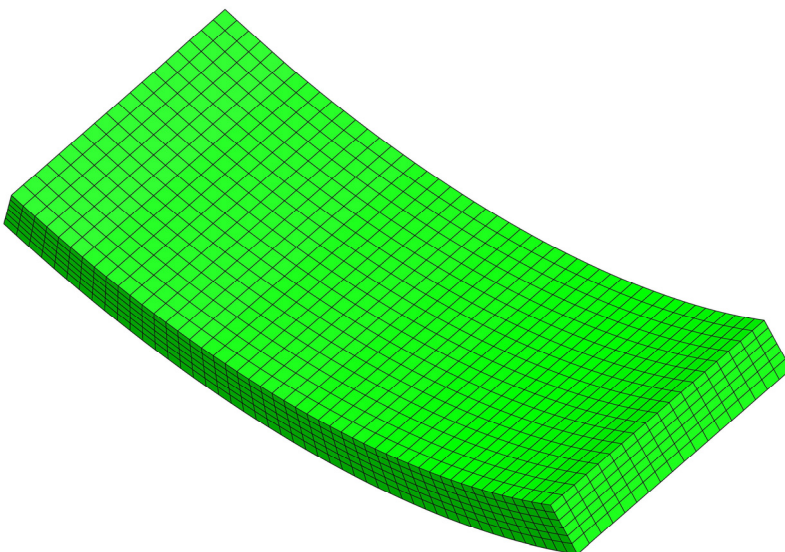


Figure 4-6: DIANA model based on two pairs of thrust jacks

[20]

5 Validation of the models

Previously, non-linear FEM simulations of the Barcelona line 9 metro tunnel have been done by Tiberti [20] at the Brescia University. For these calculations the FEM program ABAQUS was used. To validate the models, the simulation of the tunnel segment model subjected to the load of the thrust jacks is done with DIANA (total strain rotating crack) and ABAQUS (Concrete Damaged Plasticity).

This comparison is based on the meshes which are defined in Section 4.1 and the boundary conditions and hypotheses as described in Paragraph 4.1.1.

The total strain rotating crack model is recommended by experienced DIANA users, so this is used in the DIANA analysis. The concrete compression behaviour is modelled without considering confinement. The material is the earlier mentioned C50/60 concrete with 45 kg/m³ of Wirand FF1 steel fibres.

In Figure 5-1, numerical results are presented in terms of the total load applied by thrust jacks and the average displacement in longitudinal direction on the loading areas. This diagram is used to describe the global behaviour of the tunnel segment in the numerical simulations in the rest of this thesis.

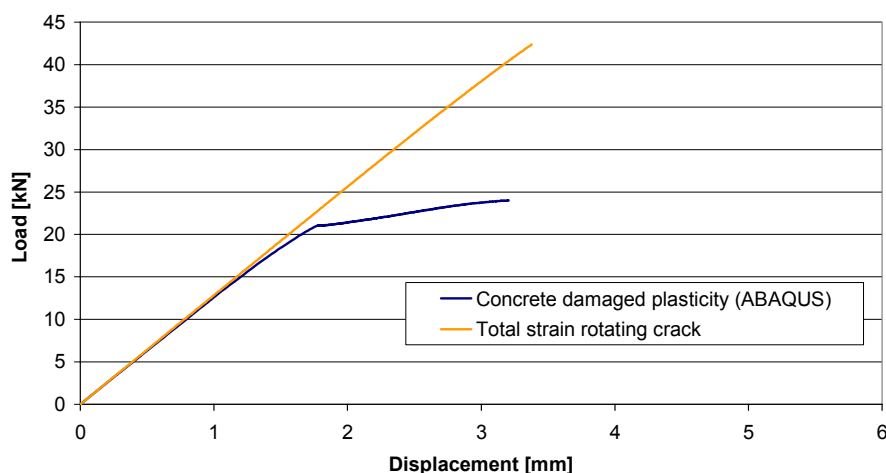


Figure 5-1: Load displacement curves of the model for comparison, Total Strain rotating crack (DIANA) and Concrete damaged plasticity (ABAQUS)

The DIANA analysis reaches an ultimate load of 42 mN, whereas the ABAQUS analysis reaches only 24 mN. The DIANA analysis stops because the compressive strength is reached (58 MPa). In the ABAQUS analysis the collapse mechanism is governed by cracks by tensile bursting stresses under the thrust jack plates (for explanation concerning cracks by bursting stresses, see Section 9.2).

Because of the large difference in this comparison, it is desirable to investigate its reason. Firstly, the numerical model (mesh and boundary conditions) is checked. Therefore the same simulation with a new mesh, which is made in the DIANA graphical user interface, is done. This mesh gives exactly the same results as the imported ABAQUS-mesh, so it is assumed that the mesh and boundary conditions are the same in both FEM programs.

The next check is to investigate if different material models lead to different results by checking the different available material models of DIANA on the segment model. The following material models are tested:

- Total strain rotating crack
- Total strain fixed crack
- Drucker/Prager + multi directional fixed crack

The curve of the analysis with the Total strain rotating crack model is used as a reference curve.

In the Total strain fixed crack model and the Drucker/Prager + smeared crack model, a shear retention factor β is present. This factor represents the shear stiffness along the crack. A detailed description of this factor is given in the 6.3.2. For both material models, a simulation is made with two values of β ($\beta=0$ and $\beta=0.2$), in order to see if it has influence on the ultimate load.

In the Drucker/Prager + smeared cracking model it is possible to choose between constant- and linear tension cut off. The tension cut off describes the strength of the material in stress situations with tension and compression in different principle directions in the same element. A detailed description is given in the 6.3.3. For the Drucker/Prager + smeared cracking model a simulation with constant- and linear tension cut off is done, in order to see the difference. Like in the Total strain fixed crack model, the shear retention factor is present in this material model. Also here a variation of β is made by making every analysis with $\beta=0$ and $\beta=0.2$.

The graphs of the above described analyses are given below.

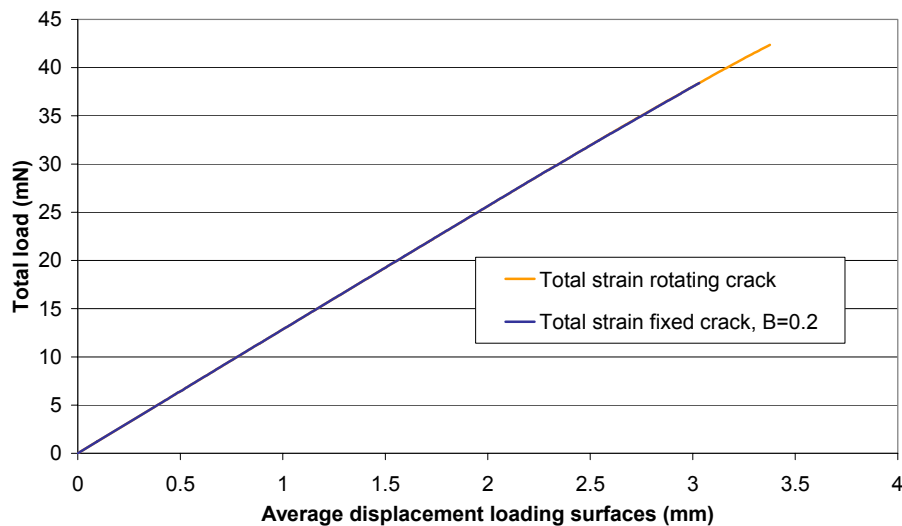


Figure 5-2: Total load- average displacement on loading areas, DIANA total strain rotating crack vs. DIANA total strain fixed crack, $\beta = 0.2$

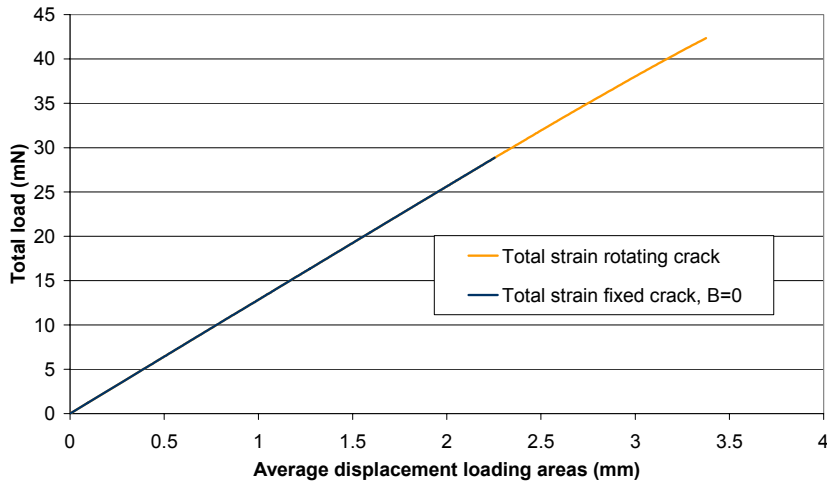


Figure 5-3 Total load- average displacement on loading areas, DIANA total strain rotating crack vs. DIANA total strain fixed crack, $\beta = 0$

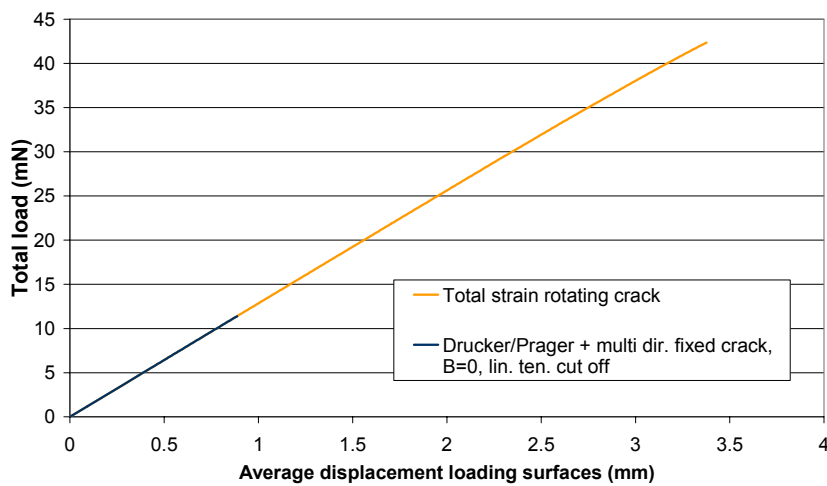


Figure 5-4: Total load- average displacement on loading areas, DIANA total strain rotating crack vs. DIANA Drucker/Prager + multi directional fixed crack, linear tension cut off, $\beta = 0$

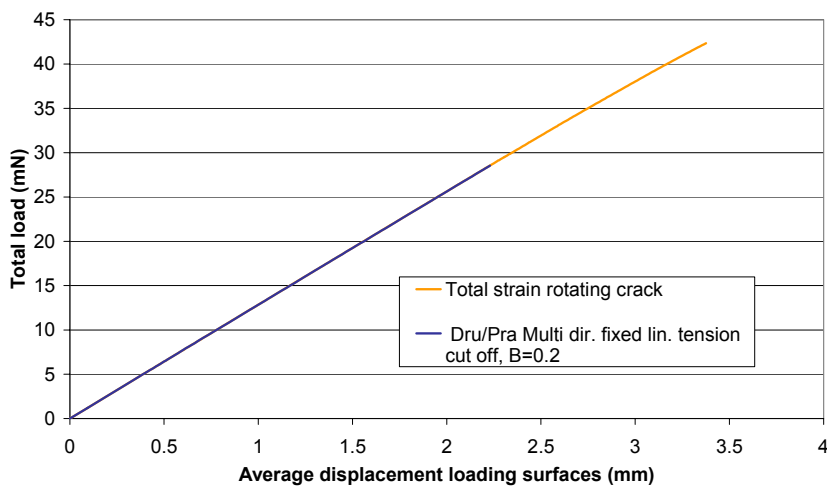


Figure 5-5: Total load- average displacement on loading areas, DIANA total strain rotating crack vs. DIANA Drucker/Prager + multi directional fixed crack, linear tension cut off, $\beta = 0.2$

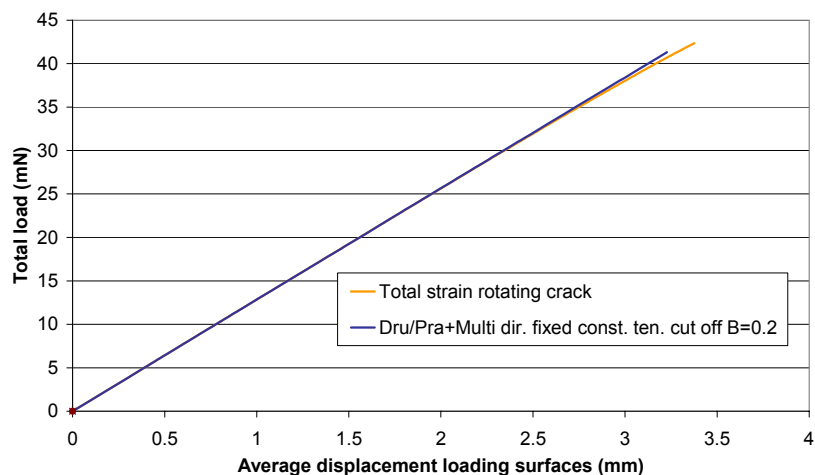


Figure 5-6: Total load- average displacement on loading areas, DIANA total strain rotating crack vs. DIANA Drucker/Prager + multi directional fixed crack, constant tension cut off, $\beta = 0.2$

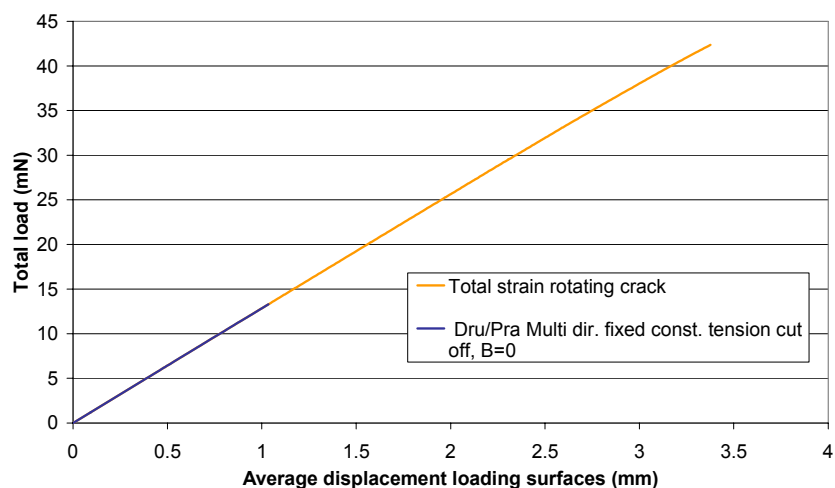


Figure 5-7: Total load- average displacement on loading areas, DIANA total strain rotating crack vs. DIANA Drucker/Prager + multi directional fixed crack, constant tension cut off, $\beta = 0$

From the above figures it becomes clear that, even though the global stiffness is the same for all the tested models, the ultimate load varies significantly. As there are no experimental data of this simulation, it is impossible to determine which model approaches the reality the best.

In order to gain insight in the working of material models which describe concrete cracking, the background of these models is studied in Chapter 6.

To be able to continue analysing the tunnel segment, it is desirable to know which material model is the most suitable one. Therefore, three experimental tests are simulated with the material models of ABAQUS and DIANA in Chapter 10.

6 Modelling of SFRC in a FEM program

The main cause for nonlinearity of concrete is cracking, due to the limited capacity of sustaining tensile stresses and strains. The behaviour of SFRC is comparable to plain concrete, with a stiffer post cracking behaviour as the main difference. Numerical modelling of concrete and SFRC can be done in several ways. Discrete cracking, smeared cracking and a damaged plasticity model are used in this thesis. Therefore these models are described in this chapter.

6.1 Discrete crack models

A discrete crack model consists of linear elastic elements and predefined cracks modelled by interface elements. Even though this is a fully nonlinear approach, the procedure consists of a series of linear calculations. The locations of the interface elements are chosen either on a basis of a smeared crack approach or by assessment of experimental data. The interface elements have dual nodes, which have the same coordinates. When the normal stress in an integration remains below the tensile strength the stress-strain relation in the interface is taken linear elastic, with a high dummy stiffness in order to practically suppress deformations in the interface. When the tensile strength is exceeded in an integration point, the unbalanced force thus generated may cause displacements between the two nodes of the node-sets of the interface. We obtain opening (mode-I behaviour) as well as sliding (mode-II behaviour) along the interface element. Of course, the success of this approach crucially depends on a correct estimation of the crack propagation path. Furthermore, the approach is primarily applicable to localized failure where we indeed have one dominant crack that leads to failure. If these conditions are not fulfilled, or the locations of the cracks are not known on forehand, a discrete-crack analysis along these lines may be less successful. A smeared-crack model or a damaged plasticity model is then a good alternative.

6.2 Implementation of the material behaviour

The use of the discrete crack model is limited by models in which the locations of the cracks are known on forehand. In the model of a tunnel segment this is not the case, so the discrete crack model is not suitable. To create the possibility of having cracks on an arbitrary location, a smeared crack model or a damaged plasticity model can be used.

In these cases the post cracking behaviour is described in the elements. When the tensile strength of the concrete in a certain element is reached, its σ - ε law changes. When a smeared crack or plasticity model is used, it is necessary to transform the σ - w relation of the discrete crack model into a σ - ε relation. By doing this it is assumed that an element can have one crack, which is described by ε_{cr} . The crack with a width w is smeared over the element, so:

$$\varepsilon_{cr} = \frac{w}{l}$$

in which l is the length of the element perpendicular to the crack, also called the crack bandwidth.

Because the shapes of the elements are in general not regular and equal l is approximated by a characteristic length l_c . In a two dimensional model:

$$l_c = \sqrt{A},$$

with A the average area of an element. In theory, an element with quadratic shape functions can have a crack in half the element, so the characteristic length is:

$$l_c = \frac{1}{2}\sqrt{A}$$

In a three dimensional model:

$$l_c = \sqrt[3]{V},$$

with V the average volume of an element. When higher order elements are used, the element cracks partly. So also here multiplication factor smaller than one can be implemented.

In practice, the crack bandwidth varies from the theoretical value. In DIANA the default values of the crack bandwidth are therefore higher than the theoretical ones. DIANA suggests $l_c = \sqrt{A}$ for higher order plain stress elements, $l_c = \sqrt{2A}$ for linear plain stress elements and $l_c = \sqrt[3]{V}$ for solid elements.

The crack bandwidths in this thesis are calculated by $l_c = \sqrt{A}$ for all plain stress elements and $l_c = \sqrt[3]{V}$ for all solid elements.

In order to have a good approximation of the post cracking behaviour, the elements should have as much as possible equal dimensions.

In the post-processor of the FEM programs it is possible to present the crack strains. With these crack-strains it is possible to calculate the crack widths by making the inverse operation, namely multiplying them by l_c . This feature will be used in the later chapters when simulations of the tunnel segment are analysed.

The limitation of this feature is the earlier made assumption that each element can have one crack. The consequence of this assumption is that a mesh must have at least as much elements in a certain region as there are cracks in reality.

Compared to tough materials, in brittle materials, few wide cracks occur. This means that tough materials need a finer meshes than brittle materials.

A too coarse mesh can have the following two consequences:

- The response is stiffer than in reality, because within the element length there is only one crack modelled, while there are two cracks in reality. If the stress remains the same, the deformations increase when there are more than one cracks instead of one.
- The response softer than in reality, because all deformation is concentrated in one crack. If the deformation remains the same, the deformation per crack reduces, so the stress in a crack is higher.

The approach which is used in this section is used in the smeared crack and damaged plasticity models, which are described in the following sections.

6.3 Smeared crack models

This section describes smeared crack models. The principle of smeared cracking is described in Paragraph 6.3.1 and the available crack models of DIANA are described in the subsequent paragraphs.

6.3.1 Principle of smeared cracking

Prior to cracking, concrete is modelled by crack models as an isotropic, linear-elastic material. In a two-dimensional state in the global axis-system this means:

$$\begin{bmatrix} \sigma_{xx} \\ \sigma_{yy} \\ \sigma_{xy} \end{bmatrix} = \frac{E}{1-\nu^2} \begin{bmatrix} 1 & \nu & 0 \\ \nu & 1 & 0 \\ 0 & 0 & 1/2(1-\nu) \end{bmatrix} \begin{bmatrix} \varepsilon_{xx} \\ \varepsilon_{yy} \\ \gamma_{xy} \end{bmatrix}$$

When the mayor principal tensile stress exceeds the tensile strength or, when for example linear tension-cut-off is applied in the Drucker/Prager + smeared cracking, the tension-cut-off criterion is violated by a combination of principal stresses, the isotropic constitutive law is replaced by an orthotropic stress-strain law. The local axis-system is transformed orthogonal to the principal stresses, with s the axis tangential to the crack and n the axis orthogonal to the crack.

Firstly the general constitutive law is transformed to the constitutive law in the directions of the principle stresses and both the normal stiffness and the shear stiffness across the crack are set equal to zero:

$$\begin{bmatrix} \sigma_{nn} \\ \sigma_{ss} \\ \sigma_{ns} \end{bmatrix} = \begin{bmatrix} 0 & 0 & 0 \\ 0 & E & 0 \\ 0 & 0 & 0 \end{bmatrix} \begin{bmatrix} \varepsilon_{nn} \\ \varepsilon_{ss} \\ \gamma_{ns} \end{bmatrix}$$

To make the crack model more similar to the reality, softening is applied in the n -direction. This means that the stiffness normal to the crack is not zero, but decreases after cracking. This is realised by implementing a μE in the matrix:

$$\begin{bmatrix} \sigma_{nn} \\ \sigma_{ss} \\ \sigma_{ns} \end{bmatrix} = \begin{bmatrix} \mu E & 0 & 0 \\ 0 & E & 0 \\ 0 & 0 & 0 \end{bmatrix} \begin{bmatrix} \varepsilon_{nn} \\ \varepsilon_{ss} \\ \gamma_{ns} \end{bmatrix}$$

Where $\mu = \mu(\varepsilon_{nn})$, so the stiffness of the material normal to the crack depends on the crack strain. Furthermore, a reduced shear stiffness and Poisson coupling can be reimplemented:

$$\begin{bmatrix} \sigma_{nn} \\ \sigma_{ss} \\ \sigma_{ns} \end{bmatrix} = \begin{bmatrix} \frac{\mu E}{1-\nu^2} & \frac{\nu\mu E}{1-\nu^2} & 0 \\ \frac{\nu\mu E}{1-\nu^2} & \frac{E}{1-\nu^2} & 0 \\ 0 & 0 & \beta G \end{bmatrix} \begin{bmatrix} \varepsilon_{nn} \\ \varepsilon_{ss} \\ \gamma_{ns} \end{bmatrix}$$

The main property of crack models is that they are orthogonal. In the different directions of the principal stresses can occur different stiffnesses. This can easily be seen by the fact that μ is applied to certain terms of the matrix, not to all terms of the matrix.

In analyses of concrete cracking, often cracks appear and close in a later stadium. They even might reopen in later load steps. Therefore, it is important to carefully handle the closing and reopening of cracks. This is done by a secant modulus in the DIANA models. This means that the stress-strain relation goes linearly back to zero in an unloading situation (Figure 6-1).

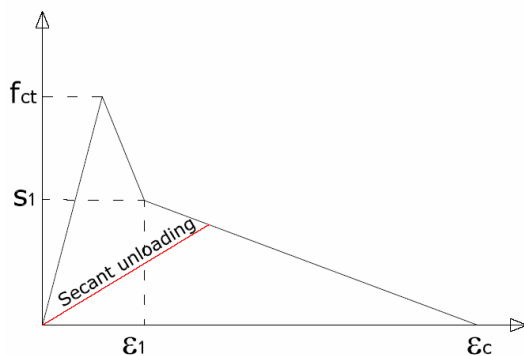


Figure 6-1: Secant unloading branch

This assumption is a simplification as in reality we may expect some residual strain upon closing the crack.

6.3.2 Total Strain crack models

This paragraph describes constitutive models based on total strain. These models describe the compressive and tensile behaviour in one σ - ε relation. The principle directions are uncoupled, so the linear elastic stress space is a cube.

The behaviour after cracking can be modelled in different ways. In DIANA the rotating crack model and the fixed crack model can be used.

Rotating crack

The rotating crack principle keeps the crack orthogonal to the principal stresses. To realise this, the crack will corotate with the principle stresses. By keeping the crack and the principle stresses orthogonal to each other, there will be no shear stress. Therefore a shear retention factor is not necessary. The model is numerically uncomplicated, but only realistic as long as the rotation of the crack is small. When the structure is subjected successively to two different load cases with load in different directions, large rotations of the cracks can occur, which leads to an unrealistic behaviour of the structure.

Fixed crack

In the Total Strain fixed crack model the crack does not corotate with the principle stresses. When a crack in a certain element has formed, the direction of this crack will not change during the rest of the load steps. For this reason, a change of the direction of the principle stresses will lead to shear stresses along the surface of the crack. To avoid numerical difficulties [12] and to improve the physical reality of the model (representation of the aggregate interlock), a reduced shear modulus βG ($0 \leq \beta \leq 1$) can be reinserted. This shear retention factor β can be constant or can be dependent on the crack strain.

Compressive behaviour

Concrete subjected to compressive stresses shows a pressure-dependent behaviour, i.e., the strength and ductility increase with increasing isotropic stress. Due to the lateral confinement, the compressive stress-strain relationship is modified to incorporate the effects of the increased isotropic stress. Furthermore, it is assumed that the compressive behaviour is influenced by lateral cracking.

In DIANA a refinement of the compressive behaviour in total strain models is possible by implementing confinement and/or implementing the influence of lateral cracking on the compressive behaviour. With the use of DIANA User's Manual [9], a description of these two phenomena is given below.

Confinement

In DIANA a refinement of the compressive behaviour in total strain models is possible by allowing higher compressive stresses due to lateral confinement.

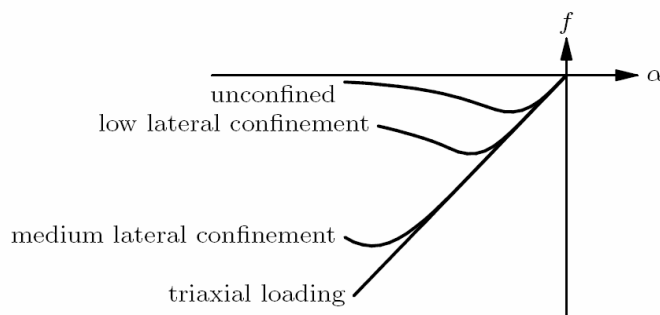


Figure 6-2: Influence of lateral confinement on compressive stress-strain curve (DIANA User's Manual)

The magnitude of the confinement is a function of the lateral compression stresses. The modification of the compression stress-strain curve is displayed in Figure 6-2. A description of the formulation is given in the DIANA User's Manual [9].

Compressive behaviour with lateral cracking

In cracked concrete, large tensile strains perpendicular to the principal compressive direction reduce the concrete compressive strength. The compressive strength of lateral cracked concrete is reduced. The parameters of the compressive stress-strain function f_{cf} and ε_p must be multiplied respectively by the reduction factors $\beta_{\sigma_{cr}}$ and $\beta_{\varepsilon_{cr}}$ so:

$$f_p = \beta_{\sigma_{cr}} \cdot f_{cf} \text{ and}$$

$$\alpha_p = \beta_{\varepsilon_{cr}} \cdot \varepsilon_p$$

With α_p the reduced strain at the reduced ultimate stress f_p in the compression stress-strain function. The reduction factors $\beta_{\sigma_{cr}} = \beta_{\sigma_{cr}}(\alpha_{lat})$ and $\beta_{\varepsilon_{cr}} = \beta_{\varepsilon_{cr}}(\alpha_{lat})$ are

functions the average lateral damage variable given by $\alpha_{lat} = \sqrt{\alpha_{l,1}^2 + \alpha_{l,2}^2}$ where $\alpha_{l,1}$ and $\alpha_{l,2}$ are the strains perpendicular to the compression direction. The relationship for reduction due to lateral cracking used in DIANA is the model according to Vecchio & Collins (1993). This model contains the following relations:

$$\beta_{\sigma_{cr}} = \frac{1}{1 + K_c} \leq 1 \text{ in which}$$

$$K_c = 0.27 \left(-\frac{\alpha_{lat}}{\varepsilon_0} - 0.37 \right) \text{ with } \varepsilon_0 \text{ the initial strain.}$$

The relation between the reduction factor $\beta_{\sigma_{cr}}$ and $\frac{\alpha_{lat}}{\varepsilon_0}$ is given in Figure 6-3.

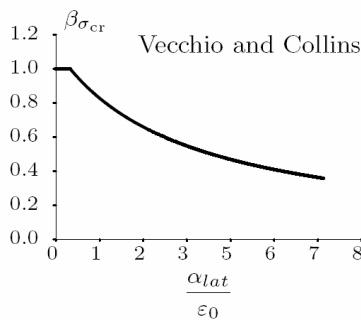


Figure 6-3: Reduction factor due to lateral cracking (DIANA User's Manual)

6.3.3 Drucker/Prager – Multi directional fixed crack

The Drucker/Prager – Multi directional fixed crack model is a combination of a yield model (Drucker/Prager) in compression and a crack model (Multi directional fixed crack) in tension.

Smearred cracking

The fundamental difference compared to the total strain crack models is the decomposition of the total strain ε into an elastic strain ε^e and a crack strain ε^{cr} as:

$$\varepsilon = \varepsilon^e + \varepsilon^{cr}$$

This decomposition of the strain allows for combining the decomposed crack model with for instance a plastic behaviour of the concrete in a transparent manner. It also allows the multi directional fixed crack principle. This principle is similar to the fixed crack principle, with the difference that after the first crack has been initiated a second crack can be formed when the angle between the first crack and the principle stress exceeds the value of the threshold angle α (Figure 6-4). In this way several cracks on different angles can be formed in one element.

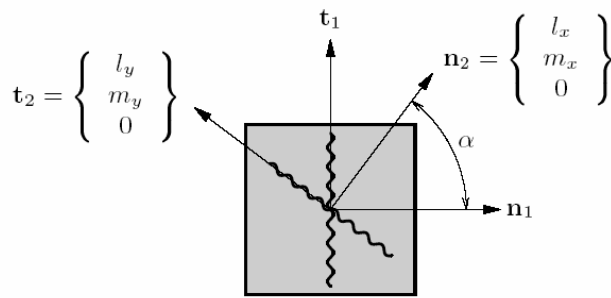


Figure 6-4: Multi-directional fixed crack model (DIANA User's Manual)

It is possible to apply a constant or a linear tension cut-off in DIANA. The tension cut-off describes the ultimate stress situation with tension in one or two directions. When a constant tension cut-off is applied, a compression stress in one direction has no influence on the allowable tension stress in the other directions (Figure 6-5a). With a linear tension cut-off a compression stress in one direction decreases the allowable tension stress in the other directions (Figure 6-5b). The real behaviour of concrete is somewhere in between.

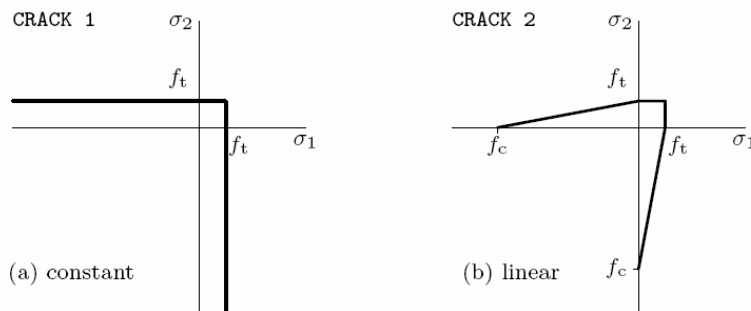


Figure 6-5: Tension cut-off in a two-dimensional principal stress space (DIANA User's Manual)

Drucker/Prager

The compression part of the model is defined by the Drucker/Prager yield criterion. The implementation of this yield function in DIANA is described in DIANA User's Manual [9].

6.4 Damage models

Damage models are similar to plasticity models, with the difference that the unloading does not occur elastically, but that the degradation of the elastic stiffness is taken into account in the unloading branch.

6.4.1 Concrete Damaged Plasticity

The concrete damaged plasticity model is implemented in ABAQUS for the analysis of concrete and other quasi-brittle materials. It consists of the combination of non-associated multi-hardening plasticity and scalar (isotropic) damaged elasticity to describe the irreversible damage that occurs during the fracturing process. The model describes the uni-axial tensile and compressive response which is characterized by damaged plasticity, as shown in Figure 6-6.

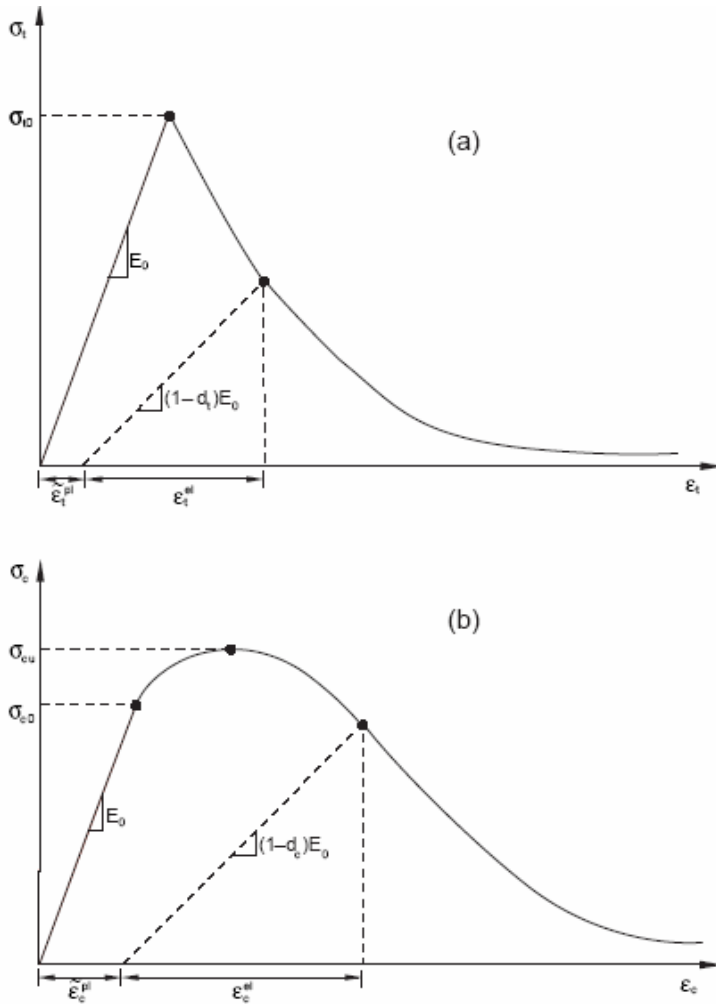


Figure 6-6: Response of concrete to uni-axial loading in tension (a) and compression (b)

The uni-axial tensile stress-strain response is linear elastic until the value of the failure stress, σ_{t0} . The softening branch starts after violating this value. The uni-axial compressive response is linear elastic until the value of initial yield, σ_{c0} followed by a hardening and a softening branch. In Figure 6-6 is shown that, when the concrete specimen is unloaded from any point of the strain softening branch of the stress-strain curves, the unloading response is weakened. The strain does not return to zero in an unloading situation, but some residual stress remains present. This is similar to the real behaviour of concrete.

The elastic stiffness is characterized by two damage variables d_t and d_c , which are functions of plastic strains (ε_c^{pl} , ε_t^{pl} equivalent plastic strain, $\dot{\varepsilon}_c^{pl}$, $\dot{\varepsilon}_t^{pl}$ the equivalent plastic strain rate, in Figure 6-6):

$$\sigma_t = \sigma_t(\varepsilon_t^{pl}, \dot{\varepsilon}_t^{pl}), \quad d_t = d_t(\varepsilon_t^{pl}, \dot{\varepsilon}_t^{pl})$$

$$\sigma_c = \sigma_c(\varepsilon_c^{pl}, \dot{\varepsilon}_c^{pl}), \quad d_c = d_c(\varepsilon_c^{pl}, \dot{\varepsilon}_c^{pl})$$

The damage variables can take values from zero, representing the undamaged material, to one, which represents total loss of strength. So, if E_0 is the initial undamaged elastic stiffness, the stress-strain relations under uni-axial tension and compression loading are respectively:

$$\begin{aligned}\sigma_t &= (1 - d_t)E_0(\varepsilon_t - \varepsilon_t^{pl}) \\ \sigma_c &= (1 - d_c)E_0(\varepsilon_c - \varepsilon_c^{pl})\end{aligned}$$

Under uni-axial cyclic behaviour, the concrete damaged plasticity model assumes that the reduction of the elastic modulus is given in terms of a scalar degradation variable d_0 as:

$$E = (1 - d_0)E_0,$$

where d_0 is the stiffness degradation variable that is a function of the stress state and the uni-axial damage variables d_t, d_c :

$$(1 - d_0) = (1 - s_t d_c) \cdot (1 - s_c d_t)$$

where s_t and s_c are functions of the stress state.

The stress-strain relations for the general three-dimensional multi-axial condition are given by scalar damage elasticity equation:

$$\overline{\sigma} = (1 - d_0) \overline{\overline{D_0^{el}}} (\overline{\varepsilon} - \overline{\varepsilon}^{pl}),$$

Where $\overline{\overline{D_0^{el}}}$ is the initial (undamaged) elasticity matrix and $\overline{\varepsilon}^{pl}$ the strain at the end of the elastic part of the stress-strain curve.

The previous expression for the scalar stiffness degradation variable, d , is generalized to the multi-axial stress state. d is now determined by a multi-axial weight factor, which is dependent on all principal stresses. The above given constitutive relation can be written as:

$$\begin{bmatrix} \sigma_{xx} \\ \sigma_{yy} \\ \sigma_{xy} \end{bmatrix} = \frac{E}{1 - \nu^2} \begin{bmatrix} (1 - d)1 & (1 - d)\nu & 0 \\ (1 - d)\nu & (1 - d)1 & 0 \\ 0 & 0 & (1 - d)^1 / 2(1 - \nu) \end{bmatrix} \begin{bmatrix} \varepsilon_{xx} - \varepsilon_{xx}^{pl} \\ \varepsilon_{yy} - \varepsilon_{yy}^{pl} \\ \gamma_{xy} - \gamma_{xy}^{pl} \end{bmatrix}.$$

The linear elastic stress space is described by plasticity model, so it is based on a yield surface. The yield surface of the Concrete Damaged Plasticity model is given in Figure 6-7.

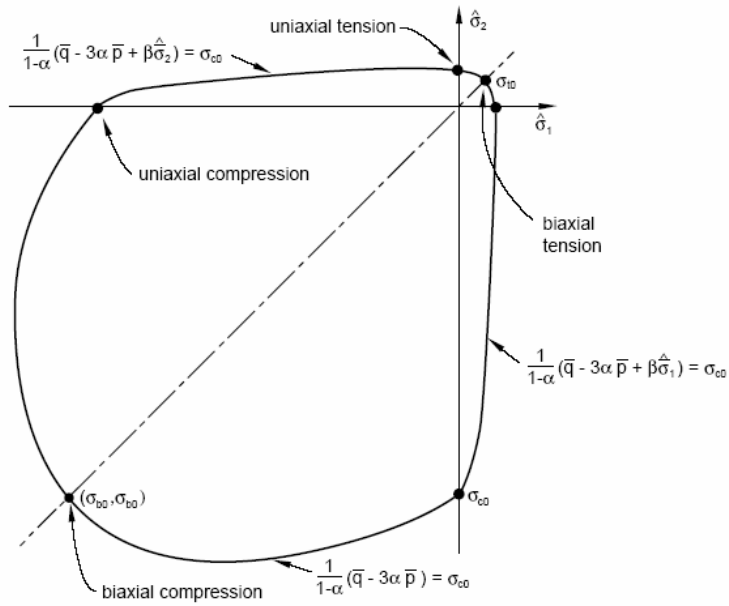


Figure 6-7: Yield surface of the Concrete Damaged Plasticity model in a plane stress situation

There can be noticed that, in a plane stress condition, the yield function presents a shape that is close to the real behaviour of concrete.

[1], [6], [9], [17]

7 Simulation of experimental tests

In Chapter 5 it has become clear that the way in which the material behaviour is modelled in a FEM program is of great influence of the result of the analysis. Therefore, a further investigation of the working of the material models is desirable. In Chapter 6 the backgrounds of the different models have been explained. This information is useful to explain, using also simulations of experimental tests, the behaviour of the material models.

This is done by simulating a four point bending test, a splitting test with line load and a splitting test with a point load with the material model as a variable.

In this chapter the different crack models which are available in DIANA and the concrete damaged plasticity model of ABAQUS are tested and compared. The following crack models are available in DIANA:

- Total strain rotating crack
- Total strain fixed crack
- Drucker/Prager + multi directional fixed crack

The models are described in Chapter 6. Within some models, modifications are tested and compared in this chapter.

Firstly, the uni-axial tensile behaviour is modelled with the two-dimensional notched beam model. The curve of the discrete crack model, which is in-between the experimental curves, is used as reference.

Section 7.2 contains the simulation of a splitting test with line load configuration, carried out by Schnütgen and Erdem [18]. A two dimensional mesh-model is made to gain insight in the bi-axial stress behaviour of the different material models in the disturbed zone.

An expansion to three dimensions is made in Section 7.3 by a splitting test with a point load configuration. In this case, the tri-axial stress situation in the disturbed zone can be analysed.

7.1 Four point bending test on a notched beam

In this paragraph, the four point bending test, which is described in Section 3.2, is modelled for different material models. The curve of the discrete crack model is used as reference. The mesh which is used to analyse the different material models is shown in Figure 7-1.

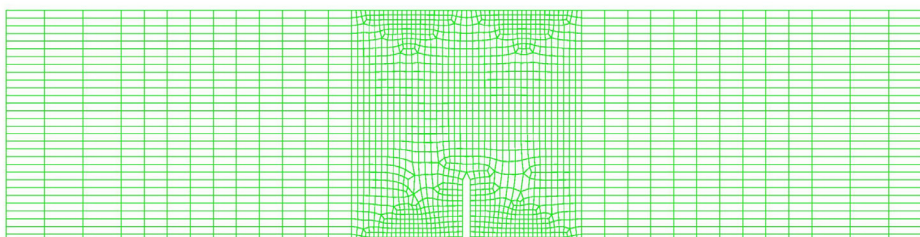


Figure 7-1: Mesh of the DIANA model of the notched beam

Cracking occurs by uni-axial tensile stresses in this simulation. The post cracking law is determined as follows:

The number of elements in this mesh is 2189 and the area is $600 \times 150 = 90000 \text{ mm}^2$. Therefore, the average area of an element is $90000/2189 = 41.1 \text{ mm}^2$. This mesh is a 2D mesh, so $l_c = \sqrt{A} = \sqrt{41.1} = 6.4 \text{ mm}$.

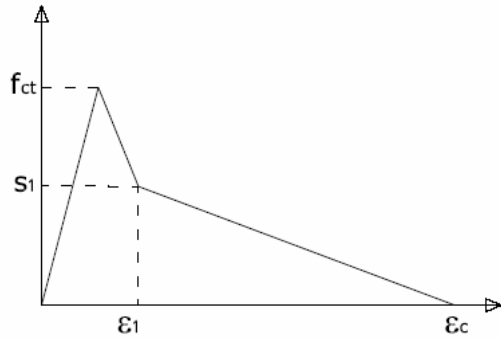


Figure 7-2: Bi-linear stress-strain law

The bi-linear softening function, which is presented in Section 3.2 is transformed into a σ - ϵ relation in Figure 7-2. The values which are used in this simulation are presented in Table 7-1.

Symbol	Value
f_{ct}	+4.1 MPa
S_1	+2.134 MPa
ϵ_1	0.00359375
ϵ_c	0.8359375
E_c	25000 MPa

Table 7-1: Material properties for the applied SFRC mixture

There must be noted that above used method is not very accurate for the above displayed mesh. This is because the element size differs significantly. The cracks will occur in the elements above the notch, which are smaller than the average. Therefore, the calculated post cracking parameters will show a stiffer behaviour than in reality.

7.1.1 Total strain rotating crack

The total strain rotating crack gives a good approximation of the discrete cracking curve (Figure 7-3) and is, for this reason, a suitable model to describe the uni-axial post cracking tensile behaviour of concrete.

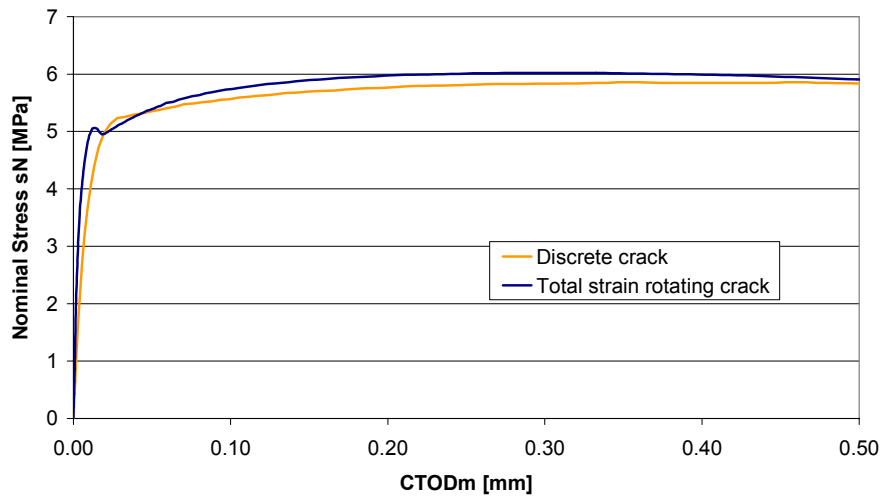


Figure 7-3: Simulation of the 4PBT by the total strain rotating crack model

7.1.2 Total strain fixed crack

Analyses with different values for β are done in order to study its influence. A simulation of the notched beam with the total strain fixed crack model with a shear retention factor of 0.2 is presented in Figure 7-4. This value for β is suggested by de Borst and Sluys [6] and by Frank J. Vecchio (0.1-0.2). The simulation seems to find stiffening, which is in reality not present. The stiffening seems to happen as a result of the reinserted shear modulus βG . Therefore, analyses with a low shear modulus ($\beta=0.01$ and $\beta=0.02$) and with without the reinserted shear modulus ($\beta=0$) are made.

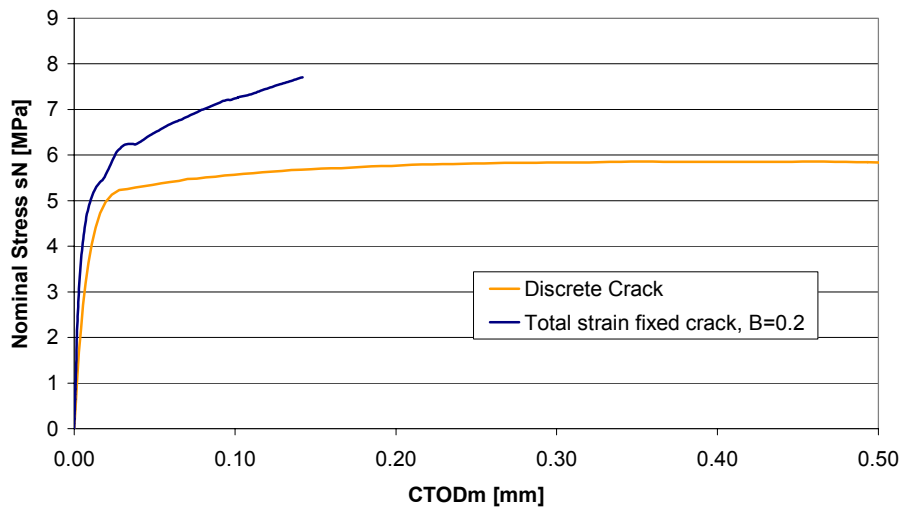


Figure 7-4: Simulation of the 4PBT by the total strain fixed crack model with $\beta=0.2$

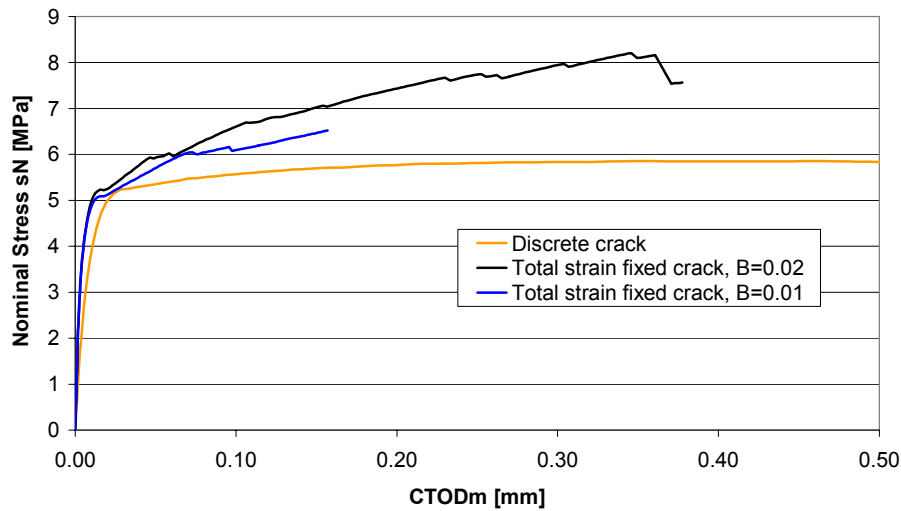


Figure 7-5: Simulation of the 4PBT by the total strain fixed crack model with $\beta=0.01$ and $\beta=0.02$

The stiffening reduces and the curve approaches the discrete cracking curve when the shear retention factor is reduced. This is visible in Figure 7-5 and Figure 7-6. While the β -value is reduced, numerical problems arise. Even though this applied mesh is very fine, very small steps are needed to find convergence.

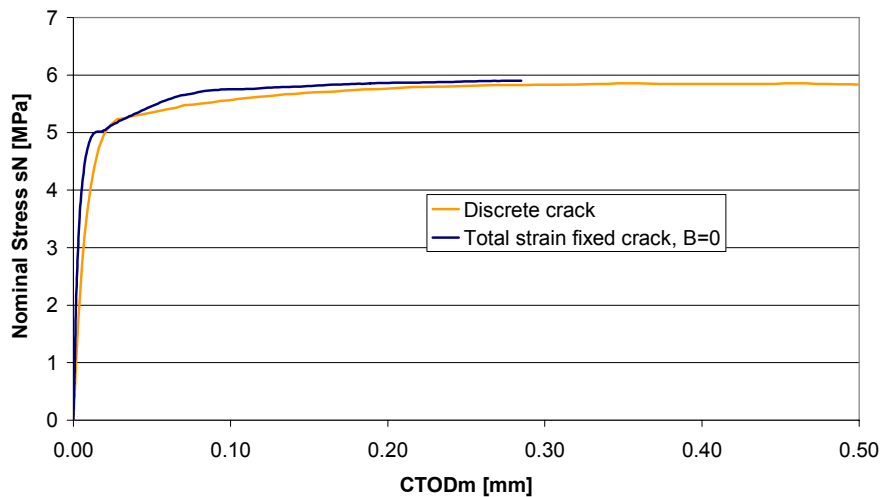


Figure 7-6: Simulation of the 4PBT by the total strain fixed crack model with $\beta=0$

Numerical stability is of great importance for the segment model, because this model is large and is built up of solid elements. Refining the mesh and applying small load steps can lead to an unacceptable long calculation time.

7.1.3 Drucker/Prager – Multi directional fixed crack

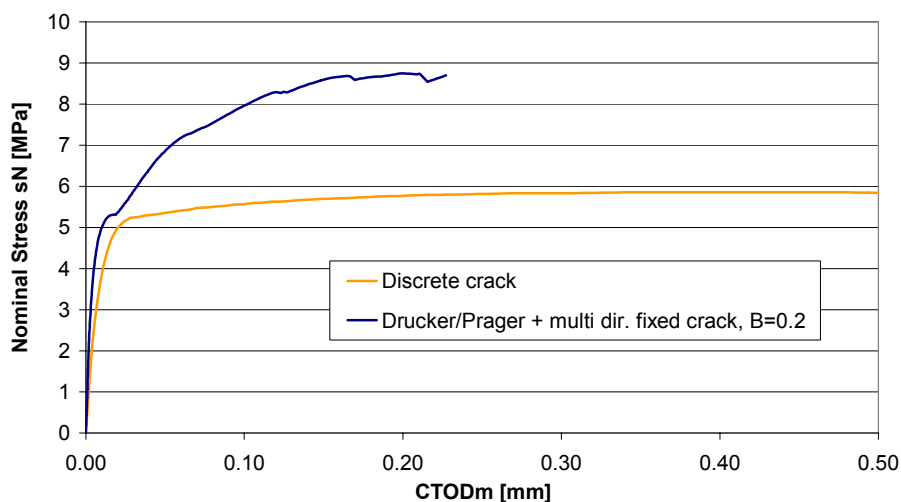


Figure 7-7: Simulation of the 4pbt by the total strain fixed crack model with $\beta=0.2$

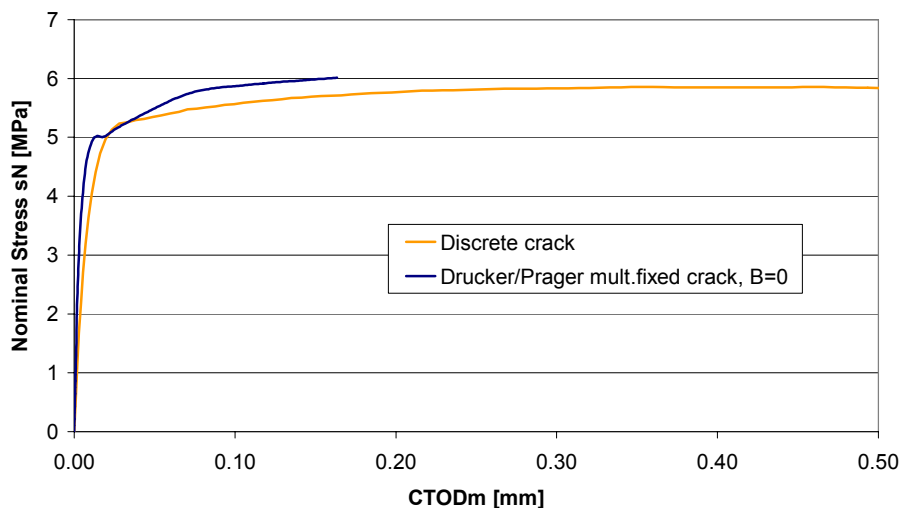


Figure 7-8: Simulation of the 4pbt by the total strain fixed crack model with $\beta=0$

The results with this model are comparable to the total strain fixed crack. When a shear retention factor of 0.2 is used, the response after cracking is too stiff and a shear retention factor of 0 leads to a close approximation, but involves numerical difficulties. As there appear only cracks by uni-axial tensile stresses in the notched beam simulation, the difference between linear and constant tension cut off is not tested. The simulations are carried out with the default settings with respect to the tension cut off, which is the constant tension cut-off.

7.1.4 Concrete Damaged Plasticity – ABAQUS model

Because of the large computational time of the ABAQUS analyses, the results of non-linear FEM simulations done by Tiberti [20] in Brescia University are used. For this simulation a 3D mesh as shown in Figure 7-9 is used.

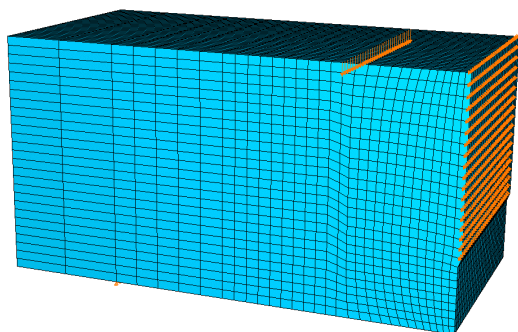


Figure 7-9: Mesh of the notched beam model in ABAQUS

This simulation is presented in Figure 7-10 and gives a satisfying approximation of the discrete cracking curve.

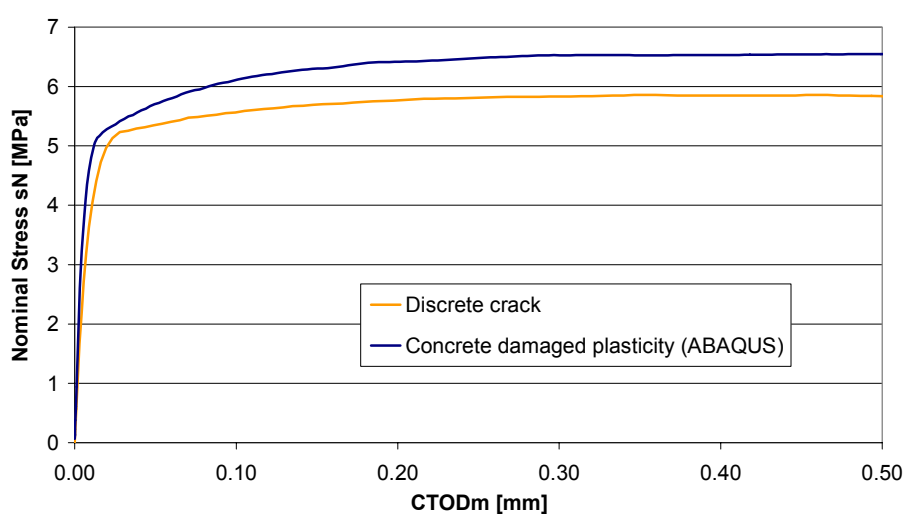


Figure 7-10: Simulation of the 4PBT by the concrete damaged plasticity (ABAQUS)

It can be concluded that the total strain rotating crack model of DIANA and the concrete damaged plasticity model of ABAQUS give satisfying approximations of the four point bending test. The approximations of the total strain fixed crack model and the Drucker/Prager + multi directional fixed crack are dependent on the shear retention factor. A satisfying approximation with these models is accompanied by numerical difficulties.

7.2 Splitting test with line load

While in Section 7.1 the simulation of the uni-axial tensile behaviour of the different material models is presented, a simulation concerning a bi-axial stress situation is done in this section. This is done by a simulation of a splitting test with a line load configuration. Splitting stresses in the disturbed region occur in this experiment.

The reference is an experimental splitting test with a line load, carried out by Schnütgen and Erdem. Five LVDT's on different distances of the load surface are placed to measure the displacement in the direction perpendicular to the line load (Figure 7-11).

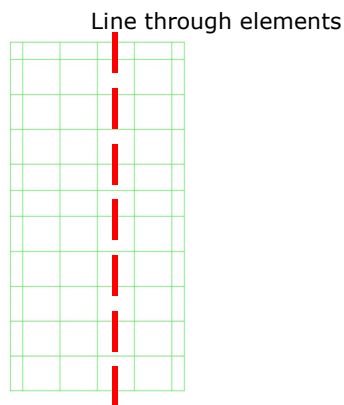


Figure 7-12: Two-dimensional mesh used to simulate the splitting test with line load

A 2D model is made with 4-node plane stress elements in DIANA (Figure 7-12). For the Total Strain rotating crack model, all five graphs of the LVDT's are added in the report. For reasons of similarity, for the rest of the models only LVDT 2 is added in the report.

An elastic analysis is made to get insight in the elastic stress distribution in the disturbed zone. The elastic stress in x-direction along a line through elements in the centre of the specimen (Figure 7-12) is plotted in a graph. This line is plotted in through elements, because DIANA calculates the stresses in the points of Gauss and with a line through elements the average of the Gaussian stresses per elements is plotted. In the same graph the stress distribution according to the elastic theory, reported by Leonard, in the disturbed zone is given. The curves of DIANA differ little from the elastic solution. This is because of the coarseness of the mesh.

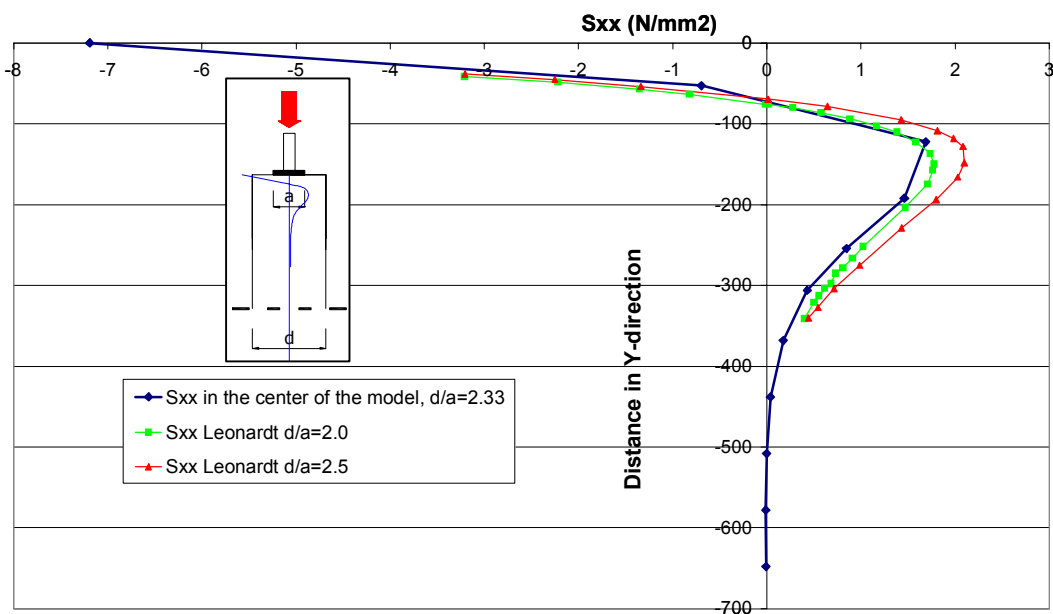


Figure 7-13: Graph of stresses in x-direction along a line through the centre of the model

The theoretical background of the disturbed zone can be found in the Literature Survey.

7.2.1 Total strain rotating crack

The graphs of the LVDT's obtained with the Total Strain rotating crack model are given in Figure 7-14.

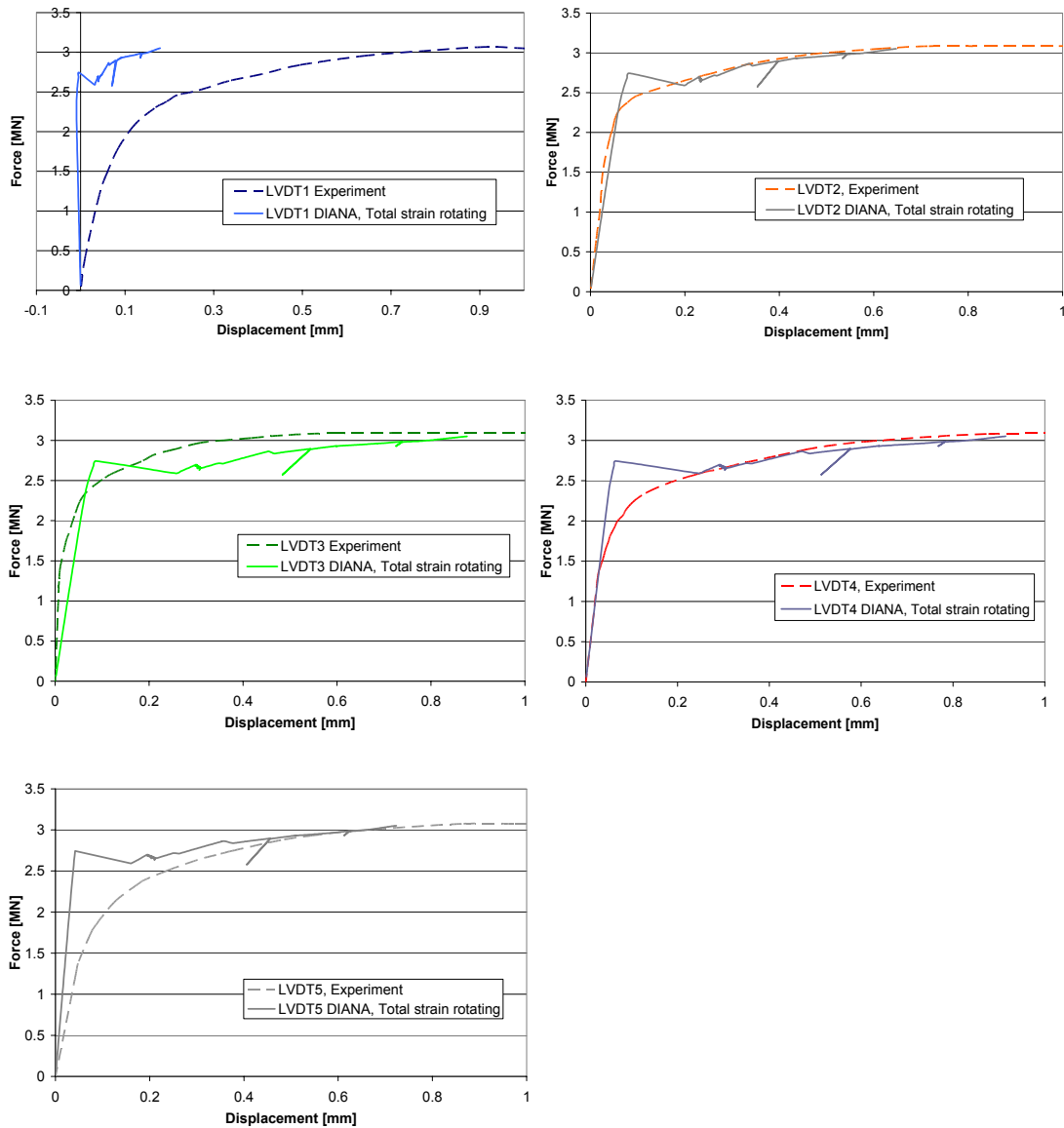


Figure 7-14: Graphs of the LVDT's of the experimental test and the total strain rotating crack model

The curves of LVDT 2, 3 and 4 of this model are quite close to the experimental curves and the ultimate load is nearly the same. As the material properties are not equal and the experimental results have a certain scatter, an approximation this close must be seen as a matter of coincidence.

The numerical curves of LVDT 1 and 5 show larger differences with the experimental results. The mayor reason for this difference is the mesh refinement. The mesh is very course, which influences the location of the disturbed zone. At the location of LVDT 1 DIANA seems to have compression in the direction perpendicular to the load, while the in experiment LVDT1 is in the tension zone.

LVDT5 seems to be (almost) outside of the disturbed zone and shows for this reason very small displacements before cracking. After cracking, the numerical and the experimental curves are closer to each other.

7.2.2 Drucker/Prager + Multi directional fixed crack

There are four simulations of the experiment by the Drucker/Prager + multi directional smeared cracking model. Two simulations to investigate the difference between constant and linear tension cut off and two simulations to investigate the influence of the shear retention factor.

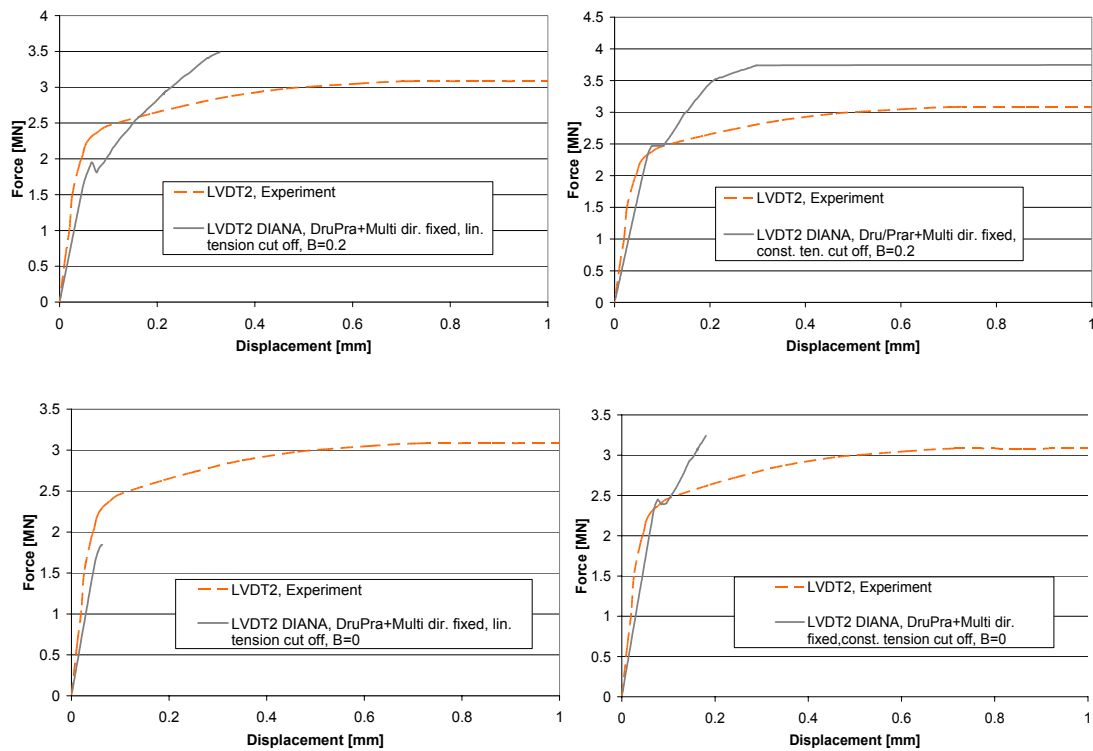


Figure 7-15: Graphs of LVDT2 for the experimental test and Drucker/Prager + multi direction fixed crack

For the Drucker/Prager + multi directional fixed crack model, a similar behaviour is found as in the four point bending test.

When a shear retention factor of 0.2 is applied, the slope after cracking is steeper. When a linear tension cut off is applied, cracking occurs at a lower load and the stiffness after cracking is lower.

When no shear retention is applied, the curve is less stiff and, as in the four point bending test, numerical problems occur. Very small steps must be applied to let the analysis go on.

7.2.3 Total strain fixed crack

For the Total Strain fixed crack model the results for $\beta=0$ and $\beta=0.2$ are approximately the same. For this reason only the graph for $\beta=0$ is added in the report.

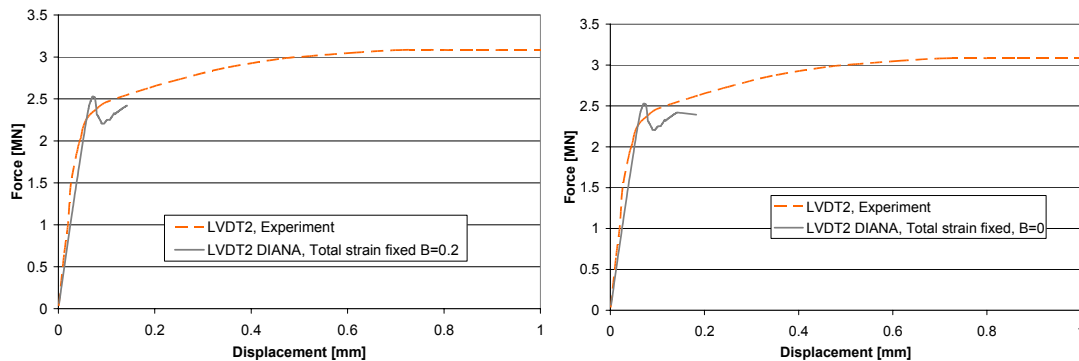


Figure 7-16: Graphs of LVDT2 for the experimental test and total strain fixed crack

The Total Strain fixed crack with no shear retention shows a similar behaviour as the Drucker/Prager + Multi directional fixed crack with a constant tension cut of and $\beta=0$ crack before cracking. After cracking, the total strain fixed crack model finds a change of slope, which is reasonably close to the experimental curve. The remaining disadvantage of this model is the numerical instability due to the absence of the shear retention factor.

7.2.4 Concrete Damaged Plasticity

A two-dimensional mesh with the same mesh refinement has been created for an ABAQUS analysis.

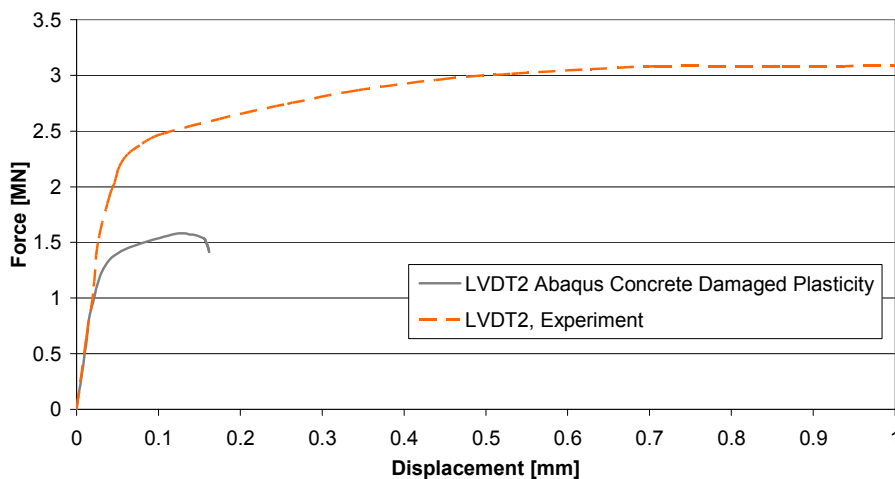


Figure 7-17: Graph of LVDT2 for the experimental test and concrete damaged plasticity

The Concrete Damaged Plasticity model reaches a much lower ultimate load than the experiment. From Figure 7-17 it becomes clear that the curve bends off at a very low load.

This is a result of the fact that this model is an isotropic plasticity model and not a crack model. The concrete damaged plasticity model has a different behaviour as a crack model in a multi-axial stress situation. A crack model distinguishes different modulus of elasticity in the direction perpendicular to the crack and the direction in plane of the crack, whereas in this plasticity model the total stiffness matrix is degraded by a scalar between zero and

one. Therefore, the degradation of the stiffness occurs not only in the direction in which the tensile strength is reached, but in all directions.

In the splitting test with a line load this means that, as soon as the first splitting crack occurs by tensile stresses perpendicular to the direction of the load, softening occurs in the direction of the load too.

From the above mentioned it can be concluded that the concrete damaged plasticity model and isotropic damaged plasticity models in general are not suitable to model concrete cracking in a multi-axial stress situation. The Total Strain rotating crack model is considered as the best of the tested models, because it approximates the experiments in a good way without numerical difficulties.

7.3 Splitting test with point load

The model of the tunnel segment is a 3D model. Therefore an expansion to three dimensions is made by a splitting test with a point load configuration. The configuration of the 3D splitting test is presented in Figure 7-18. In this case the tri-axial stress situation in the disturbed zone can be analysed. As in the splitting test with a line load, LVDT's are placed on the vertical sides of the specimen. Also here, the aim of the LVDT's is to measure the development of bursting cracks.

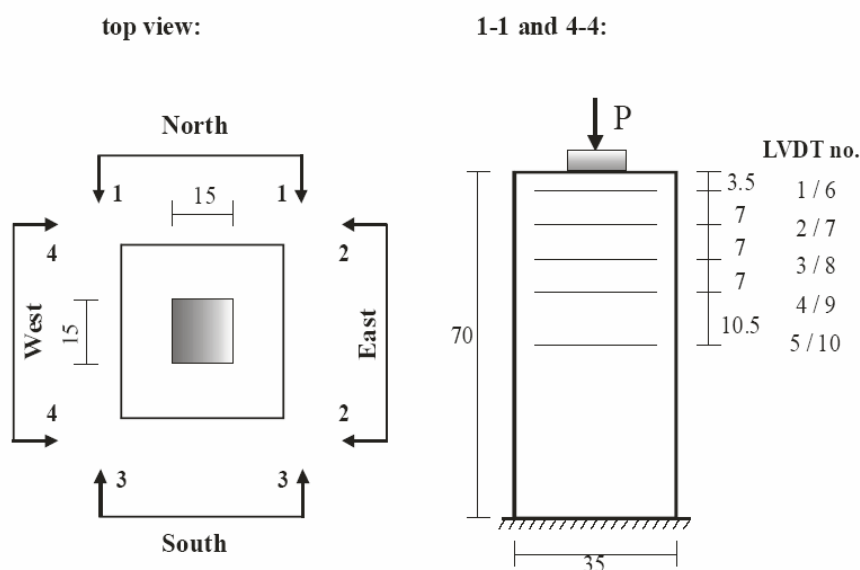


Figure 7-18: Configuration of the splitting test with point load

The experiment is carried out with a C50/60 concrete with 60 kg/m^3 of RC 65/60 steel fibres (60 mm long DRAMIX hooked-end steel fibres with an aspect ratio of 65). Since there are no post-cracking properties available for this type of concrete, the simulations have been done with a C50/60 concrete with 45 kg/m^3 Wirand FF1 steel fibres with a fibre length of 50 mm and a aspect ratio of 50 (Paragraph 3.1.1). Since the material properties are not exactly the same, a close approximation can not be expected. The aim of this simulation is to know if with a numerical model a similar curve as in the experiment can be reached.

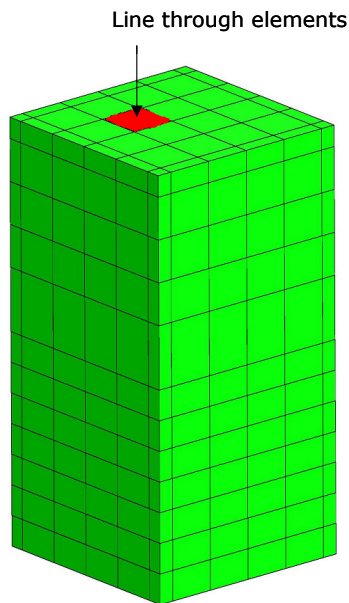


Figure 7-19: Three dimensional mesh used to simulate the splitting test with point load

The DIANA model is given in Figure 7-19. The model consists of 20-node brick elements. 2-node elements are used, because the mesh is coarse and, when 8-node elements are applied, the analysis does not find a change of slope of the LVDT curves.

In the previous section it is concluded that the Total Strain rotating crack model is the most suitable material model for the uni-axial and the bi-axial simulation of concrete cracking. Therefore there is chosen to use this model for the simulations of the tunnel segment in this thesis. The splitting test with a line load is a last check and is only done with the Total strain rotating crack model.

The experimental test reaches an ultimate load of approximately 2 mN. A simple calculation shows that the compression stress under the load is higher than the compressive strength: $2 \cdot 10^6 / (150 \cdot 150) = 88.9 \text{ N/mm}^2$. Therefore it is not possible with the normal Total Strain rotating crack model to simulate this experiment in a proper way.

In the simulations of the splitting test with a point load the possibility of higher compressive stresses due to lateral confinement has been implemented. Using this modification of the model, a higher compressive stress is allowed in regions with lateral compressive stresses. Furthermore, it is possible to have a closer approximation of the true behaviour of concrete under compression by implementing a reduction of the allowable compressive stress due to lateral cracking [9]. A simulation with- and without the latter modification is made to get insight in the influence of this aspect.

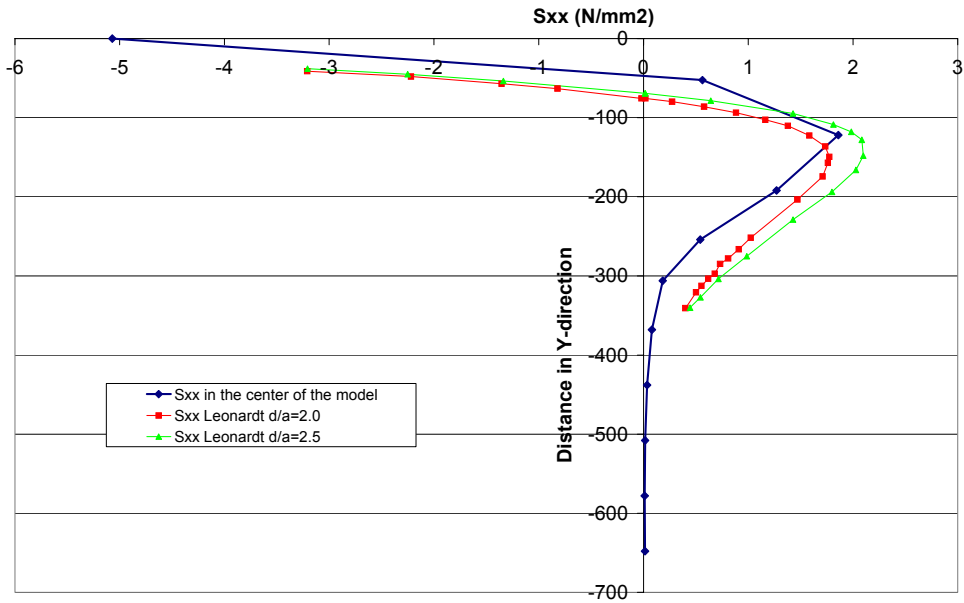


Figure 7-20: Graph of stresses in x-direction along a line trough the centre of the model

In Figure 7-20 a graph is given of the stresses (S_{xx}) in horizontal direction in the linear elastic situation on a line trough the centre of the model, over the height of the model. As presented in Figure 7-19, this line is a line through elements. This is done in order to have the stresses plotted in the points of Gauss. As the model is symmetric, the stress distribution in the other horizontal direction is exactly the same. The numerical curve is compared with the elastic solution for a 2D disturbed region condition.

The load-displacement curves of the LVDT's for the Total Strain rotating crack model without modification are given in Figure 7-21 until Figure 7-25.

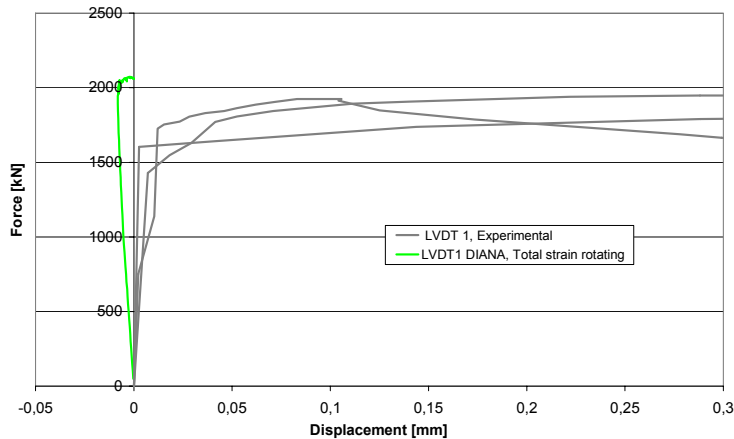


Figure 7-21: Graph of LVDT1 for the experimental test and total strain rotating with confinement

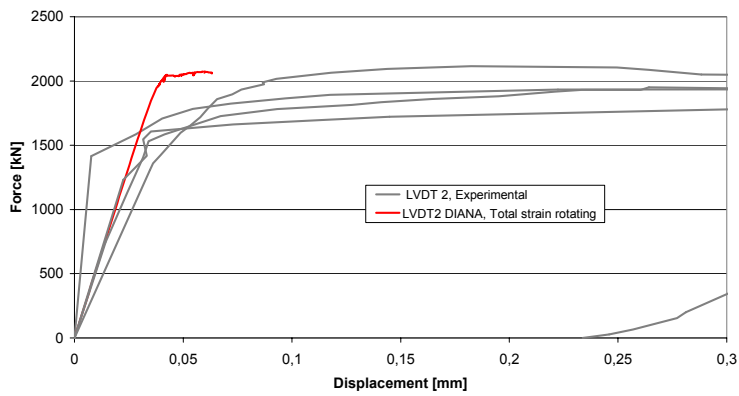


Figure 7-22: Graph of LVDT2 for the experimental test and total strain rotating with confinement

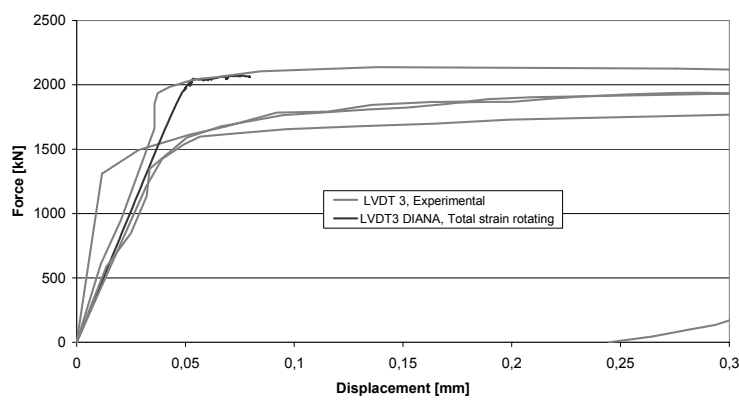


Figure 7-23: Graph of LVDT3 for the experimental test and total strain rotating with confinement

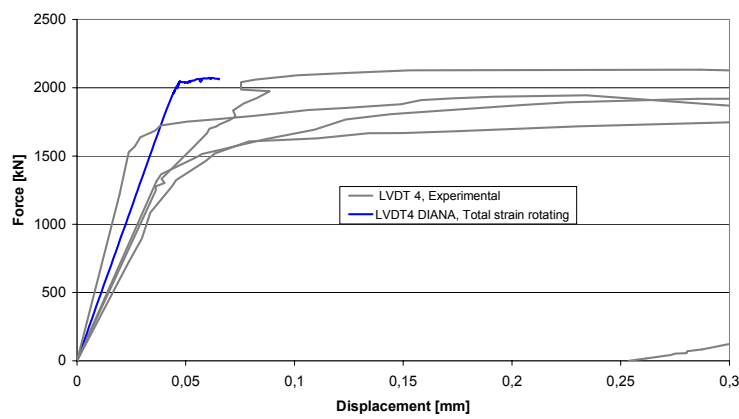


Figure 7-24: Graph of LVDT4 for the experimental test and total strain rotating with confinement

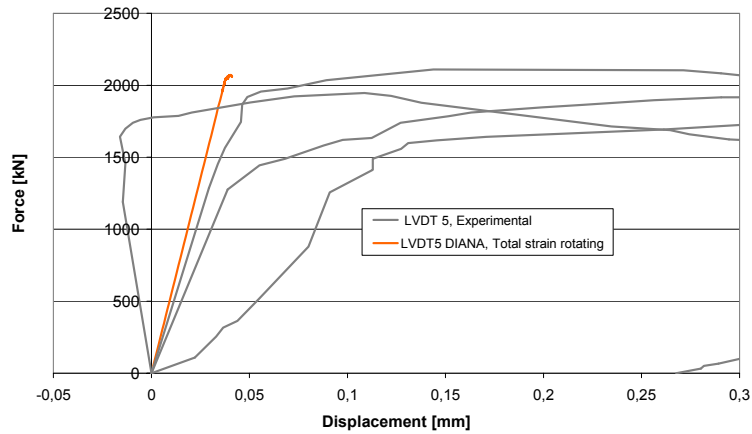


Figure 7-25: Graph of LVDT5 for the experimental test and total strain rotating with confinement

The Total Strain rotating crack model with confinement has a short horizontal part of the curve at 2.07 mN. This is high in comparison to the experimental results, because in the experiment a higher amount of fibres has been applied. Another difference is that numerical curves bend off at a relatively high load. This could be clarified by the fact that the principal stress directions in the total strain rotating model are uncoupled. The cube, which is the linear elastic stress space of the Total Strain rotating crack model, contains more space than the real linear elastic stress space of concrete. For this reason, in this model the yield contour is reached later in a multi axial stress situation.

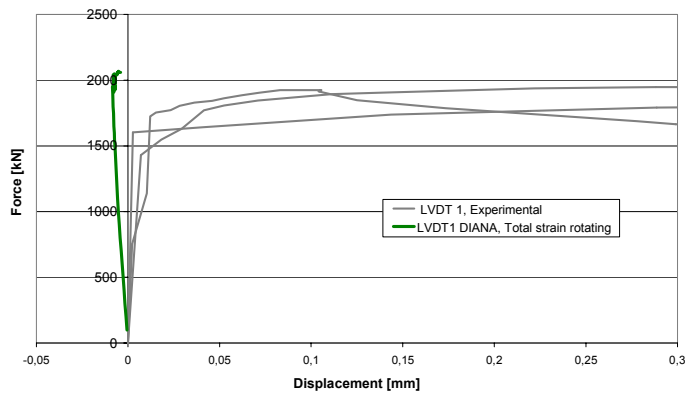


Figure 7-26: Graph of LVDT1 for the experimental test and total strain rotating with confinement and reduction

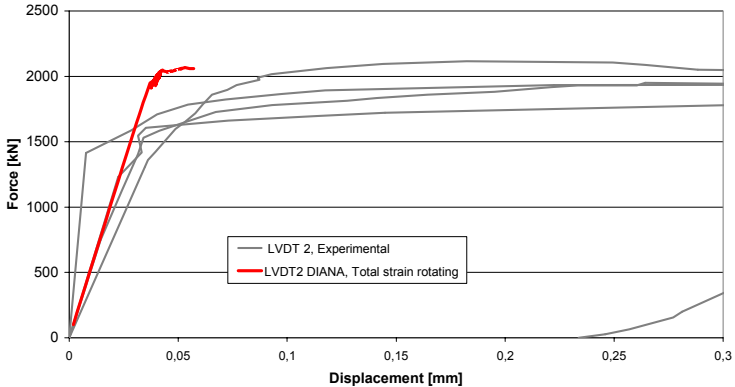


Figure 7-27: Graph of LVDT2 for the experimental test and total strain rotating with confinement and reduction

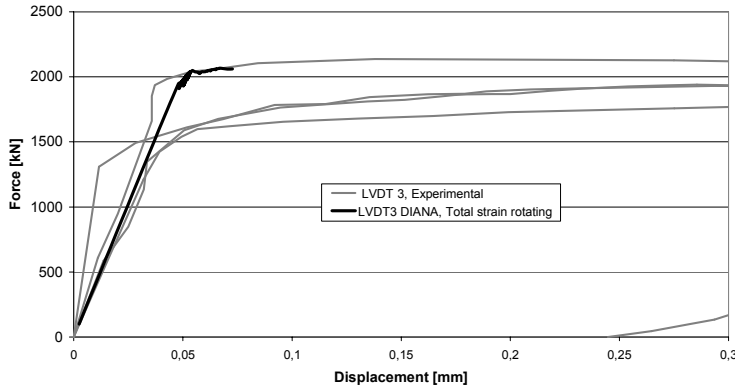


Figure 7-28: Graph of LVDT3 for the experimental test and total strain rotating with confinement and reduction

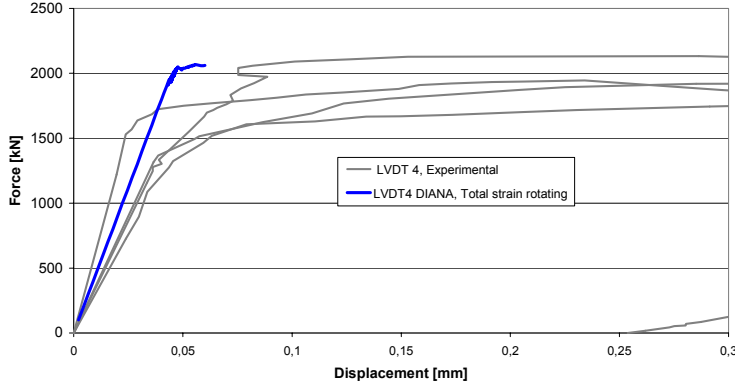


Figure 7-29: Graph of LVDT4 for the experimental test and total strain rotating with confinement and reduction

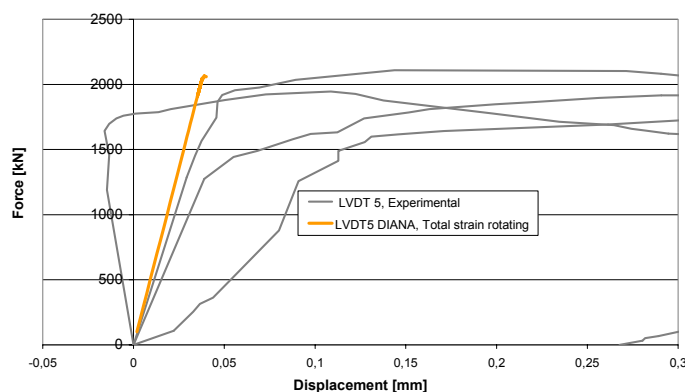


Figure 7-30: Graph of LVDT5 for the experimental test and total strain rotating with confinement and reduction

The curves of the model with reduction due to lateral cracking (Figure 7-26) do not show any difference from the curves of the model without this modification. Probably the stress situation where the compressive strength decreases does not occur in this experiment. As it is not clear from this comparison what the application of the reduction of the compression strength due to lateral cracking does, it is not applied in the simulations of the tunnel segment in the later chapters of this thesis.

7.4 Conclusions with respect to the material models

Approach of the behaviour of concrete

The Total Strain rotating crack model is the simplest one and the least realistic one. The fact that the crack corotates with the principle stresses is unrealistic and the principle stress directions are uncoupled, which makes the model different from the real behaviour of concrete. The Total Strain fixed crack model describes the behaviour of concrete in a better way, because the cracks do not rotate after initiating. Even more realistic is the Drucker/Prager + multi directional fixed crack principle. More than one crack can occur in this model and linear tension cut off is a closer approach on the safe side compared with the Total Strain models. The Concrete Damaged Plasticity model is the most realistic model that is used in this thesis. The model is similar to the Drucker/Prager + multi directional fixed crack model, but it has a more realistic unloading branch.

Multi-axial post cracking behaviour

While the Concrete Damaged Plasticity model approaches the real behaviour of concrete the best, it fails in a multi-axial stress state. This is because the scalar damage factor, which multiplies the total stiffness matrix by a factor smaller than one. The constitutive law shows the same softening relation in all directions, which is completely different from the real behaviour of concrete. In a uni-axial stress state, this difference is not experienced, because there is no stress in the directions tangential to the crack. Therefore, the concrete damaged plasticity gives a good result in the simulation of the four-point-bending-test. When it comes to the splitting test with a line load, the concrete damaged plasticity model does not give good results. This is because there is a bi-axial stress situation in this case. There is a compressive stress in the direction of the load and a tensile splitting stress perpendicular to the load-direction. Whereas only the stiffness in the direction perpendicular to the load-direction is multiplied by a softening function in a crack model, all terms of the stiffness matrix are multiplied by the degradation factor in the Concrete damaged plasticity model. The result is softening in the direction of the load, which is in reality not present. Therefore, the Concrete Damaged Plasticity model is not suitable to model concrete cracking in a multi-axial stress state.

The smeared cracking models all have orthotropic softening and are therefore suitable to model a multi-axial stress state. The Drucker/Prager + multi directional fixed crack model has the advantage of choosing between a constant and a linear tension cut off. The linear tension cut off is a safe approach and the constant tension cut off is an unsafe approach. The reality is in-between constant and linear tension cut off.

Numerical stability

When the material models are subjected to analyses, it becomes clear that the shear retention factor, which is present in the Total Strain fixed crack model and the Drucker/Prager + multi directional fixed crack model, causes problems. The numerical stability increases when an increased value of β is used, but at the same time the approximation becomes worse when β is increased. The use of a material model in which β is present leads either to a bad approximation or numerical difficulties. The Total Strain rotating crack model does not have this problem, because with the rotating crack principle there cannot occur shear stresses along the crack.

Total Strain rotating crack

The Total Strain rotating crack model is a simple model. It is not close to the real behaviour of concrete, because the principle stress directions are uncoupled and the cracks can rotate during the analysis. The simplicity of this model is at the same time a large advantage. It makes the model numerically much more stable than the other mentioned models. The numerical stability is a very important feature of a material model, because instable models take a lot of time from the engineer. The rotations of the cracks are in most cases very small, so they have only little influence on the behaviour of the analysis. The uncoupling of the principle stress directions makes the tension-compression (or tension-tension-compression in 3D) behaviour stronger than the real behaviour of concrete, but, looking at the analyses of the experiments, this seems to have only small influence.

The Total Strain rotating crack model is suitable to model SFRC in a uni-axial and multi-axial stress state. The model is understandable and numerically stable. The model does not give a very close approximation of the real behaviour of concrete, but the approximation is reasonable and in most cases crack simulations are used to show differences and principles, not design calculations.

The limitation of the Total Strain rotating crack model is that large rotations cause an unrealistic behaviour. This makes it impossible to do an analysis in which different loading cases are put subsequently on the mesh-model (phased analysis).

The simulations of the tunnel segment in this thesis are done with the Total Strain rotating crack model. Within this model the possibility of higher compressive stresses due to lateral confinement is applied.

Analysing the simulations of the tunnel segment, there must be noted that also the Total Strain rotating crack model is not completely stable. Therefore, it might happen that the analysis stops because of numerical reasons, instead of collapse of the structure. Even though the analyses present an ultimate load, these must be interpreted as indications, not as exact values.

8 Calibration of the model

Before making non-linear FEM simulations, one must define a model that represents the reality properly. The model must represent the reality as good as possible, but must also be understandable for the user. In non-linear FEM simulations the calculation time is an important factor too.

In this chapter the choice of the element type and the boundary conditions is explained. The aim is to define a model which is reasonably close to the reality, understandable for the user and uses only a few hours for a simulation.

8.1 Choice of the element type

The segment model consists of solid elements. Solid elements have the tendency to produce a large system of equations. In a non-linear analysis with many iterations times several load steps, this leads to a long calculation time. therefore it is desirable to use an element type and mesh refinement in such a way that a good approximation with a minimum calculation time is reached. There are different solid element types available in DIANA. The most applied types are tetrahedric elements and brick elements. Brick elements are chosen for the smooth segment model. This is done because a mesh with this element type has a higher number of Gauss-points with the same number of degrees of freedom. This results in a high accuracy with a relatively small system of equations. Another advantage with respect to tetrahedric elements is that there are no problems with the aspect ratio. A large aspect ratio (the ration between the lengths of the sides of the elements is large) leads to convergence problems and a bad accuracy. The model with irregularities can not be described with brick elements. Tetrahedric elements are applied in this case. A more fine mesh will is applied here.

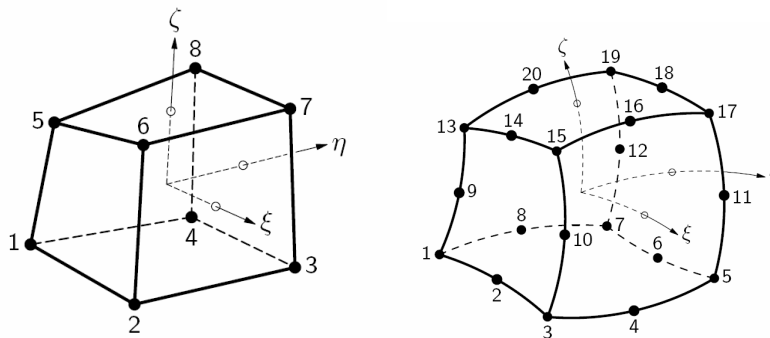


Figure 8-1: Element types; 8-node linear (left) and 20-node parabolic (DIANA User's Manual)

Brick elements are applicable with eight or 20 nodes (see Figure 8-1). The eight-node element has a $2 \times 2 \times 2$ integration scheme (eight points of Gauss) and linear shape functions, whereas the 20-node element has a $3 \times 3 \times 3$ integration scheme (27 points of Gauss) and parabolic shape functions. With the computer, which is used for the FEM analyses for this thesis, an analysis with eight-node elements has a duration of approximately four hours, whereas an analysis with 20-node elements has a duration of approximately four days. Therefore it is desirable to use eight-node elements. In this paragraph a comparison is made between eight-node and 20-node elements. The goal is to have a good agreement between the two element types. A good agreement means that the eight-node element gives a good approximation and no further refinement is necessary.

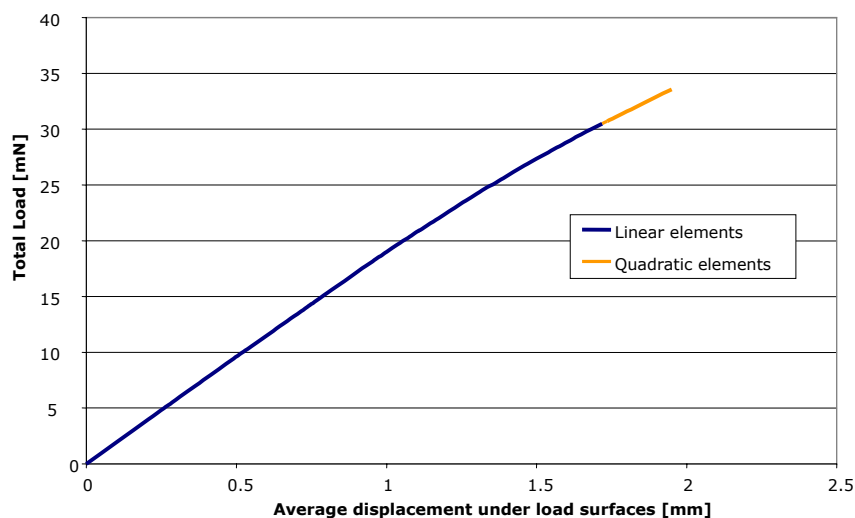


Figure 8-2: Load vs. displacement curves for eight-node and 20-node elements

The curves which describe the total load versus the average displacement on the load surfaces are presented in Figure 8-2. The curves follow the same path, but the ultimate load of the curve of the model with 20-node elements is approximately 10% higher than the curve of the model with eight-node elements.

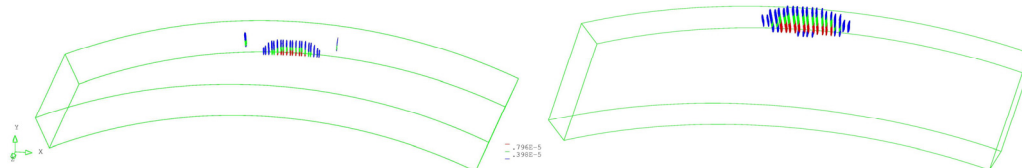


Figure 8-3: First crack for the analysis with 20-node elements (left) and with 8-node elements (right)

The first crack, which is between the load surfaces (Figure 8-3), occurs in both analyses approximately at the same load level, namely 7.0 (20-node elements) and 6.5 mN (eight-node elements).

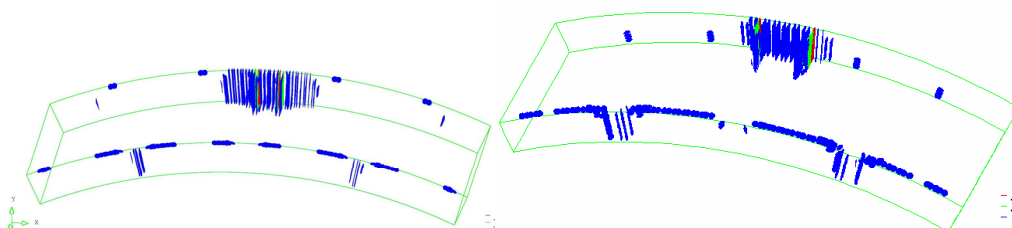


Figure 8-4: Third crack for the analysis with 20-node elements (left) and with 8-node elements (right)

The load levels, on which the second crack occurs, differ significantly. The model with 20-node elements shows cracks at the supports at a load level of 9.92 mN, whereas the model with 8-node elements at 14.2 mN. These cracks appear at the support side. The third location on which cracks appear is near the thrust jacks. Again the cracks appear earlier in the model with the 20-node elements, namely at 13.2 mN, whereas they appear

at 17.7 mN in the model with 8-node elements. The second and third crack locations are visible in Figure 8-4.

The difference in load level is caused by the difference mesh refinement of this region. The 8-node elements give a less accurate approximation. In this case this leads to lower stresses, so cracks occur at a higher level. This difference is local and has no influence on the global behaviour of the segment.

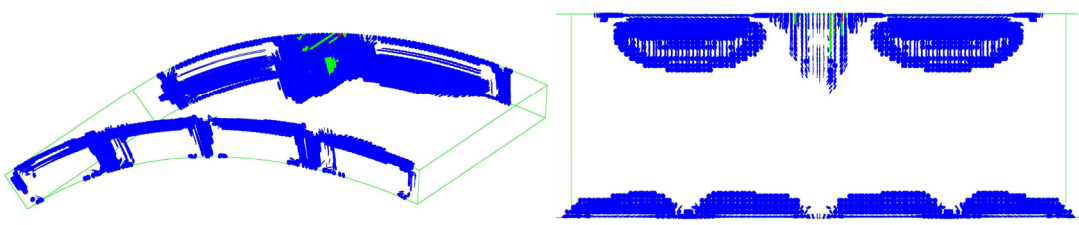


Figure 8-5: Crack pattern of the model with 20-node elements at 30.0 mN

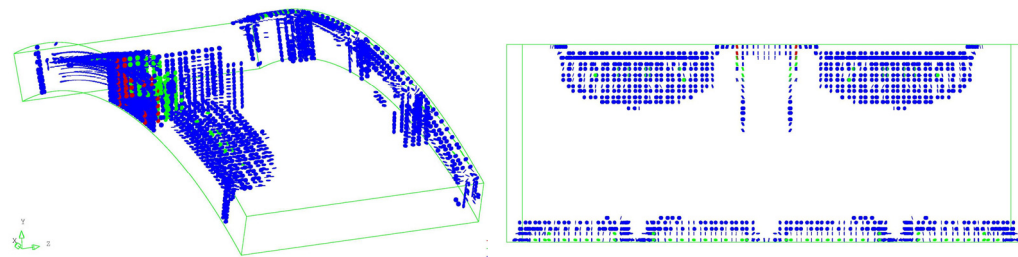


Figure 8-6: Crack pattern of the model with 8-node elements at ultimate load (30.7 mN)

The crack patterns at approximately 30 mN are mainly the same. The pictures show a difference in density of the cracked zones, but this is graphical property of DIANA. The 20-node elements have more locations where a crack can occur, so the pictures show a denser crack pattern.

With the graphs in Figure 8-7 and Figure 8-8 the difference in crack development is studied in more detail. Figure 8-7 shows the development of the cracks in radial direction in the bursting zone underneath the loading surfaces.

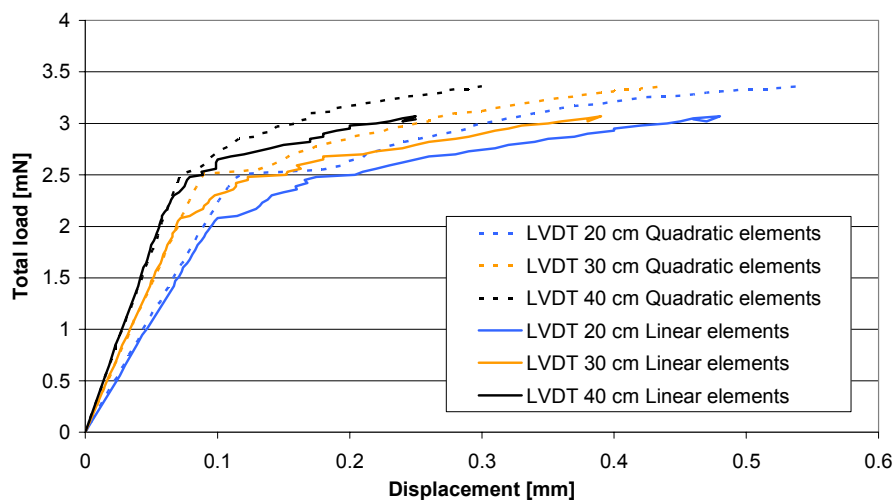


Figure 8-7: Total load vs. displacement in radial direction in the bursting zone

The model with 20-node elements shows cracks near the edges in an earlier stage (Figure 8-4), the development of the bursting cracks underneath the loads (Figure 8-7) shows that these cracks develop earlier in the model with 8-node elements.

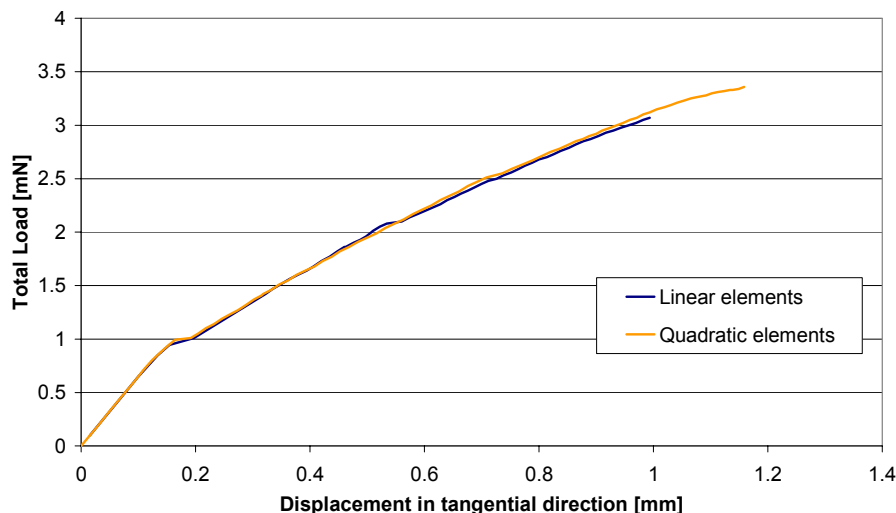


Figure 8-8: Total load vs. displacement of the spalling crack for linear and parabolic elements

The development of the spalling cracks in the two models is approximately the same. Figure 8-8 shows that the total crack width in this region is approximately the same, whereas the crack patterns in Figure 8-5 and Figure 8-6 show a little different shape of the cracks in this area.

The two compared models show differences in crack development and ultimate load of an order of 10% (30% locally, on the edges). The purpose of this thesis is to show principles and not to predict exactly the crack development. A very close approximation can not be expected, because the loading situations have been estimated, the material model does not give an exact description of the reality and other assumptions and simplifications have to be done in order to keep the model understandable. For this reason, small differences in FEM approximation of the mesh (10%) are accepted in this thesis. The advantage of a much shorter calculation time of the model with 8-node elements makes this element type more attractive for this thesis. Therefore the following analyses are made with this element type.

8.2 Choice of the boundary conditions

8.2.1 Support of the ring joint in z-direction

The aforementioned model contains rigid supports in x- y- and z-direction in the ring joint. In reality, this is not the case. The supporting ring acts as an elastic support and does not give tension forces. Some nodes of the support surfaces will have a negative displacement (displacement in the direction of the TBM-front), when the loading situation with a missing support is analysed. In reality this displacement does not lead to tension forces, so a no-tension support is required. Therefore no-tension springs are applied in z-direction.

To determine the spring stiffness, the following assumptions have been made:

- The last placed ring does not have any support in longitudinal direction from the grout layer. This is because this ring is partly in the TBM and the partly in non-hardened grout. This element acts totally elastic.
- The next rings are in hardened grout and will not deform. This means a rigid support.

The supporting ring will have four bearing pads to the previous placed ring and four bearing pads to the new placed ring. The spring stiffness will be calculated with a linear elastic model of segment with four rigid support surfaces, which represent the contact surfaces of the previously placed ring and four load surfaces, which represent the contact surfaces of the new placed ring.

With a load of 12 mN, the average displacement under the load surfaces is 0.403 mm. The stiffness of the total segment is then:

$$k = \frac{F}{u} = \frac{12.0 * 10^6}{0.403} = 29.7 * 10^6 \text{ N/mm}$$

The support surfaces contain 180 spring elements. With the assumption that the stiffness of the segment is equally distributed over the support surfaces, the stiffness per spring is:

$$k_{spring} = \frac{k_{total}}{n_{springs}} = \frac{29.7 * 10^6}{180} = 165.3 * 10^3 \text{ N/mm}$$

This value is checked by a calculation with imposed displacement. With an imposed displacement of one mm, the total force on the load surfaces is 28.7 mN. This results in a stiffness of $159.3 * 10^3$ N/mm per spring element.

8.2.2 Support of the ring joint in lateral direction

Friction and dowel action will make sure that no displacements in the lateral direction are possible in the ring joint. Rigid supports are applied in this direction.

In fact, the lateral supports should be no-tension springs and these springs should be non-linear too. The spring should be elastic when the ring joint does not slide and should show a sort of plastic behaviour when the lateral forces exceed the friction capacity. The friction capacity of the ring joint depends on the stress in the joint in z-direction. Modelling of the ring joint in such a way costs a lot of time and often leads to convergence problems. Furthermore the influence of the ring joint in lateral direction is expected to be small with respect to the global behaviour of the segment.

Another possibility is to model no rigid supports in lateral direction. A test with a model without lateral supports was done. The numerical stability gives a lot of problems in this model. Assuming that the influence of the lateral support on the global behaviour is small, the choice for rigid lateral supports is reasonable and saves time.

8.2.3 Support of the lateral joint

In the lateral joint, the segment is supported by the adjacent segments of the same ring. This support is approximated by no-tension springs. The spring stiffness used by Tiberti [10] is used in this model. For determination of the spring stiffness, see Paragraph 4.1.1.

9 Simulation of the thrust jack forces in the Barcelona line 9 metro tunnel

9.1 Introduction

The TBM is pushed forward by thrust jacks. These thrust jacks push off on the last placed ring. The thrust jack forces are needed to compensate the friction forces on the shield and the ground and water pressure on the front of the TBM.

In order to determine the stress distribution due to the thrust jack forces, a nonlinear finite element model is made with DIANA. This model is described in Section 4.2.

The load configuration which is used in the Barcelona line 9 metro tunnel is applied on the model of the segment in this chapter. This is a combination of the French and the Japanese thrust jack configuration. There are two pairs of thrust jacks and four support surfaces equally distributed over the segment (Figure 9-1).

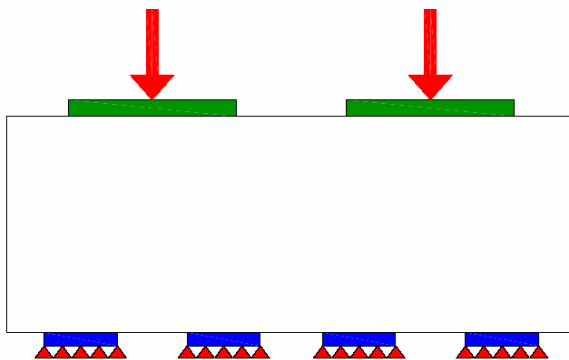


Figure 9-1: Thrust jack configuration of the Barcelona line 9 metro tunnel

The aims of this chapter are to analyse the stress distribution and crack development in the tunnel segment under thrust jack action and to show the reasons for the cracks which have appeared in practice. A description of the occurring cracks in the Barcelona line 9 metro tunnel is given in Chapter 1. These cracks are clarified by different loading situations in this chapter.

In the normal loading situation, the thrust jacks are exactly placed in position and the support of the ring joint is equal. A number of irregularities can occur in practice. As a consequence of irregularities in assembly and the trumpet shape the ring joint may not be smooth anymore and the thrust jacks are not exactly on place. This influences its cracking behaviour. For this reason the following cases are modelled:

- The normal thrust jack loading situation
- Eccentric placement of the thrust jack
- Placement of the thrust jack with an inclination
- Non-smooth support in the ring joint

The simulations are analysed with the help of graphs and crack patterns. These crack patterns are plotted by DIANA and represent the status of the cracks for the selected load step. An example of a crack pattern is presented in Figure 9-2. This crack pattern is built

up of discs. Each disc represents the crack in a certain element and the plain of the disc is the plain of the crack. The different colours (red, green and blue) represent different crack widths, which is visible in the legend on the right.

In this thesis, all crack patterns are plotted with the load side on the top and the ring joint at the bottom side of the image, like in Figure 9-2. Furthermore when is spoken of the spalling zone, the area in Figure 9-2 with the green ellipse is meant, the red ellipsis display the bursting zones and the cracks near the supports are on the bottom of the image. When other cracks occur, they are explained in the relating section.

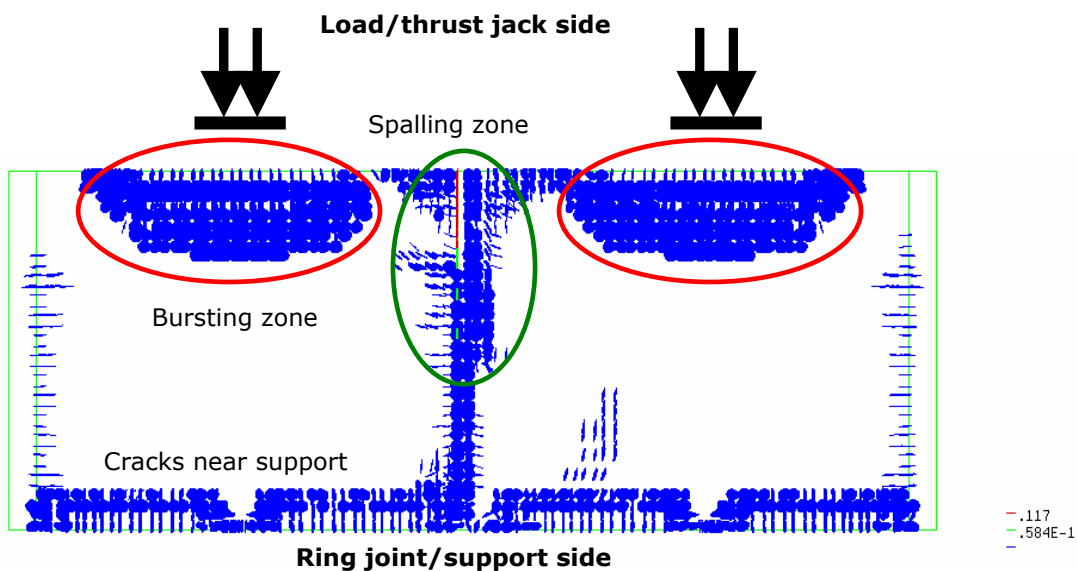


Figure 9-2: Example of the crack patterns which are plotted by DIANA.

The normal loading situation is analysed in detail in Section 9.2. In the sections 9.3, 9.4 and 9.5, the different irregular loading situations are studied by comparing them with the behaviour in the normal loading situation.

9.2 The normal loading situation

In the normal loading situation the thrust jacks are placed in such a way that the stress distribution of the loading surfaces is equal. The support consists of four surfaces of PEBD, which is a easily compressible material. In this calculation it is assumed that the contact from ring to ring is only caused by the PEBD surfaces. The support of the segment subjected by thrust jack forces is therefore restricted by these four surfaces.

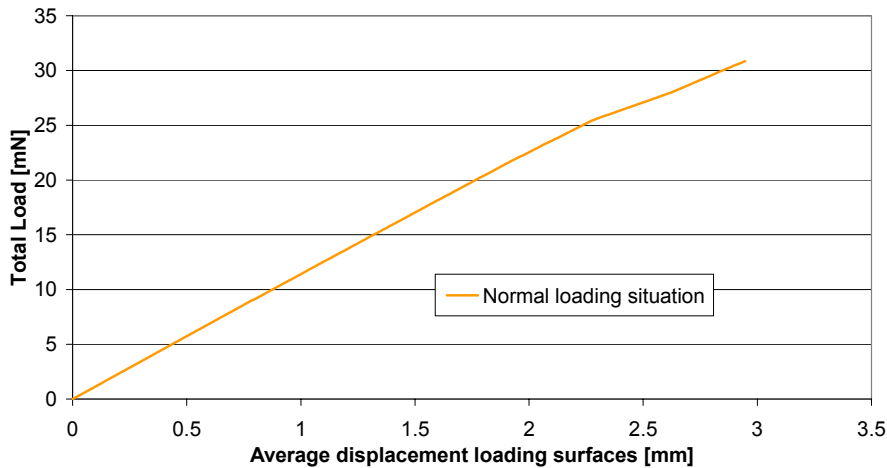


Figure 9-3: Load displacement curve of the normal loading situation

The curve of the total load versus average displacement on the loading surfaces is plotted in Figure 9-3. The segment collapses at a total load of 30.7 mN. The service load is 12.0 kN, so in this situation the safety factor is 2.58. The compressive strength of the concrete is almost reached in z-direction under the loads ($\sigma_{zz}=55.5 \text{ N/mm}^2$, $f'_c=58.0 \text{ N/mm}^2$). On the support surfaces the distribution of stresses in z-direction is unequal due to the eccentricity, which is showed in Figure 9-9.

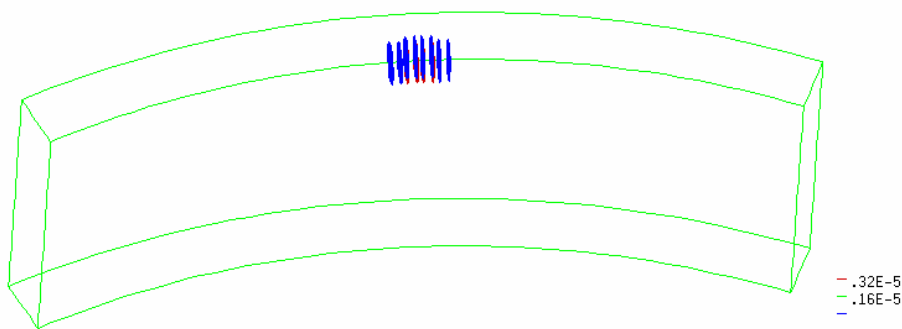


Figure 9-4: First crack due to spalling stresses between the loads

The first crack appears between the loading surfaces (Figure 9-4) at a load of 6.0 mN (0.5 times service load). This is due to the curved shape of the segment on this location (Figure 9-5). The stress situation here is mainly a tensile stress in tangential direction. As the curvature is a sort of imposed deformation, the size of the stresses is dependent on the stiffness of the material. After cracking, the main part of the curvature takes place in the cracks, so the stresses decrease. The spalling cracks develop with an increase of load and penetrate more deeply in the segment (Figure 9-18).

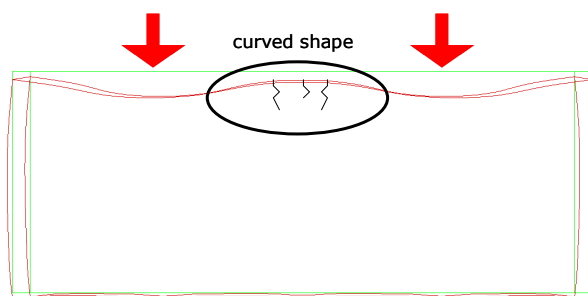


Figure 9-5: Convex shape due to the thrust jack forces

The relative displacement in tangential direction of two nodes in the cracked area is plotted against the total load in order to gain insight in the behaviour of the crack development in this zone.

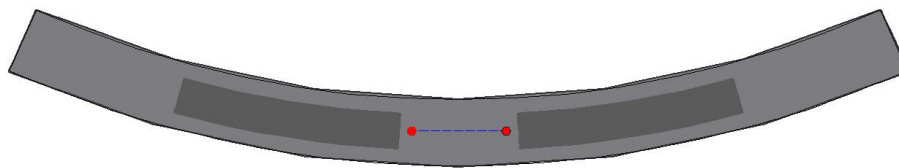


Figure 9-6: Schematisation of the measurement in the spalling zone

This is schematised in Figure 9-6. The two red dots are the nodes in the mesh of which the tangential displacements are subtracted in order to obtain the relative tangential displacement of these nodes. The dark surfaces in Figure 9-6 are the loading surfaces.

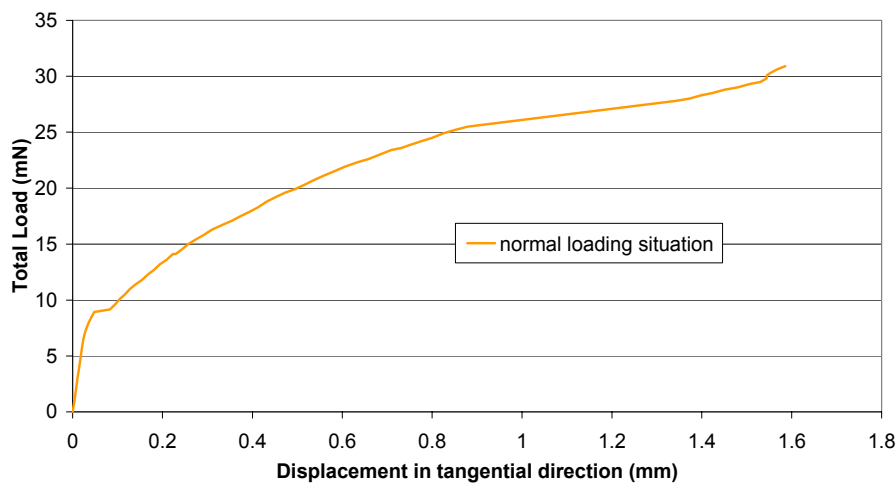


Figure 9-7: Development of the spalling crack between the loads

The graph is plotted in Figure 9-7. It gives an idea of the crack development in this area. The cracks in this region make a change of shape possible. Crack initiation and crack development have a release of stresses as a consequence. Redistribution of stresses is not necessary here, because there is no demand for equilibrium.

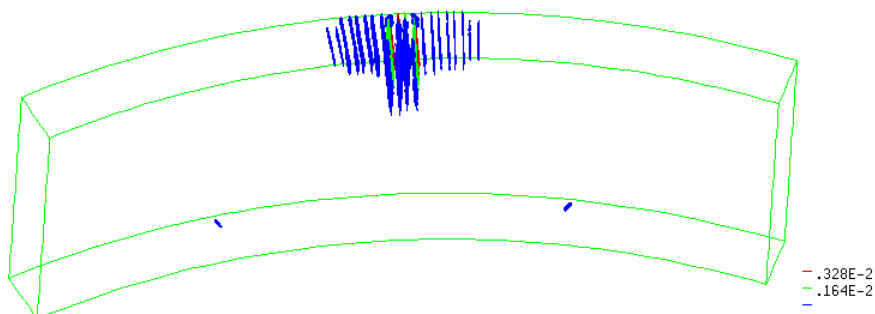


Figure 9-8: Second crack above and between the support surfaces

With an increased load, cracks appear between the support surfaces and above (outside) the support surfaces. These cracks appear at 14.5 mN. The cause of these cracks is the eccentricity of the loads and the supports that is schematised in Figure 9-9. The

eccentricity is approximately 25 mm and therefore the support surfaces are subjected to a higher stress on the outside of the segment.

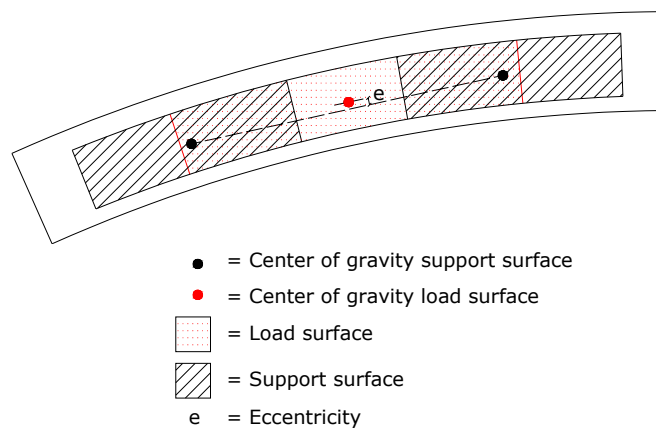


Figure 9-9: Eccentricity of the load and the supports

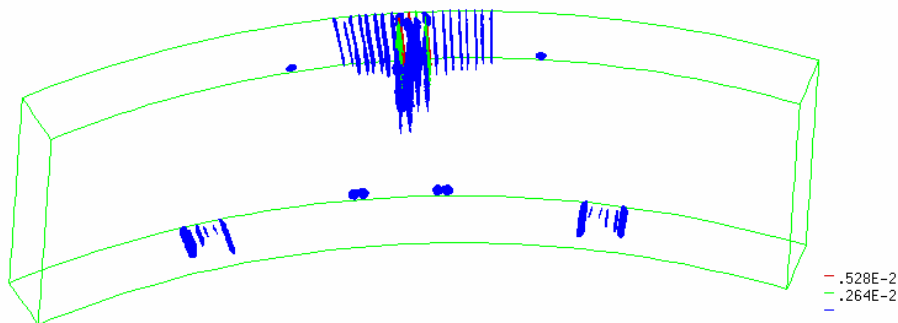


Figure 9-10: Third crack under the load surfaces

The 3rd location of cracks is under the load surfaces, the bursting zone. These cracks appear at 17.5 mN (Figure 9-10) and are caused by splitting forces in radial direction. The cracks in this zone develop in the next load steps. The crack pattern just before collapse is shown in Figure 9-18. At a load of 30.7 mN there are large cracked zones under the load surfaces. The reason for these bursting cracks is the stress distribution in the disturbed zone, which is described in the Literature Survey.

The elastic stress distribution is schematised in Figure 9-11. In the elastic solution, the depth of the disturbed zone is approximately the width of the structure. In the case of bursting stresses in radial direction in the tunnel segment, the width is the lining thickness, which is 350 mm. Therefore the depth of the disturbed zone in the elastic solution is approximately 350 mm.

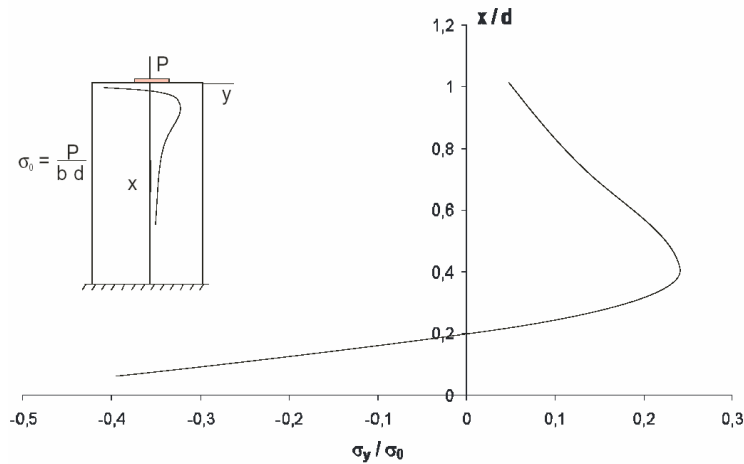


Figure 9-11: Distribution of tensile stresses in a disturbed region (Schnütgen and Erdem, 2001)

The aforementioned elastic solution of the disturbed zone is no longer applicable after cracking. The splitting stresses decrease in the cracked zone and are redistributed over a larger area. Due to the toughness of the material, the disturbed zone is larger than in the elastic solution. This is visible in Figure 9-18 in the picture of the top-view of the segment. The zone in which bursting cracks are present is approximately 600 mm, which is 170% of the disturbed zone in the elastic solution.

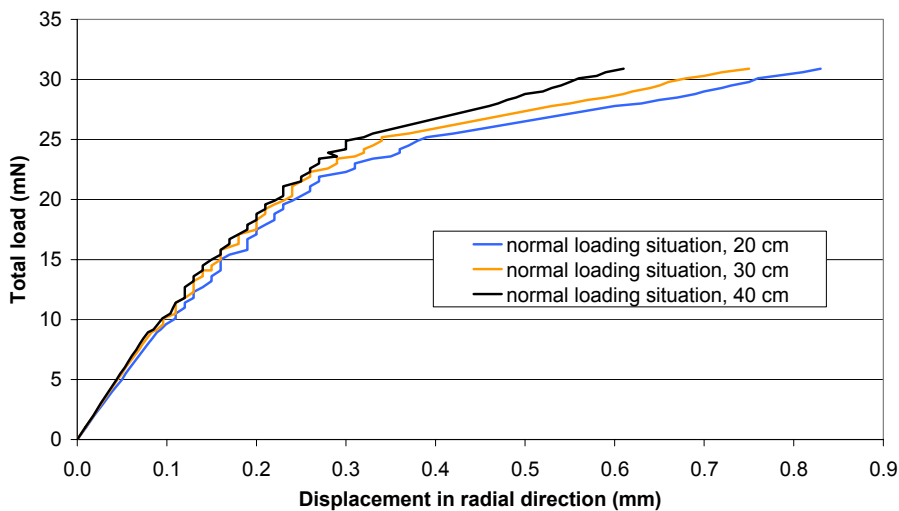


Figure 9-12: Development of the bursting crack under the load

In Figure 9-12 a graph is given of the development of the crack width opening in the bursting zone under the load. The graph represents the relative displacements of two nodes, of which one is located on the inside of the segment and one on the outside of the segment. Three pairs of nodes are taken on 20, 30 and 40 cm in z-direction from the TBM side of the segment. From the graph can be concluded that there exists a redistribution of stresses after cracking.

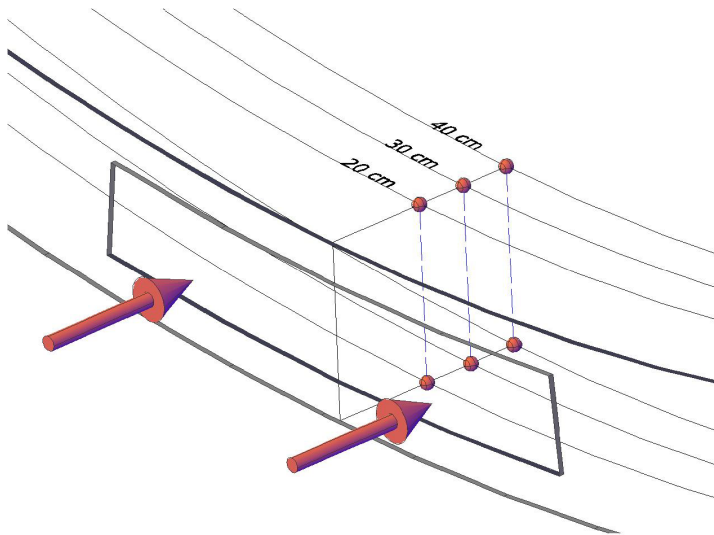


Figure 9-13: Schematisation of the measurement of the bursting cracks

This is schematised in Figure 9-13. The two red arrows are one pair of thrust jacks. The three pairs of red spheres are the pairs of nodes from which the displacement is measured. The displacement is measured in radial direction. The displacements are subtracted within one pair, in order to obtain the relative displacements.

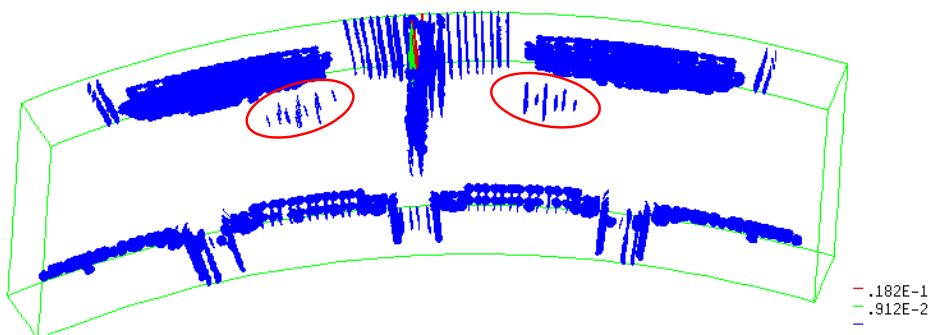


Figure 9-14: Fourth crack in the centre of the segment

At a load of approximately 25 mN, cracks appear on another location (see Figure 9-14). These cracks develop in the following load steps, which is visible in Figure 9-18.

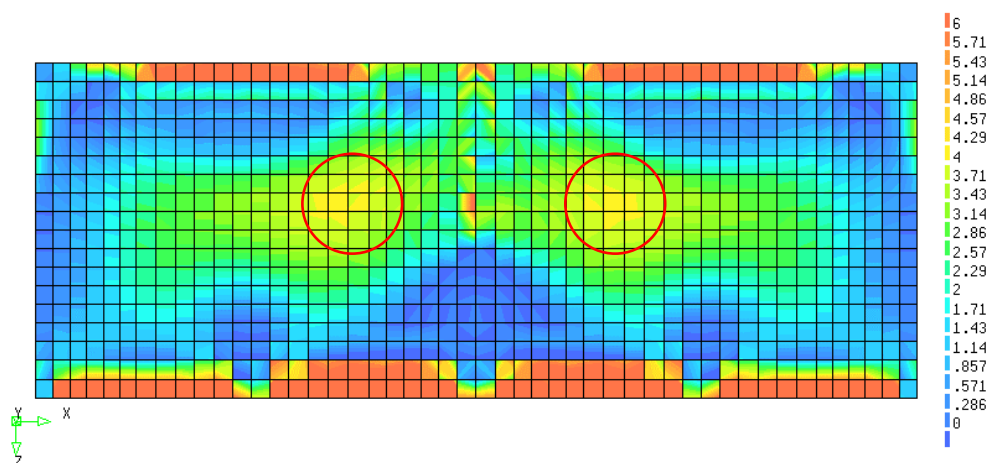


Figure 9-15: Contour plot of the largest principal stresses on the external side of the segment at a total load of 24.5 mN

The cracks initiate on the external side of the segment, on the centre-side of the loads. The cracks appear here, because the magnitude of the stress is increased here due to the convex deformation between the loads. With a contour plot of the principle stresses (Figure 9-15), just before the cracks in this region appear, is shown that there is a high stress on the location where the cracks initiate. With a vector plot (Figure 9-16) the directions of the principle stresses are shown. The cracks initiate perpendicular to these principal stresses.

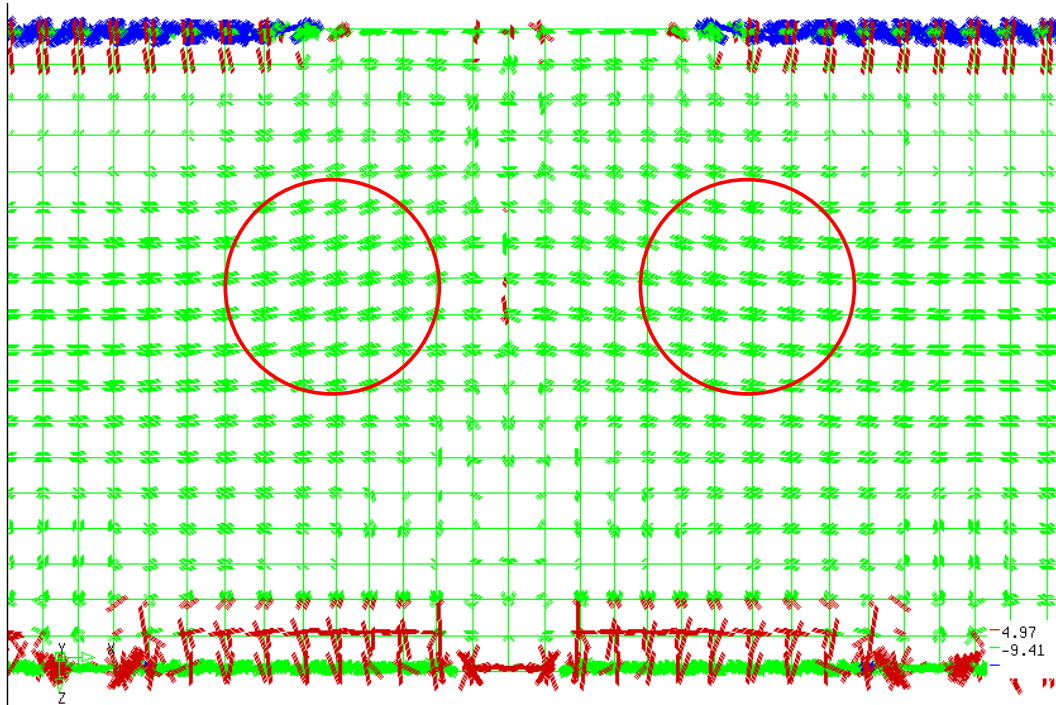


Figure 9-16: Vector plot of the largest principal stresses on the external side of the segment at a load of 24.5 mN

The cracks initiate and develop fast. With a load of 2.52 mN the cracks have been developed until the support side of the segment and the stresses are decreased. In Figure 9-17 this decrease of stresses on a load level of 2.52 mN is visible.

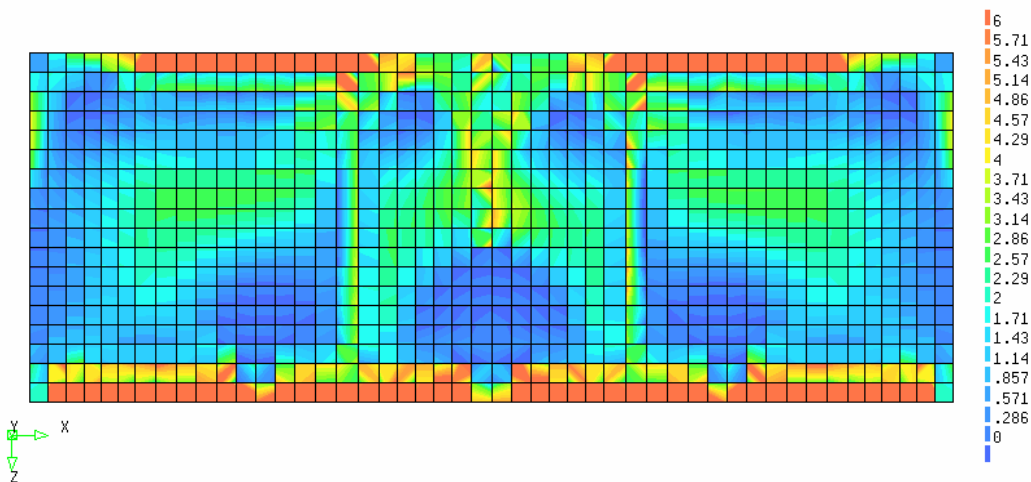


Figure 9-17: Contour plot of the largest principal stresses on the outside of the segment with a load of 25.2 mN

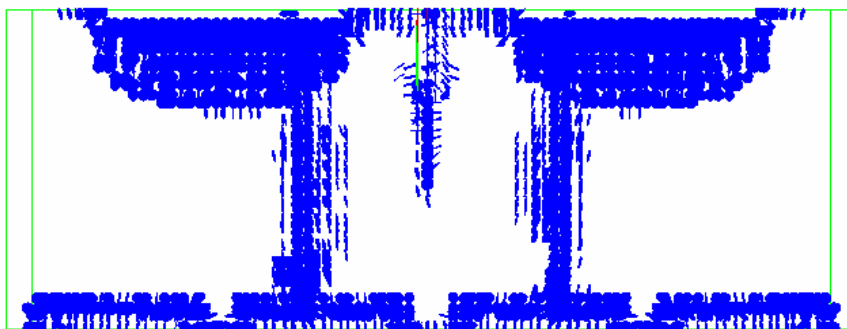


Figure 9-18: Crack pattern at ultimate load 30.7 mN

The ultimate load is 30.7 mN. The model shows a maximum crack strain of 0.0536 in the spalling zone between the loads. The characteristic element size is 83 mm, so with the assumption that there is only one crack in an element, the crack width is 4.45 mm.

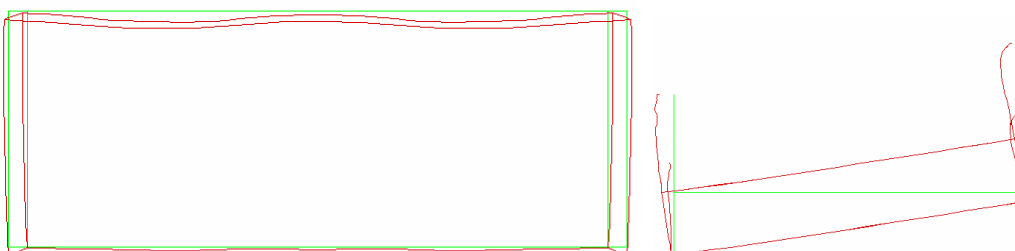


Figure 9-19: Deformed shape of the segment at ultimate load top view (left) and side view

The deformed shape is presented in Figure 9-19. The earlier mentioned curved shape at the thrust jack side is visible in the left figure. The segment tilts outwards due to the eccentricity of the loads with respect to the supports, which is visible in the right figure.

9.3 Eccentricity of the thrust jack

Due to deformation of the tunnel lining and the TBM or due to inaccurate placement, the thrust jacks may not act in the centre of the segment. This introduces a bending moment and a compression stress concentration. An error in placement can occur in tangential or radial direction. De Waal [21] has studied the eccentricity of the thrust jack forces. An eccentricity in tangential direction does not have any influence in this study. Therefore, tangential eccentricity is not taken into account in this thesis. Eccentricity in radial direction will increase the spalling stresses and can lead to damage.

The effect on the stress distribution and crack development by eccentricity in radial direction, which is visualised in Figure 9-20, is studied in this section.

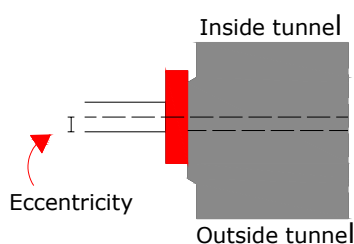


Figure 9-20: Eccentric placement of the thrust jack

The eccentric placement is modelled in DIANA as an unequal distributed pressure on the same loading surface as in the original loading situation. The centre of gravity of the load is eccentric in this way.

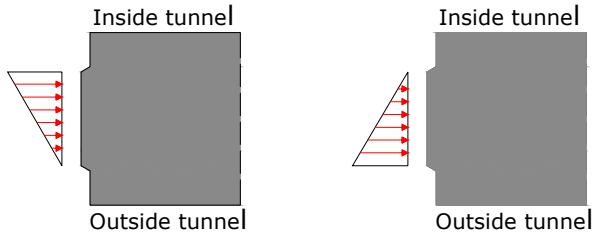


Figure 9-21: Eccentric pressure of the thrust jack inside (left) and outside

For the calculations with eccentricity, a triangular stress distribution on the load surface is assumed (Figure 9-21). This is equal to an eccentricity of 37.3 mm.

9.3.1 Eccentricity outside

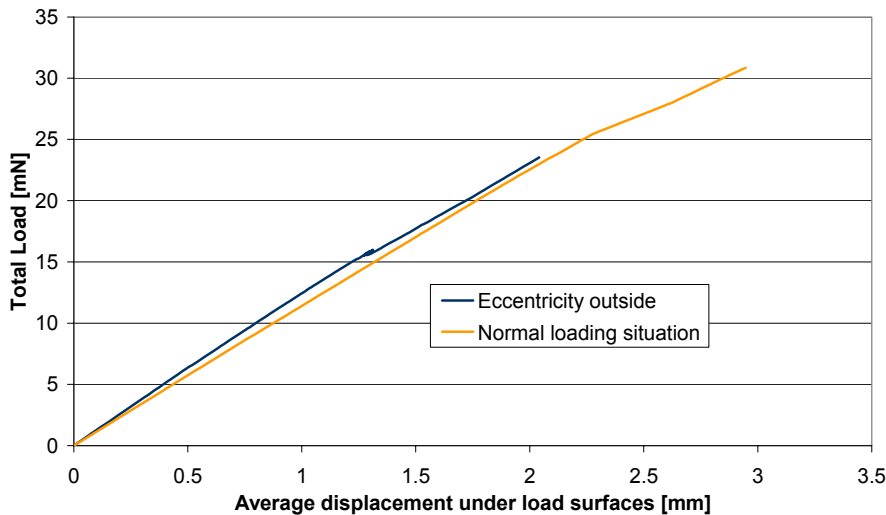


Figure 9-22: Load displacement curves with eccentricity outside and the perfect loading situation

When the above mentioned eccentricity is applied in outside direction (right part of Figure 9-21), a maximum load of 23.6 mN is reached. This means a safety factor of 1.97. Figure 9-22 shows that the ultimate load decreases significantly with respect to the normal loading situation.

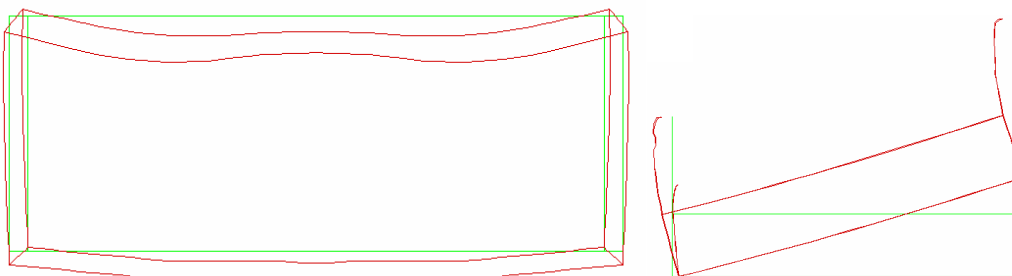


Figure 9-23: Deformed shape of the segment, seen from the top (left) and from the side

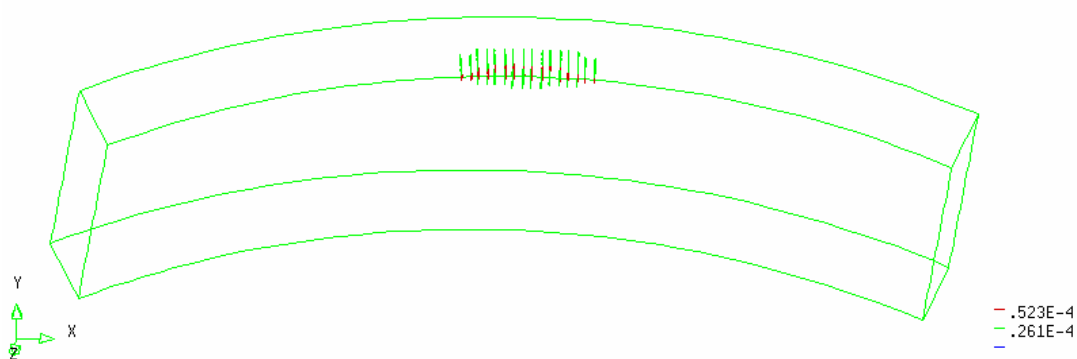


Figure 9-24: First crack due to spalling stresses between the loads

The first cracks that appear are the spalling cracks between the thrust jacks (Figure 9-24). These cracks initiate at 5.0 mN and are dominant for the collapse of the segment in this load case. Due to the eccentricity, the segment tilts outward (right part of Figure 9-23), providing a non-smooth support.

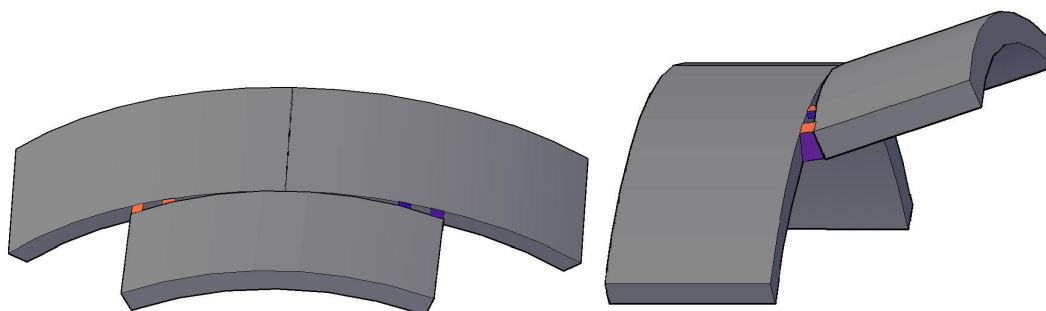


Figure 9-25: First crack due to spalling stresses between the loads

The effect of outward tilting is explained by the 3D model in Figure 9-25. The two adjacent segments are in position and the single segment is tilted outward. Because the segments are curved, there appear gaps between the two adjacent segments and the single segment, at the sides of the single segment. These gaps are at the location of the red/blue surfaces in Figure 9-25. In reality, these gaps do not appear, because the rotational angle is small and the segments are compressed. The result in the simulation is that the springs of the outer supports are less compressed than the springs of the centric supports. This results in a bending moment, which causes tension stresses in the spalling zone between the thrust jacks. In this case, the cracks between the thrust jacks appear by superposition of the tension stresses due to of the bending moment and the tension stresses caused by the curved shape, as explained in Section 9.2.

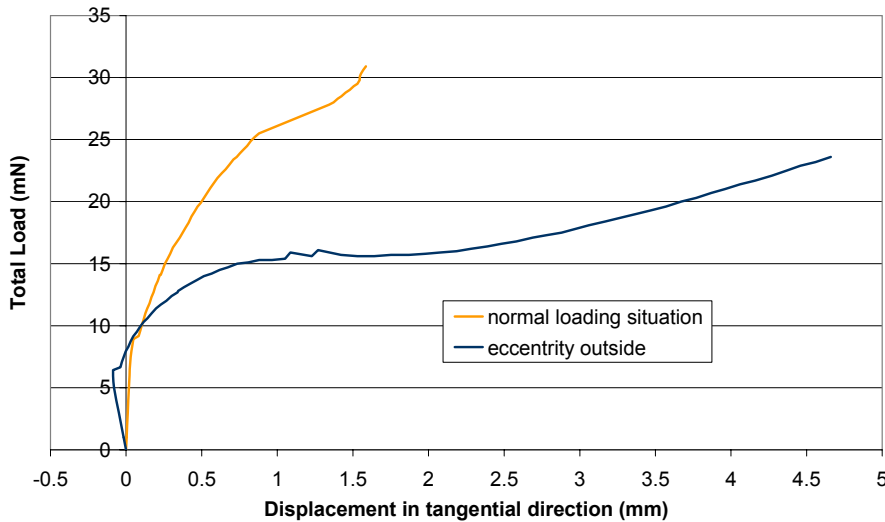


Figure 9-26: Development of the spalling crack between the loads

The relative displacement of two nodes in the spalling zone is plotted against the total load in Figure 9-26. The location of these nodes is schematised in Figure 9-6. From Figure 9-26 it becomes clear that the cracks between the thrust jacks in this loading case are larger in the simulation with an eccentric load. This is because of the earlier mentioned tilting.

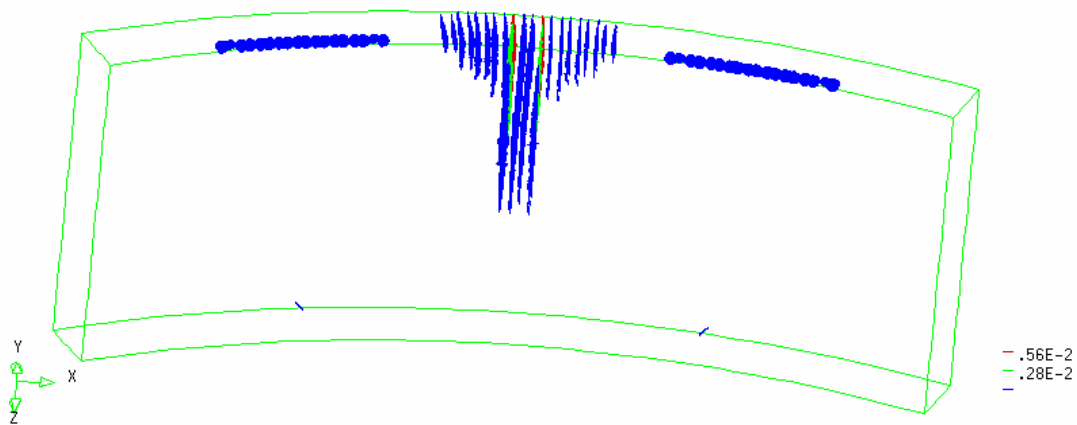


Figure 9-27: Second and third crack due to bursting stresses under the loads and spalling near the supports at 11.4 mN

Cracks initiate in the bursting zone under the loads and spalling cracks initiate near the supports at a load of 11.4 mN (Figure 9-27). The bursting cracks appear on the outside of the segment, because, due to the eccentricity, the thrust jack pressure is higher there. As a consequence of the tilting of the segment, there is an increase of stresses on the outside of the two centric support surfaces. Therefore, the spalling near the supports starts on the outside of the segment.

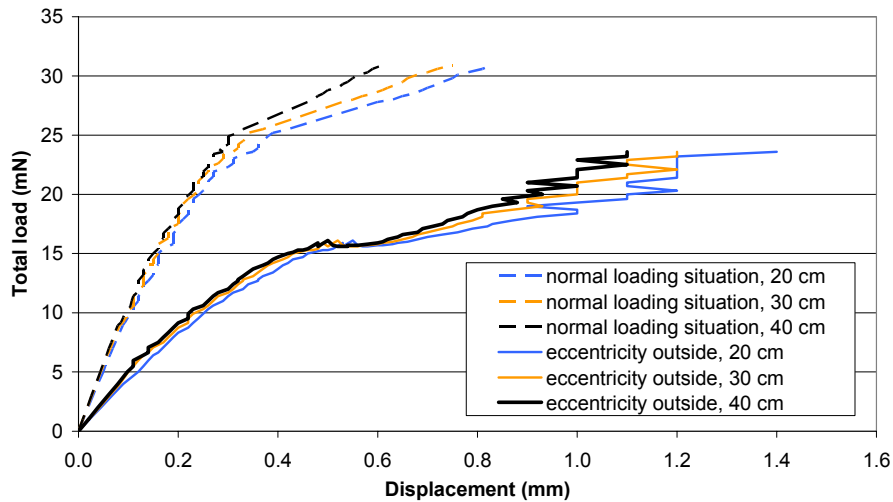


Figure 9-28: Development of the bursting cracks under the load

The bursting stresses initiate at an earlier load level (11.4 mN instead of 17.5 mN in the perfect loading situation). This is because the stresses in longitudinal direction are locally higher. An idea of the cracks in the bursting zone can be obtained from Figure 9-28. The principle of this graph is explained in Figure 9-13.

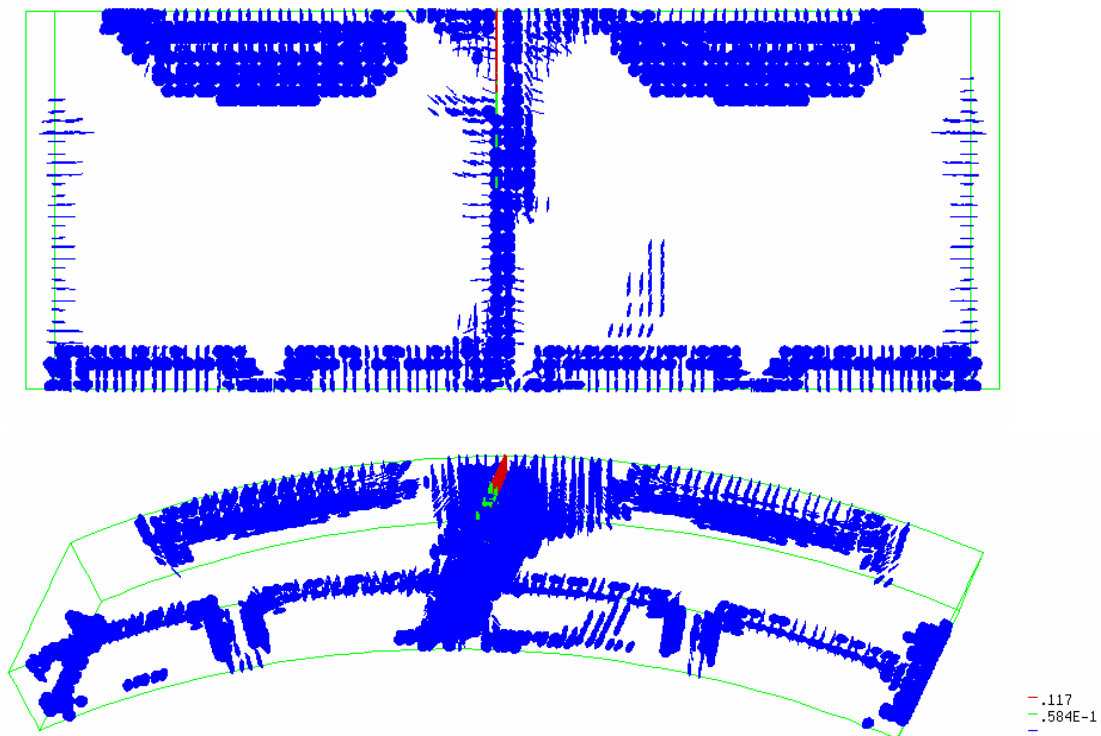


Figure 9-29: Ultimate load at 23.6 mN, top view (up) and 3D view

The crack between the loads caused by the spalling stresses and, as showed in Figure 9-29, the crack develops over the total depth of the segment due to the increasing bending moment. The bending moment becomes larger by the increasing outward tilting.

Deeply penetrating cracks between the thrust jack zones, like is displayed in Figure 9-29, are observed in the Barcelona line 9 metro tunnel. An example of this crack is shown in Figure 9-30.



Figure 9-30: Spalling cracks between the loads, observed in the Barcelona line 9 metro tunnel

The right figure displays the location of the crack on the photo. In this case a load of 9.3 mN (0.78 times service load) has been applied. Similar cracks occur in the DIANA analysis. The crack width at a load of 11.4 mN (Figure 9-27) is 0.70 mm. Looking at the similarities between the analysis in this paragraph and the observed cracks, eccentricity outside can be a reason for the cracks in Figure 9-30.

9.3.2 Eccentricity inside

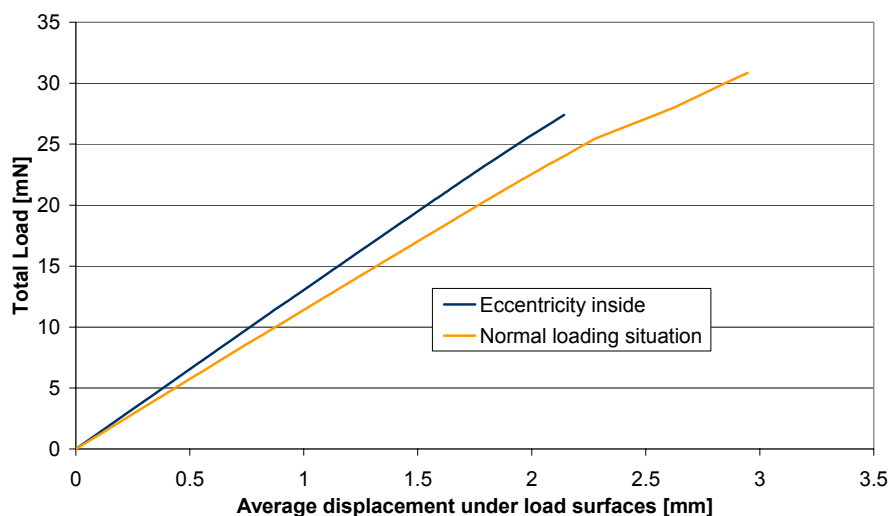


Figure 9-31: Load displacement curves with eccentricity inside and the perfect loading situation

When an eccentricity inside is applied to the load, the simulation stops at a load of approximately 24 mN (Figure 9-31). This means a safety factor of 2.0. Figure 9-31 shows that the ultimate load decreases significantly with respect to the normal loading situation.

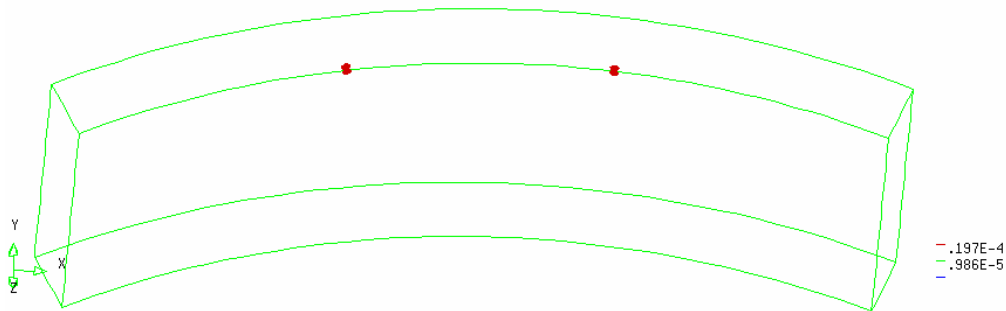


Figure 9-32: First crack due to spalling between the thrust jacks at 11.0 mN

The relatively high pressure value on the inside of the segment causes spalling stresses at the edge on the inside of the segment (Figure 9-32). At a load of 11.0 mN these stresses lead to cracks in this zone.

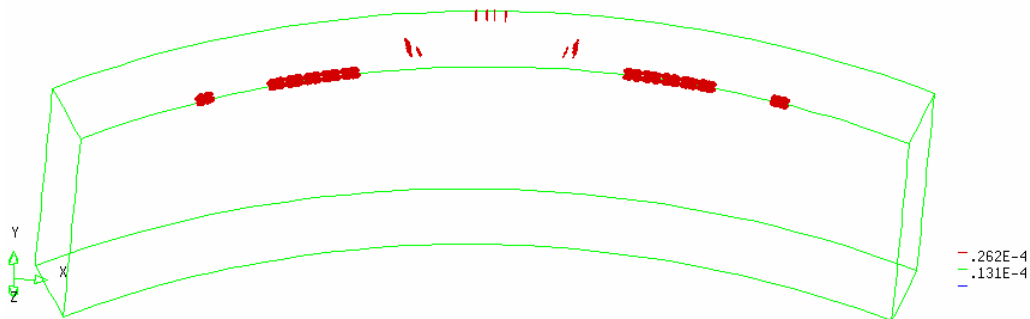


Figure 9-33: Second crack due to bursting under the thrust jack plates 11.5 mN

Just after the spalling cracks at the inside edge of the segment, spalling cracks between the loads initiate (Figure 9-33). These cracks appear later than in the perfect loading situation, because the segment tilts inside. This tilt increases the pressure on the outer supports, which leads to a bending moment with compression stresses in the spalling region between the loads. In this situation, the bending moment due to tilting and the tension stresses due to the curved shape give stresses in opposite directions. Therefore, the tilting has a favourable influence in the spalling zone between the thrust jacks.

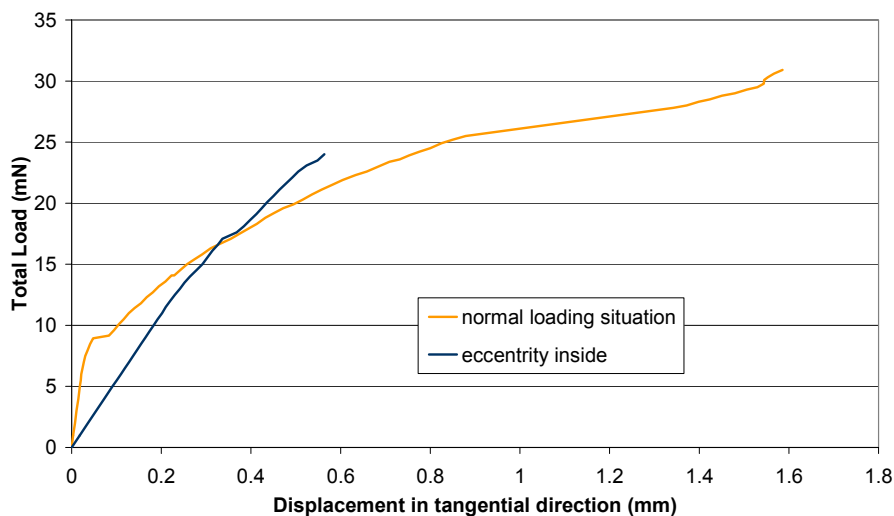


Figure 9-34: Development of the spalling crack between the thrust jack surfaces

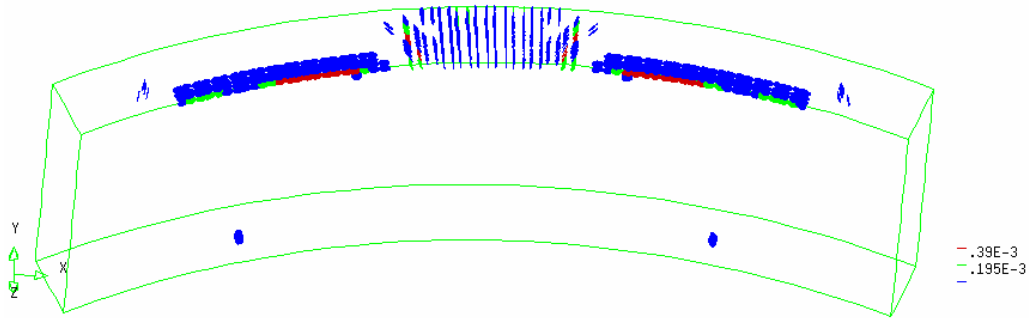


Figure 9-35: Third crack near the support surfaces at 16.6 mN

At a load of 16.6 mN cracks appear near the support surfaces (see Figure 9-35). The cracks appear firstly near the outside support, because the support pressure is higher here due to tilting. At this load level also bursting cracks under the loads have been developed. In Figure 9-35 is visible that the bursting cracks under the thrust jack plates are starting to develop too.

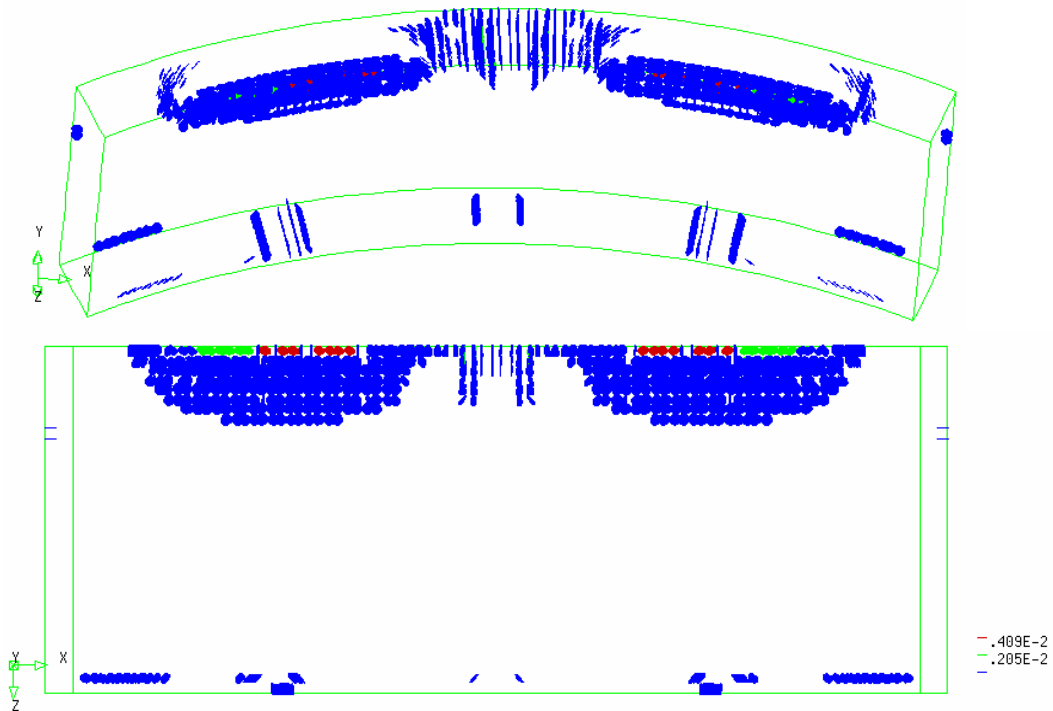


Figure 9-36: Ultimate loading situation at 24 mN, 3D view (top) and top view

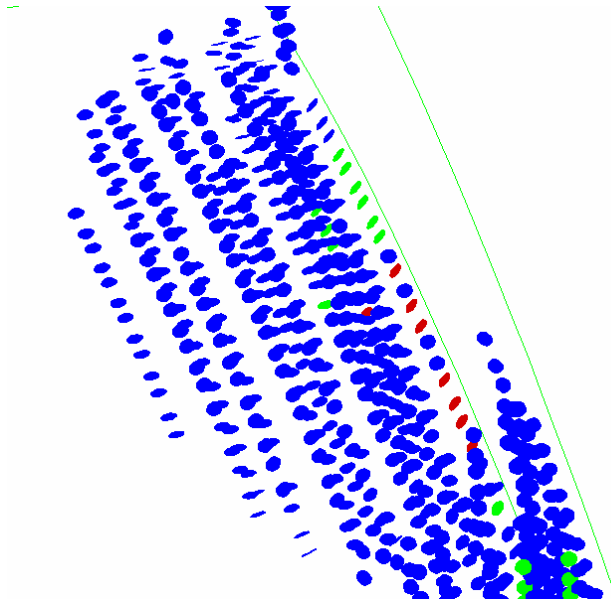


Figure 9-37: Collapse due to spalling cracks on the inside of the segment

At a load of 24 mN the analysis stops due to spalling cracks on the inside edge of the segment.

In the completed part of the Barcelona line 9 metro tunnel, similar cracks are present. These cracks are shown in Figure 9-38.



Figure 9-38: Spalling cracks at the edge, observed in the Barcelona line 9 metro tunnel

The figure in the left photo displays the location of the cracks. The load of the thrust jack was 0.86 times service load (10.3 mN). The crack in Figure 9-38 seems to be larger than in the analysis and the load on which the crack occurs in reality is lower than the ultimate load in the analysis. The reason for this difference may be that the magnitude of the eccentricity is higher in practice or there is a combination of eccentricity and inclination. Furthermore, the mesh refinement may be too coarse to simulate local cracking in a proper way. In Figure 9-39 is clearly visible that the above mentioned spalling cracks occur due to thrust jack action.

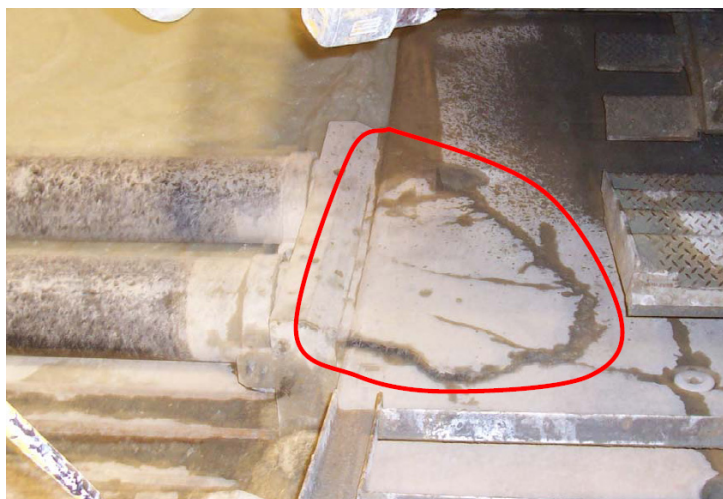


Figure 9-39: Spalling cracks at the edge of the segment, due to thrust jack forces, observed in the Barcelona line 9 metro tunnel

9.4 Inclination between segment and the thrust jack

Due to an inclination of the thrust jack or the segment, the thrust jack force may not be in line with the centre of the segment. It may also happen that the thrust jack is initially in line with the segment, but an inclination appears due to forces that occur later.

The cause of the inclination can be an error in placement. When a ring is placed on an already deformed ring, the new built ring may be deformed before it is loaded by thrust jacks. When the thrust jacks are placed in the right position, they have to be placed under a certain angle. In Figure 9-40 the inclination is illustrated. The angle can be in both directions.

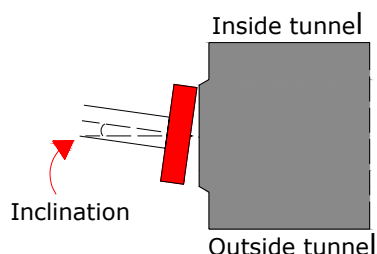


Figure 9-40: Inclination of the thrust jack in outside direction

For determining the load on the model, some assumptions have been done. The length of the thrust jack in the most slide-out position is assumed to be 50 cm and the maximum error in radial direction is assumed to be 2 cm. The inclination is modelled in DIANA as traction in radial direction. This traction is added to the thrust jack force, as shown in Figure 9-41. The size of the traction is

$\frac{2}{50} = 0.04$ times the thrust jack pressure in longitudinal direction. This traction will be added to the longitudinal pressure and will have the size of 0.04 times the longitudinal pressure for every load step.

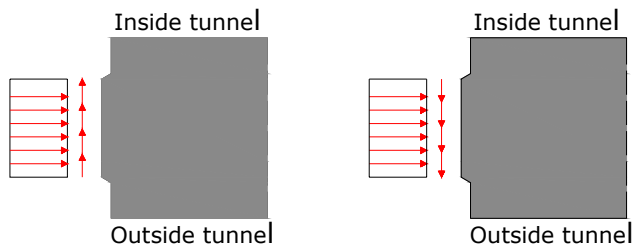


Figure 9-41: Modelling of the loading situation with inclination inside (left) and inclination outside

Analyses with inclination outside and inside are analysed in the following paragraphs.

9.4.1 Inclination outside

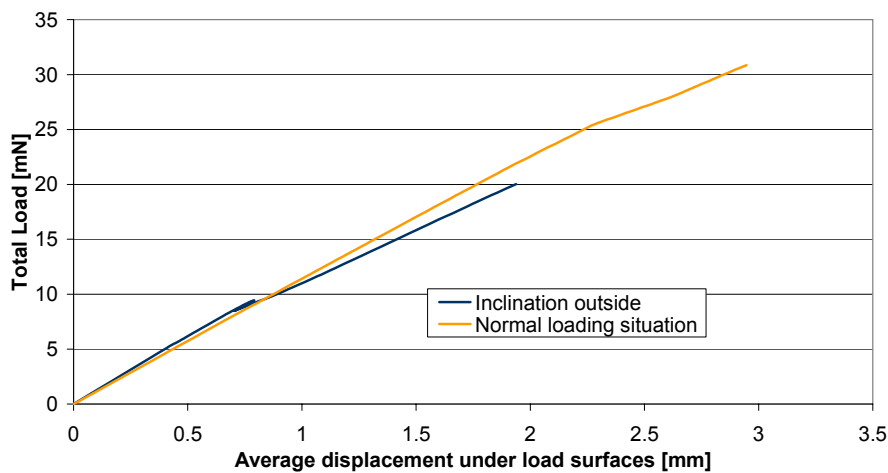


Figure 9-42: Load displacement curves with inclination outside and the perfect loading situation

Figure 9-42 shows an ultimate load of 20 mN, which comes down to a safety factor of 1.67. The simulation with outside inclination results in the same tilting effect as the simulation with eccentricity outside (Paragraph 9.3.1). The difference is that the outside inclination involves a horizontal tension force imposed by the thrust jack plates. This is because the traction forces due to the inclination are in radial direction.

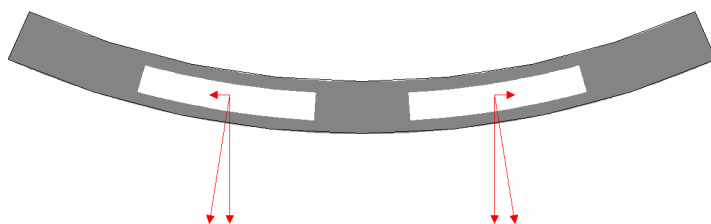


Figure 9-43: Components of the traction due to the inclination outside

Therefore, the traction forces of the two thrust jack plates are not parallel and tension force in the segment must make equilibrium to these forces. This is visible by the small horizontal arrows in Figure 9-43. There is a change of slope visible at approximately 10 mN, which will be clarified below.

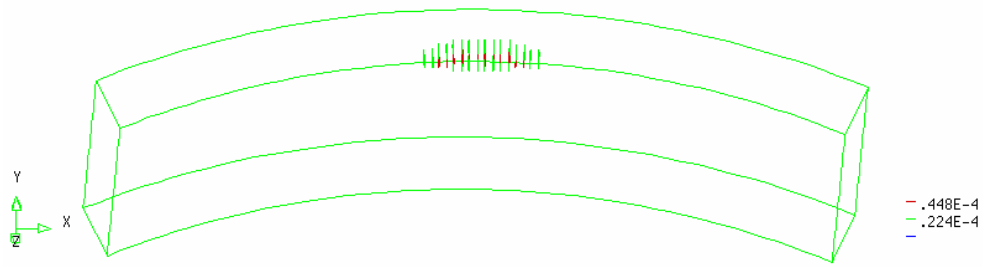


Figure 9-44: First crack in the spalling zone between the loads at 4.0 mN

The simulation shows a similar crack pattern as the simulation with eccentricity outside (Paragraph 9.3.1). Figure 9-44 and Figure 9-45 show a crack pattern which is similar to the crack pattern in this simulation. The difference is that the applied inclination has a larger influence on the behaviour of the segment than the earlier applied eccentricity. This is a matter of choice of the size of the eccentricity and the inclination by the author. What the magnitudes of the eccentricity and inclination in practice are, is not studied here.

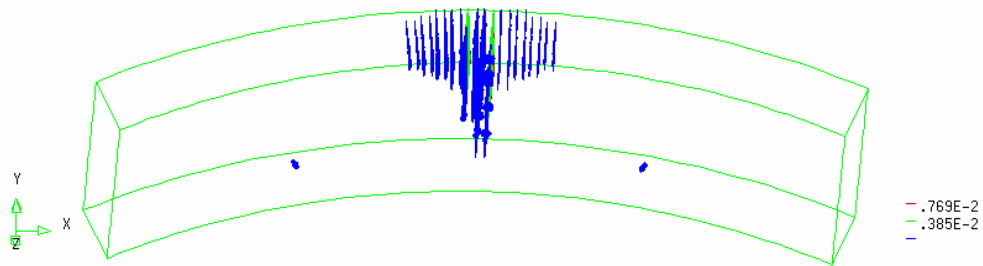


Figure 9-45: Second crack near the support surfaces at 8.45 mN

The spalling crack between the thrust jack plates has developed over the total depth of the segment at a load of 10 mN (Figure 9-46). The segment splits in two parts, which are kept together by the steel fibres. This causes the change of slope in the load displacement curve in Figure 9-42.

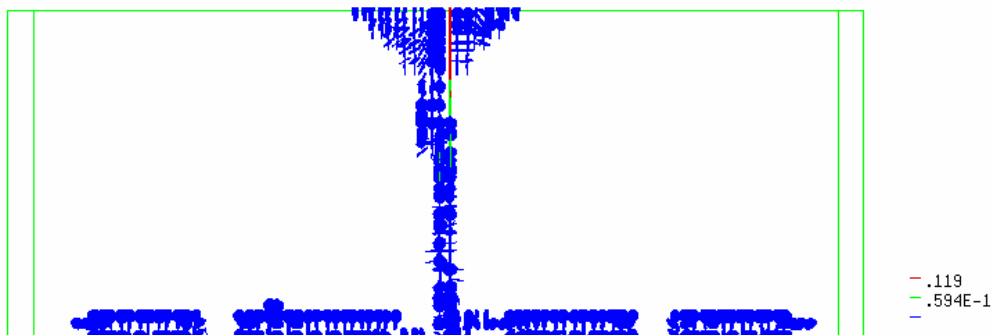


Figure 9-46: Crack pattern at 10 mN, spalling crack over the total depth of the segment

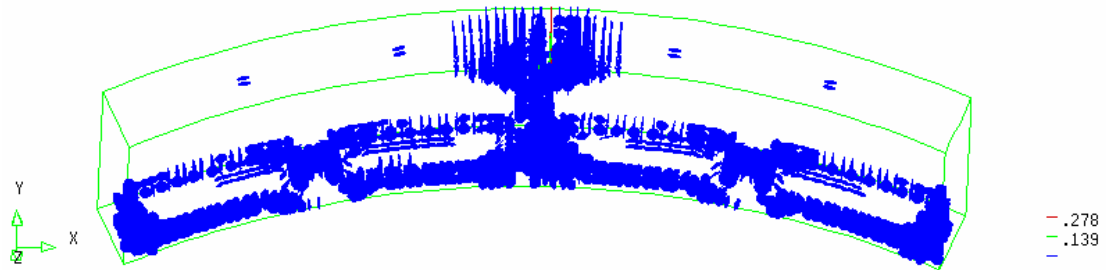


Figure 9-47: Bursting cracks under the loads at 1.92 mN

The bursting stresses under the loading surfaces appear on approximately the same load level as in the perfect loading case. The cracks appear 19.2 mN in this case and at 17.5 mN in the perfect loading case. This is according to expectations, because the pressure in longitudinal direction is equal for these load cases.

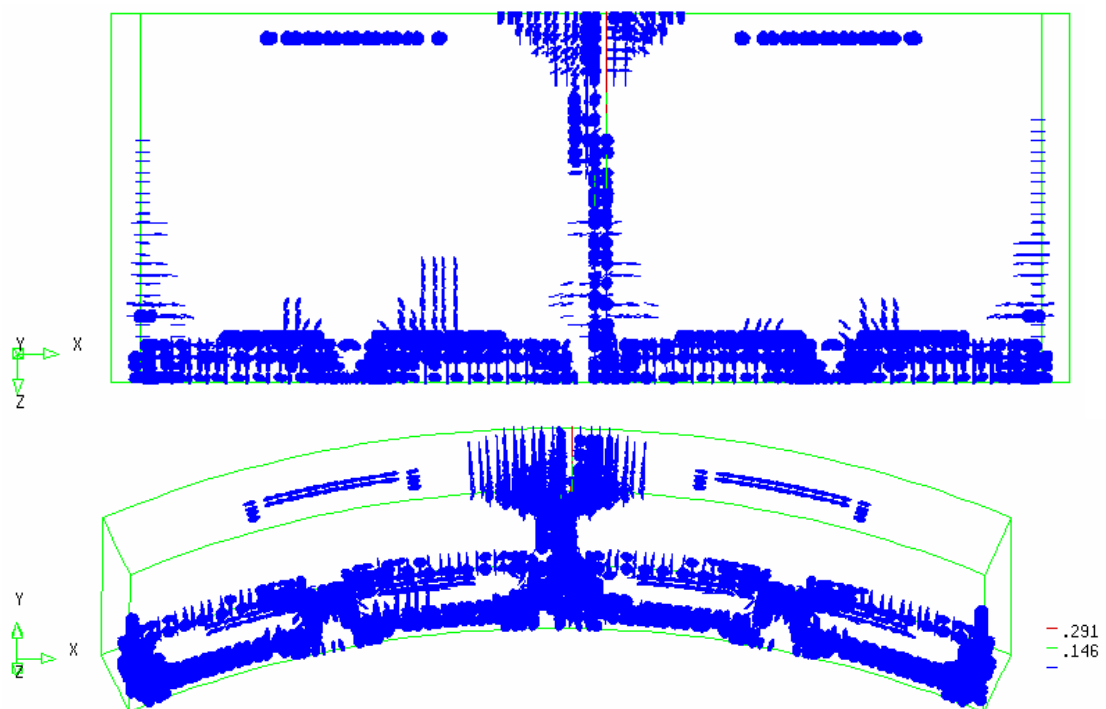


Figure 9-48: Crack pattern at ultimate load: 20 mN, spalling crack over the total depth of the segment

The simulation stops at a load of 20 mN. At this load level the crack between the thrust jacks plates has become very large. In Section 3.2, the assumption that every element has only one crack is done. If the crack strain is now multiplied by the characteristic element length l_c , the crack width is known. For the crack strain in Figure 9-48, this means $0.437 \cdot 83.04 = 36.3$ mm. The length of the applied fibres is 50 mm, so, assuming that the fibre bridges the crack in the middle of the fibre, one half of the fibre is pulled out already at 25 mm. This means that the most cracked element has no strength left.

This mechanism leads to the same cracks as when the thrust jack is placed eccentric outside. The occurring cracks are described in Paragraph 9.3.1.

9.4.2 Inclination inside

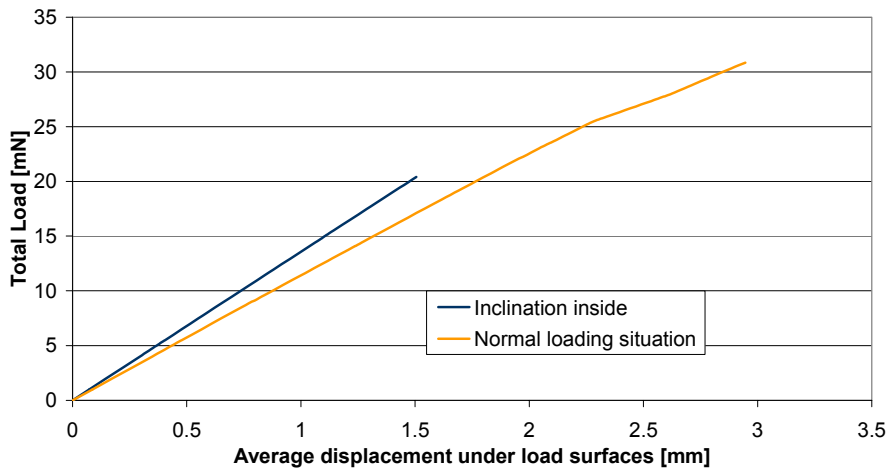


Figure 9-49: Load displacement curves with inclination inside and the perfect loading situation

The ultimate load is 20.4 mN when the thrust is placed inclined inside. This is equal to a safety factor of 1.7.

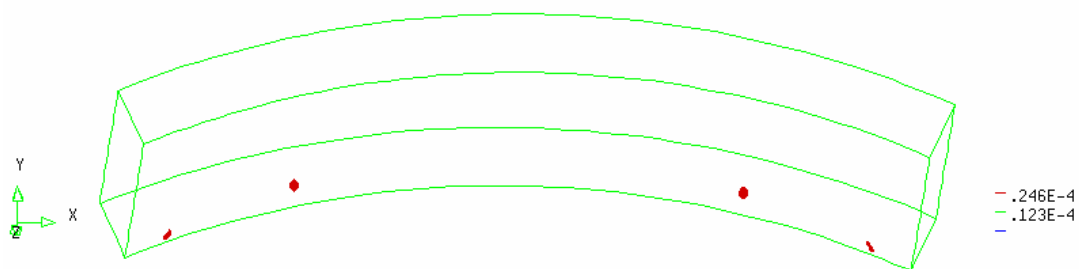


Figure 9-50: First crack near the support surfaces at 13.4 mN

In this load case the segment tilts inwards. The consequence of this tilting is that the outside supports give a higher reaction force than the middle ones. This phenomenon has a bending moment in the plane of the segment as a result. The compression stresses due to this bending moment are at the TBM side of the segment. For this reason spalling cracks between the loads occur later: at 14.4 mN instead of 6.0 mN (normal loading case). The first crack occurs on the location of the more heavily loaded outside support surfaces.



Figure 9-51: Second crack in the spalling zone between the loads at 14.4 mN

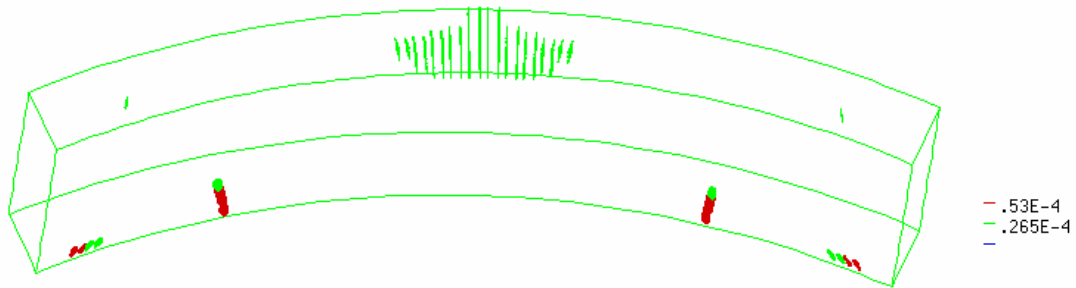


Figure 9-52: Third crack outside the load surfaces at 14.9 mN

At a load of 14.9 mN cracks outside of the loading areas start to develop. The inside inclination causes a bending moment out of the plane of the segment. The equilibrium is caused by the lateral joints, which give an outside reaction. Due to this phenomenon stresses in tangential direction are expected. It will have compression stresses on the outside and tension stresses on the inside of the segment as a consequence. Another phenomenon is the tangential bursting stresses. These stresses do normally not lead to cracks, but a superposition of these two phenomena will lead to high tension stresses on the inside of the segment in tangential direction. These stresses lead to cracks and later on to failure in this load case (see Figure 9-54).

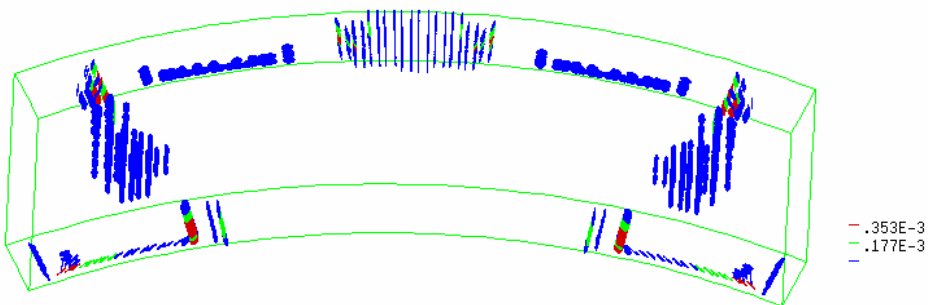


Figure 9-53: Fourth crack in the bursting zone under the loads at 19.4 mN

The bursting cracks under the loads appear on a similar load as in the perfect loading case. This was expected, because the pressure in longitudinal direction is equal to this loading situation.

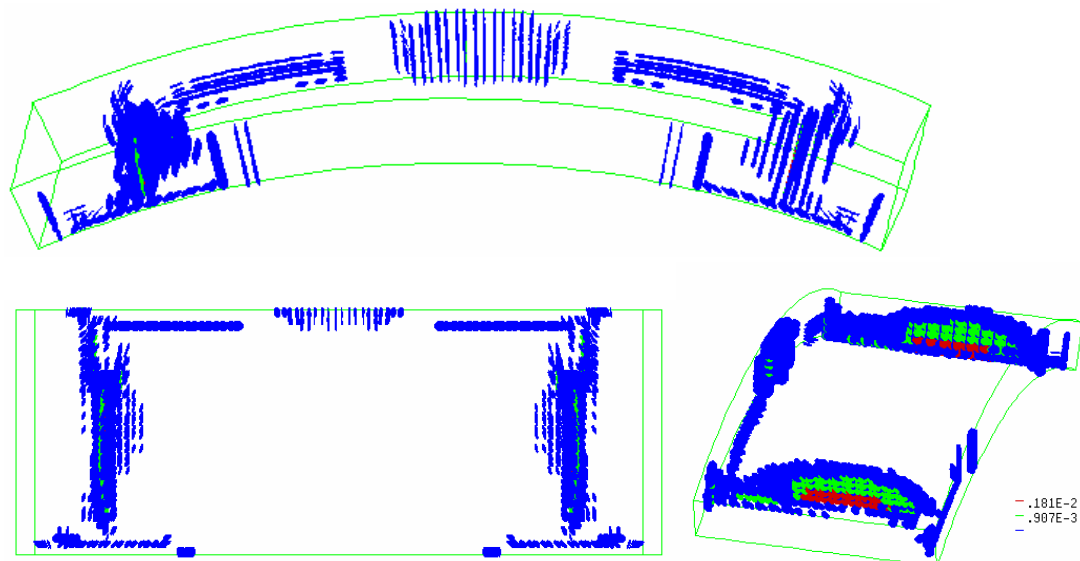


Figure 9-54: Crack pattern at ultimate load, 20.4 mN

The mayor cracks which occur in this mechanism appear at approximately 19 mN. This is over 1.5 times service load. This explains why inclination inside does not cause cracks in practice.

9.5 Non-smooth support of the ring joint

A non-smooth ring joint leads to a non-smooth support of the segments in the next placed ring. This leads to a bending moment in the segment which results in cracking. A non-smooth ring joint can be the consequence of the trumpet shape and/or disturbances during the placement of the segments. Bloemhof [3] studied both cases. The reasons for this phenomenon are errors in placement and deformations caused by the trumpet shape. The gap in the ring supports lead to values of approximately 6 mm in this study. In the next paragraphs the non-smoothness caused by the trumpet shape is simulated in order to study its influence on the stress distribution and crack development in the segments.

The non-smoothness of the ring joint is modelled as a missing support. In practice the support is not missing, but there is a small gap between the last and the last but one placed ring. In the analysis is showed that large cracks occur, even with a small gap, because the displacements in the analyses are small.

9.5.1 Missing support in the middle of the segment

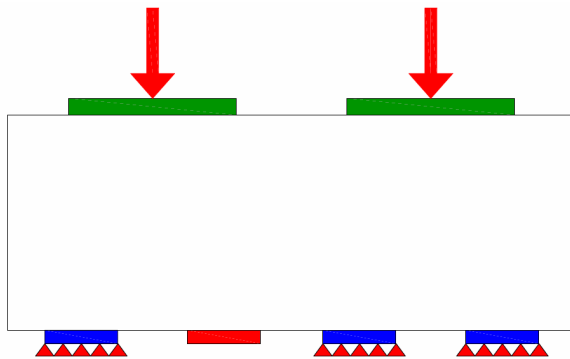


Figure 9-55: Load configuration of the Barcelona line 9metro tunnel with one of the centric supports removed

This paragraph describes the analysis with the load configuration as displayed in Figure 9-55. The red rectangle is the removed support surface.

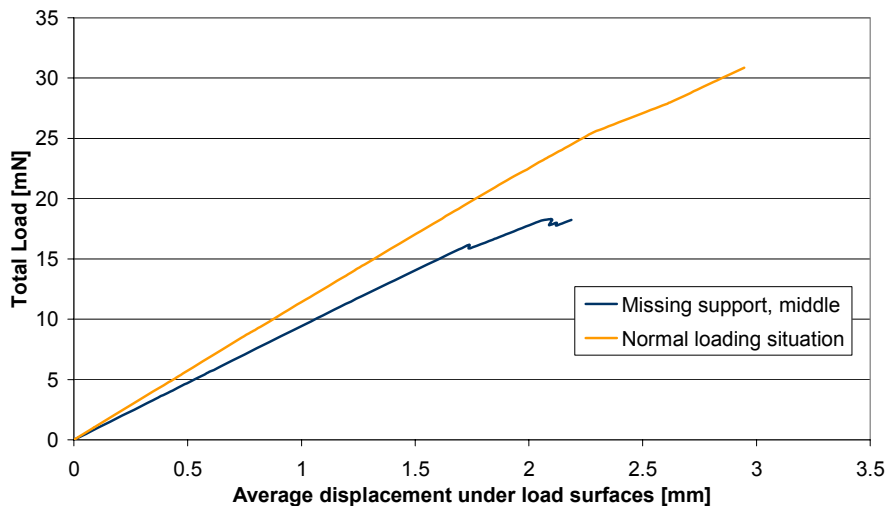


Figure 9-56: Load displacement curves with a missing support in the middle and the perfect loading situation

When one of the middle support surfaces is removed, the bearing capacity of the segment decreases from 30.7 mN to 18.3 mN. The less steep slope, which is visible in Figure 9-56, occurs due to the fact that only three in stead of four compressible surfaces bear the load.

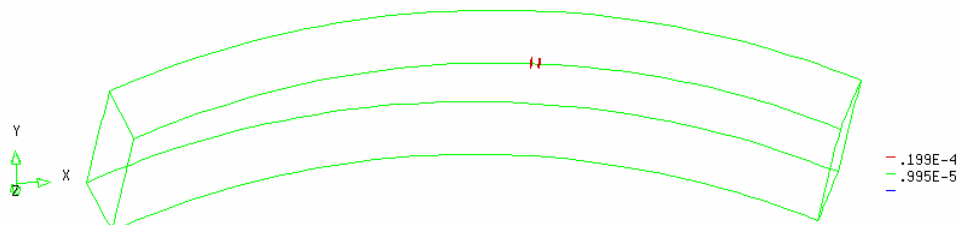


Figure 9-57: First crack in the bursting zone between the loads at 6.58 mN

The first crack appears, as in the other loading situations, between the thrust jack plates. The load on which this occurs is 6.58 mN, which is comparable to the first crack in the normal loading situation.

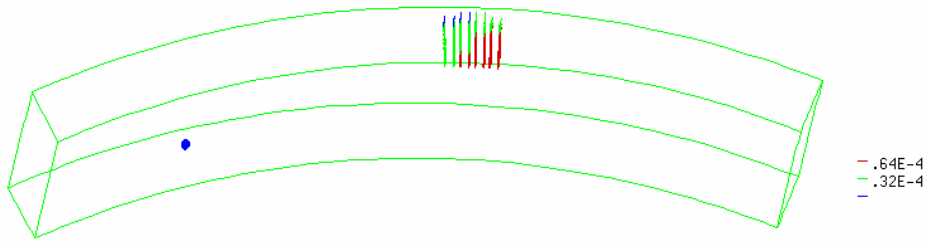


Figure 9-58: Second crack near a support surface at 8.08 mN

The load on the outer support, next to the missing one, is increased due to the missing support. This causes the initiation of cracks at a load of 8.08 mN, which is displayed in Figure 9-58.

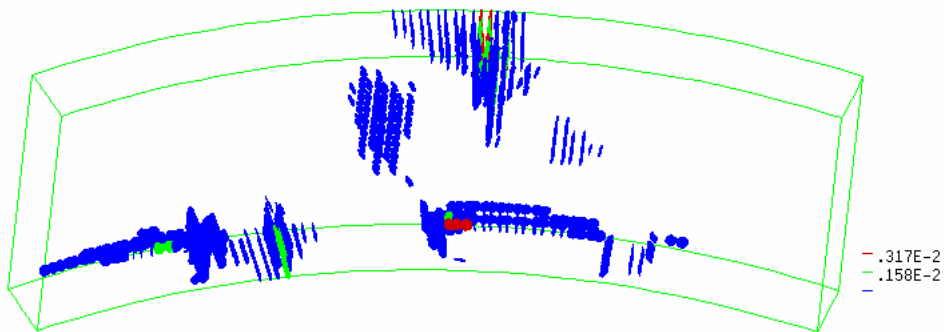


Figure 9-59: Third and fourth crack zone in the centre of the segment at approximately 15.0 mN

The crack pattern at a load of 15.0 mN is displayed in Figure 9-59. Cracks have appeared at the middle support surface, next to the missing support and, more important, cracks are developing in the centre of the segment on two locations. In Figure 9-60 is showed that these cracks develop over the total depth of the segment in the proceeding load steps and lead to failure at a load of 18.3 mN.

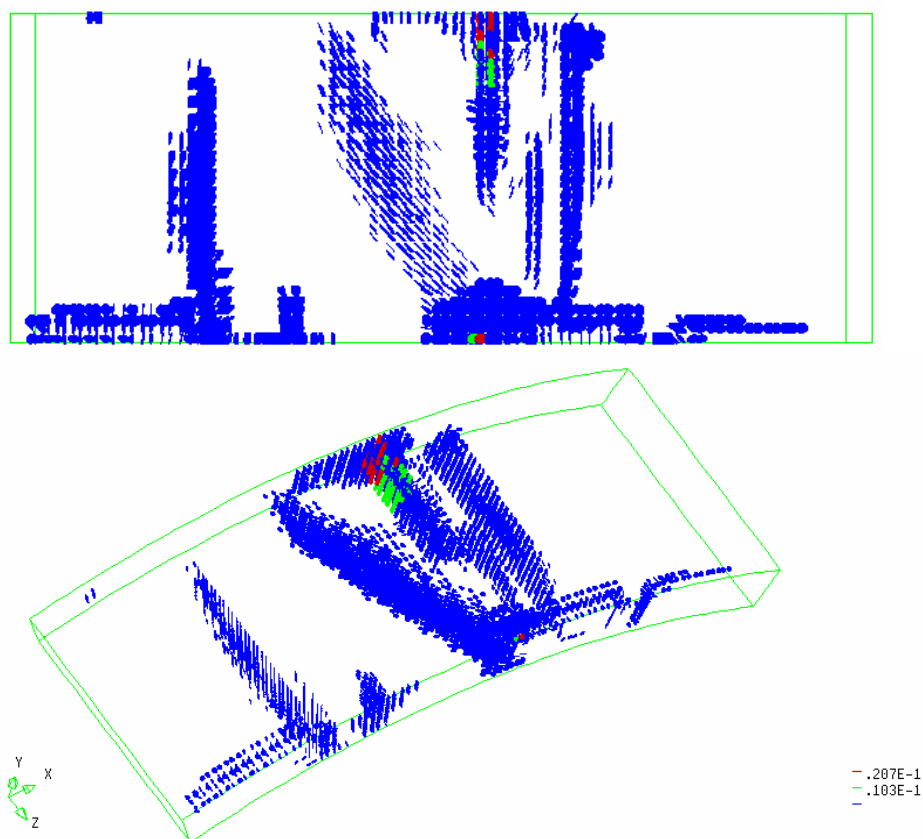


Figure 9-60: Crack pattern at ultimate load, 18.2 mN

In Figure 9-61 is showed that the largest displacement occurs on the position of the missing support.

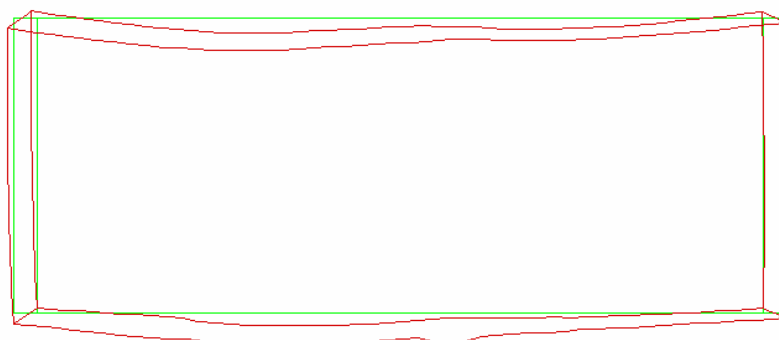


Figure 9-61: Deformed shape of the model with a missing support in the middle

Similar cracks have occurred in the Barcelona line 9 metro tunnel, which is visible in Figure 9-62. These cracks have occurred with a thrust jack load of 5.72 mN of the right thrust jack and 2.23 mN for the left one (8 mN in total).

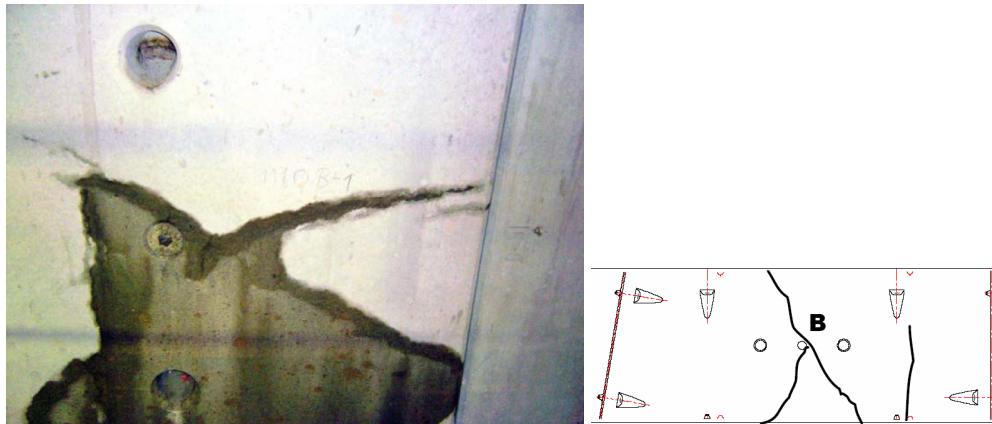


Figure 9-62: Cracks developing from the support side, observed in the Barcelona line 9 metro tunnel

The mayor cracks develop from the support side, but they are not developed deeply into the structure at service load (12.0 mN). Even at 15 mN (Figure 9-58) the cracks are not developed over the structure. Therefore, it is plausible that there are other phenomena that increase the effect of the missing support and cause deeply developing cracks at low load levels. Torsion stresses caused by the trumpet shape could be the reason for these cracks or make them occur on an early load level.

9.5.2 Missing support on the side of the segment

To model the non-smoothness of the ring joint with a gap at the side of the segment, one of the support surfaces is removed from the model. This is showed in Figure 9-63, in which the red rectangle represents the support that is removed.

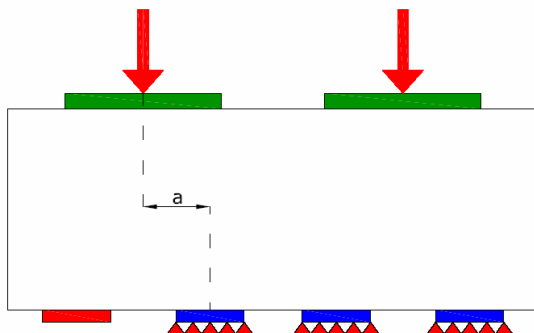


Figure 9-63: Schematisation of the model with a missing support at the side

The displacements in the analysis are small (2 mm), so the in practice occurring gap that is represented by the missing support may not be closed at the end of the analysis.

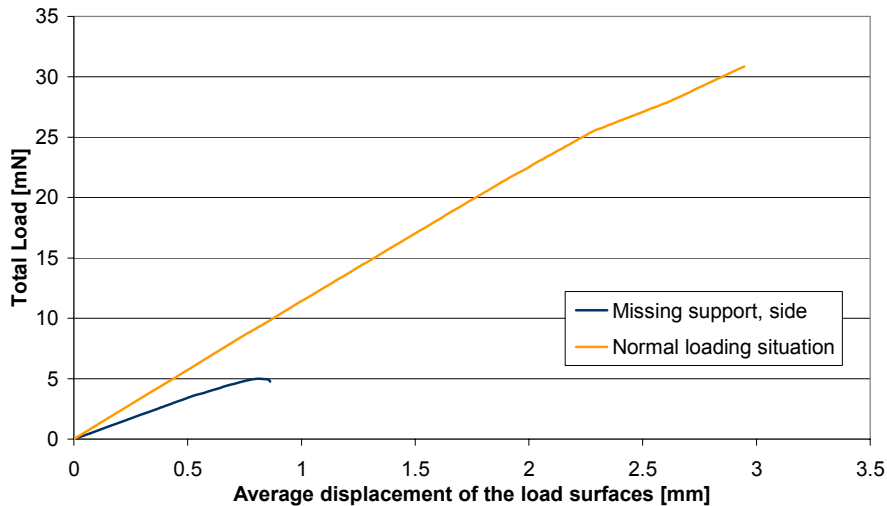


Figure 9-64: Load displacement curves of the analyses with a missing support at the side and the normal loading situation

The missing support at the side of the segment, changes this part into a sort of cantilever beam. This results in a very low bearing capacity, which is visible in Figure 9-64.

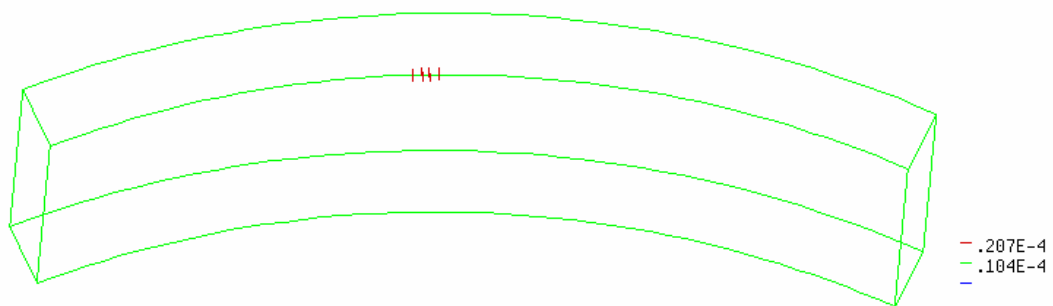


Figure 9-65: First crack due to a bending moment at 2.5 mN

The cracking and collapse of this load case is caused by tangential tension stresses due to an in-plane bending moment. This bending moment is caused by the missing support. The above mentioned cantilever makes the segment crack at a very low load. The crack initiates at 2.5 mN, as showed in Figure 9-65, and develops fast. When the crack becomes longer, the tension surface of the bending moment becomes larger, so the load can increase.

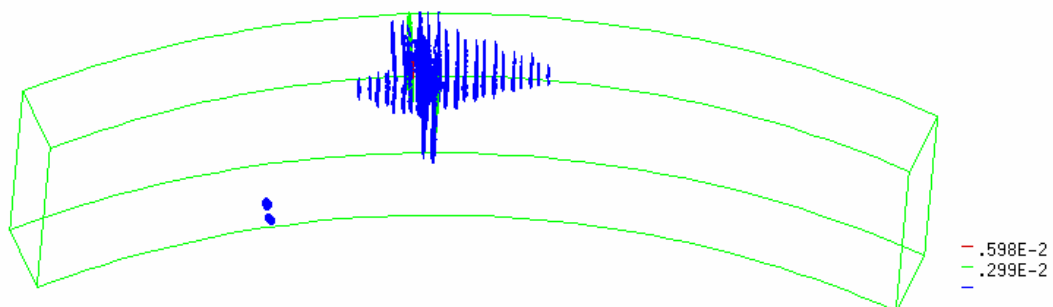


Figure 9-66: Second crack near a support surface at 4.56 mN

At a load of 4.94 mN the crack has been developed over the total depth of the segment (Figure 9-67). No further redistribution of the tension stresses is possible and, as the material shows softening after cracking, no further increase of load is possible here.

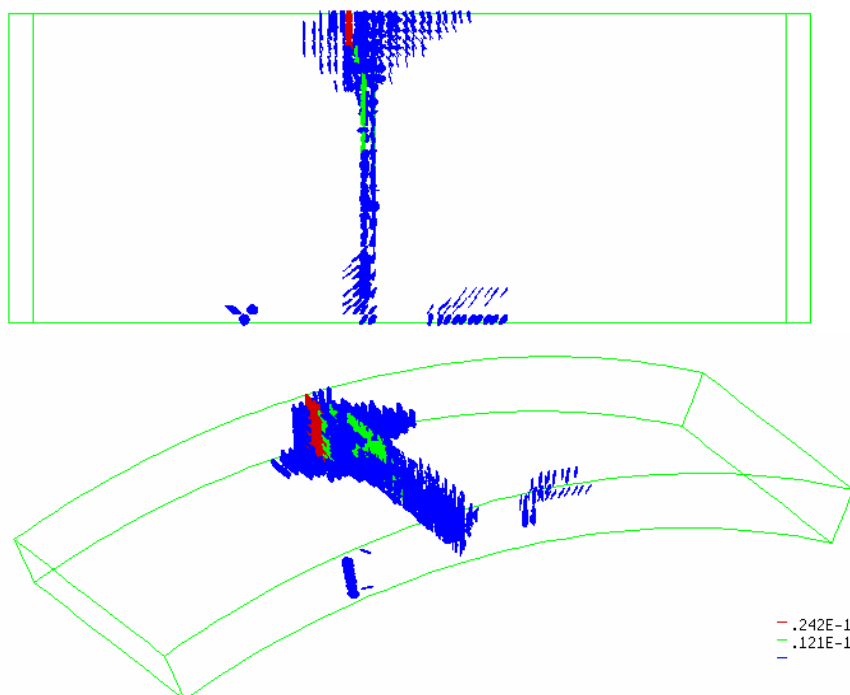


Figure 9-67: Crack pattern at ultimate load, 4.94 mN

The collapse mechanism is clearly visible in Figure 9-68 too. Whereas, the analysis is stopped at 4.94 mN, because the FEM program can not find convergence after this load, in practice the cantilever part deforms until it touches the supporting ring. The crack width is then dependent of the gap in the ring joint support.



Figure 9-68: Deformed shape of the model with a missing support at the side

This mechanism leads to the same cracks as when the thrust jack is placed eccentric outside, with the difference that they appear at a very low load in the analysis with a missing support at the side. The occurring cracks are described in Paragraph 9.3.1.

A rough calculation is made in order to investigate if the occurring bending moment due to the cantilever effect can be carried by reinforcement bars. This calculation is made according to the Dutch code for concrete structures, NEN 6720 [16]. By approximation, the moment arm is the distance from the centre of gravity of the load surface to the centre of gravity of the first support. This comes down to an angle of the 6° of the total tunnel ring. This angle is checked by measuring on Figure 9-67. The distance right from the crack is 37.8% of the total width of the image. The total segment is 48°, so the right

side is 18.2° . The centre of gravity of the load surface is 12° from the right edge, so the angle from the load surface to the crack is $18.2 - 6 = 6.2^\circ$. An angle of 6° is assumed.

Furthermore, the curvature of the segment is not considered. The segment is simplified as a flat plate. The radius to the centre of gravity of the loading surface is approximately 5600 mm, so the moment arm $a = 2 \cdot \sin 3^\circ \cdot 5600 = 586 \text{ mm}$. The height h of the segment is 1800 mm.

According to NEN 6720 article 8.1.4, the cantilever must be considered as a deep beam, the internal moment arm is:

$$z = 0.2(2a) + 0.4 \cdot h = 954 \text{ mm} < 0.8(2a) = 938 \text{ mm}$$

The ultimate moment is:

$$M_u = A_s f_s z = 0.435 \cdot 0.938 \cdot A_s = 0.408 A_s \text{ (kNm)}.$$

The highest load level which occurred in the test is 11.5 mN. When a support is missing at the side of the segment, this comes down to a bending moment of $0.586 \cdot (11.5 \cdot 10^3 / 2) = 3355 \text{ kNm}$.

The required amount of reinforcement steel is then: $A_s = 3355 / 0.408 = 8223 \text{ mm}^2$.

This comes down to 11 bars with a diameter of 32 mm or 7 reinforcement bars with a diameter of 40 mm.

10 Influence of the material properties

The normal loading situation has been simulated with different post-cracking laws, in order to study the influence of the amount of steel fibres. Firstly, different analyses with different amounts of FF1 fibres are done, secondly Ultra High Performance Concrete (UHPC) has been implemented to study if this material is suitable for application in tunnel segments.

10.1 Different amounts of FF1 steel fibres

There is no data available of different amounts of FF1 steel fibres. Therefore, the post cracking properties of the different amounts of steel fibres are derived from the post cracking properties of the earlier used C50/60 with 45 kg/m³ FF1 steel fibres. To do this, the following assumptions have been made, regarding the parameters in Figure 10-1:

- f_{ct} is the concrete tensile strength and is independent of the amount of steel fibres
- s_1 is linearly dependent of the amount of steel fibres. The size of w_1 does not change
- w_c is dependent of the length of the steel fibres

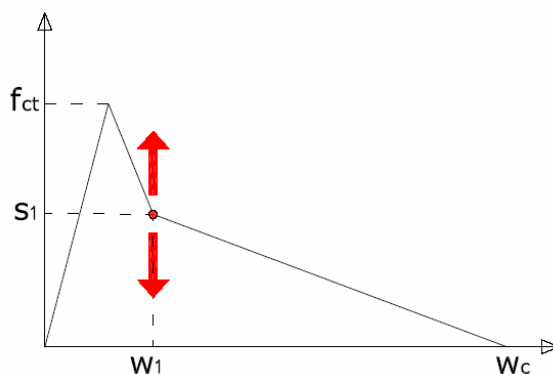


Figure 10-1: Bi-linear tension softening function

From the post cracking behaviour of the C50/60 concrete with 45 kg/m³ we can now determine the post cracking laws of other types of concrete with the formula:

$$s_1 = \frac{X}{45} s_{1(45 \text{ kg/m}^3)}$$

in which X is the amount of steel fibres in kg/m³ for the concrete type that has to be determined. The applied amounts of FF1 steel fibres are 15, 30, 45, 60 and 75 kg/m³. The values for s_1 are given in Table 10-1.

Concrete type	s_1 [MPa]
C50/60, 15 kg/m ³	0.711
C50/60, 30 kg/m ³	1.423
C50/60, 45 kg/m ³	2.134
C50/60, 60 kg/m ³	2.845
C50/60, 75 kg/m ³	3.557

Table 10-1: Values for s_1 for the different amounts of FF1 steel fibres

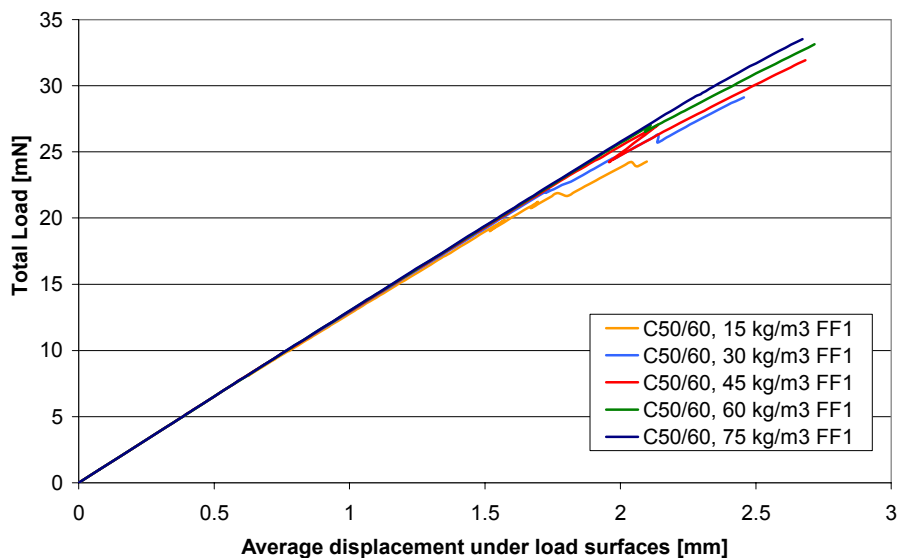


Figure 10-2: Total load vs. average displacement of the loading surfaces for different amounts of FF1 steel fibres

The ultimate load differs from 24.3 mN, when 15 kg/m³ is used, until 33.5 mN when a fibre amount of 75 kg/m³ is used. From the graph in Figure 10-2 it becomes clear that the global behaviour is slightly nonlinear. There must be noted that the analyses of 60 and 75 kg/m³ reach approximately the compressive strength and are probably stopped for this reason.

With the average characteristic element length l_c , the crack-strain calculated by DIANA and the earlier made assumption that every element has one crack, it is possible to calculate the crack-width by multiplying the crack-strain by the average characteristic element length. The values of the crack widths are given in Table 10-2, for every analysed amount of fibres.

Concrete type	Ultimate load [mN]	Maximum crack width at 24.3 mN [mm]
C50/60, 15 kg/m ³	24.3	4.850
C50/60, 30 kg/m ³	29.1	3.155
C50/60, 45 kg/m ³	31.5	2.383
C50/60, 60 kg/m ³	33.1	0.712
C50/60, 75 kg/m ³	33.5	0.280

Table 10-2: Ultimate loads for different materials

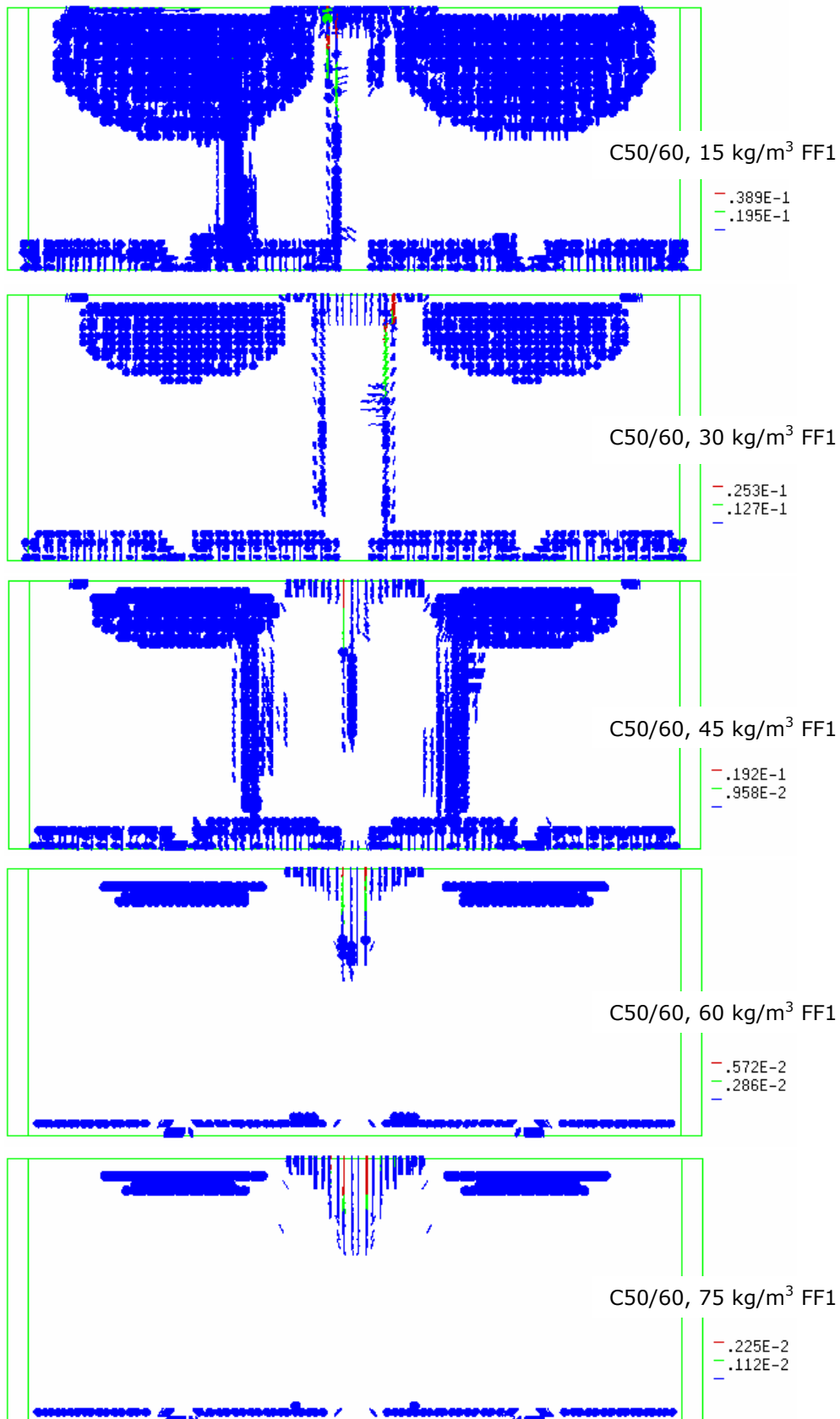


Figure 10-3: Crack patterns at 24.3 mN

The crack patterns of the different amounts of steel fibres at a load of 24.3 mN (the ultimate load for the analysis of the concrete type with 15 kg/m³ steel fibres) are plotted

in Figure 10-3. This figure shows clearly how the amount of steel fibres influences the crack width and crack development.

When the amount of steel fibres is plotted against the ultimate load (Figure 10-4), it becomes clear that, when the amount of steel fibres is increased, the amount of steel fibres has a decreasing influence on the ultimate load. From amounts of approximately 60 kg/m³ it hardly pays putting more steel fibres into the concrete without increasing the concrete compressive strength.

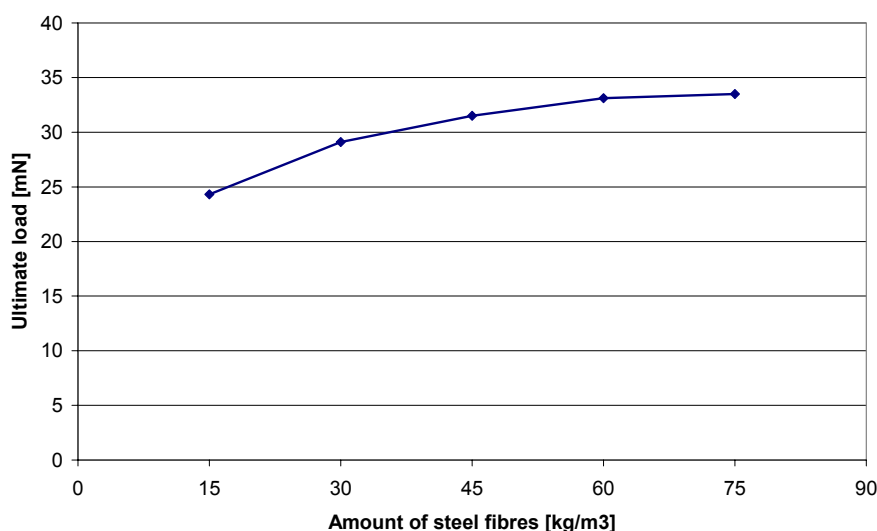


Figure 10-4: Influence of the amount of steel fibres on the ultimate load

Figure 10-5 shows a decreasing influence, in absolute sense, on the crack width with an increasing amount of steel fibres. In relative sense, the influence of the amount of steel fibres has large influences on the crack width, especially when large amounts of steel fibres are applied. Comparing the concrete type with 60 kg/m³ and the type with 75 kg/m³, 25% extra steel fibres gives a maximum crack width which is a factor 2.5 smaller. The point of 45 kg/m³ in Figure 10-5 seems irregular. This is because the spalling zone, where the widest cracks occur, shows two mayor cracks in the analyses with 60 and 75 kg/m³ and one mayor crack in the analysis with 15, 30 and 45 kg/m³. The mayor spalling cracks are the red lines in Figure 10-3.

The influence of the amount of steel fibres on the global development on the spalling cracks between the thrust jack plates is visualised in Figure 10-6. Even though a large influence of the amount of steel fibres is visible in this figure, it becomes clear that there is a significant non-linear deformation for all tested amounts of steel fibres. This confirms that the cracks in this zone occur due to a change of shape. Looking at that crack patterns in Figure 10-3, the influence on this zone is clearly visible.

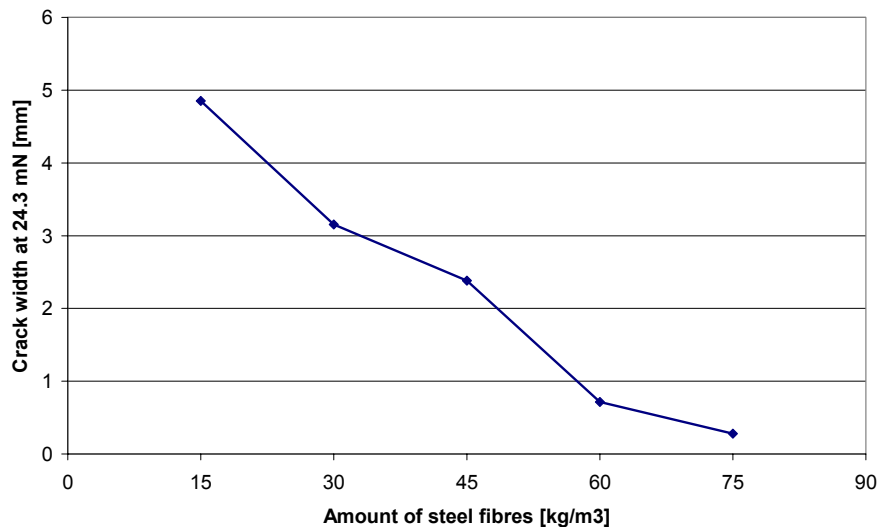


Figure 10-5: Influence of the amount of steel fibres on the crack width

When higher amounts of steel fibres are applied, the crack penetrates less deeply into the segment and the redistribution is better. This is clearly visible in the crack pattern of the concrete type with 75 kg/m³ steel fibres. This figure does not display a long single crack penetrating deeply into the structure, but several short cracks.

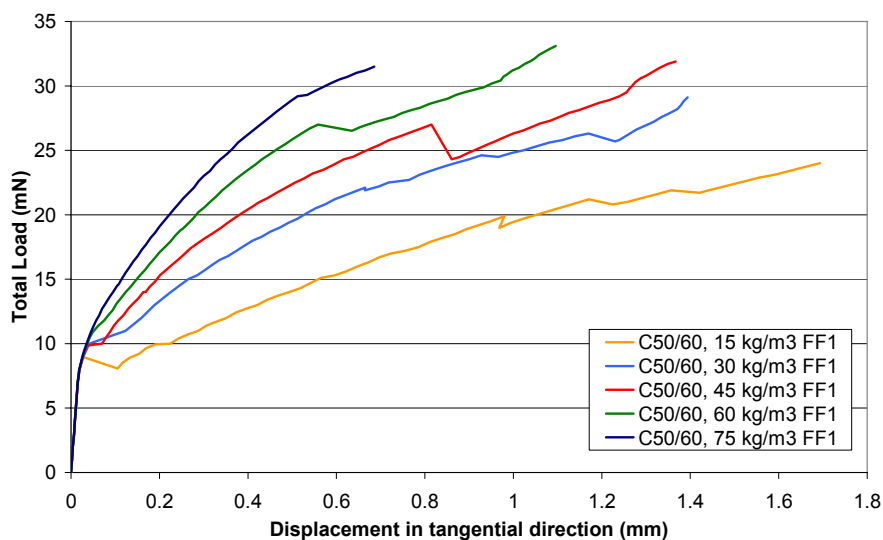


Figure 10-6: Influence of the amount of steel fibres on the spalling cracks

The bursting cracks for different fibre contents can be studied from Figure 10-7. The first 8 mN of the curves are similar. This part contains only linear deformation. After the straight part of the curve, large differences are visible. The linear branch is estimated in Figure 10-7 by extrapolating the load and displacement of the analysis with 75 kg/m³ steel fibres at 4 mN (the element is not yet cracked at this load). The distance between the linear branch and the analysis curves is an estimation of the total crack width over the depth of the segment. Where the concrete type with 75 kg/m³ steel fibres hardly bends of from the linear path, the lower fibre contents show large deformations.

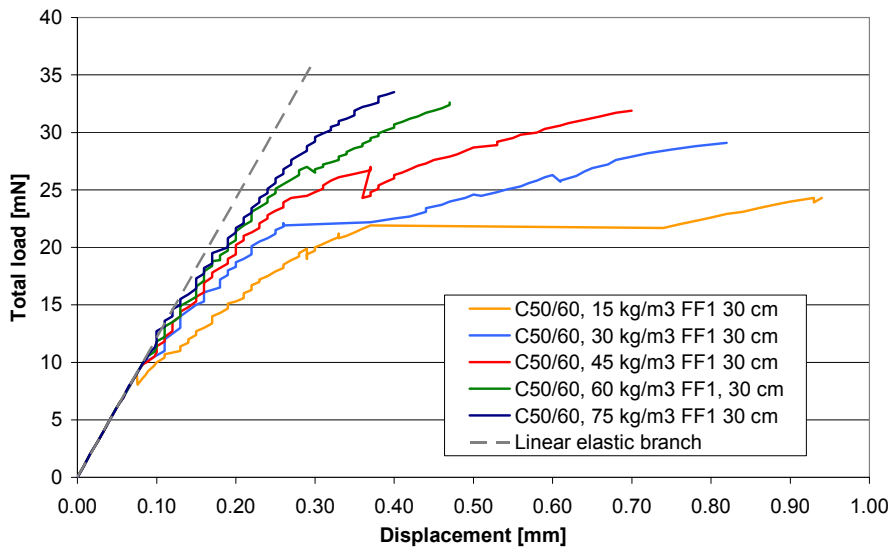


Figure 10-7: Influence of the amount of steel fibres on the bursting cracks

10.2 Ultra high performance concrete

The stress-strain relations of UHPC have been reported by den Hollander in 2006 [13]. These stress-strain relations and the values for the UHPC used in the den Hollander’s report are used to determine the stress-strain relations to implement in the model of the tunnel segment.

The stress-strain diagram for UHPC is given in Figure 10-8.

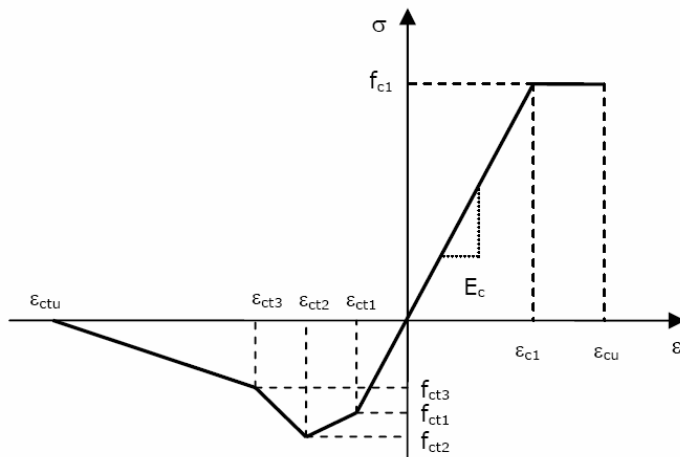


Figure 10-8: Stress-strain diagram for UHPC with strain hardening (Den Hollander, 2006)

The corresponding values of the stress-strain diagram are given in Table 10-3 and will be explained below.

Material property	Symbol	Value
Characteristic value compressive strength	f_{ck}	-200 MPa
Design value compressive strength	f_{c1}	-120 MPa
Design value tensile strength at point t_1	f_{ct1}	+8 MPa
Design value tensile strength at point t_2	f_{ct2}	+9 MPa
Design value tensile strength at point t_3	f_{ct3}	+5 MPa
Yield compressive strain	ϵ_{c1}	-1.75 ‰
Ultimate compressive strain	ϵ_{cu}	-3.00 ‰
Ultimate tensile strain	ϵ_{ctu}	+10.00 ‰
Specific weight	ρ_c	28 kN/m ³
Young's modulus	E_c	55000 MPa

Table 10-3: Material properties for the applied UHPC mixture

The simulations are done without material safety factors, in order to give the best possible impression of the truth.

The crack widths corresponding with the points ϵ_{ct2} and ϵ_{ct3} are respectively $w_2 = 0.16$ mm at point t_2 and $w_3 = 1.0$ mm at point t_3 . Usually, a UHPC mixture contains two kinds of fibres, namely, micro fibres and "normal" fibres. The "normal" fibre length is decisive for the ultimate tensile strain. A length of 50 mm is assumed for the "normal" fibre.

The tensile strain of the concrete at point t_1 , where the linear elastic behaviour of the concrete ends, is calculated as:

$$\epsilon_{ct1} = \frac{f_{ct1}}{E_c} = \frac{8.0}{55000} = 0.0001455$$

The tensile strain of the concrete at point t_2 is calculated as:

$$\epsilon_{ct2} = \frac{w_2}{l_c} + \epsilon_{ct1} = \frac{0.16}{83.044} + 0.0001455 = 0.002072$$

The tensile stress of the concrete at point t_3 is calculated as:

$$\epsilon_{ct3} = \frac{w_3}{l_c} + \epsilon_{ct1} = \frac{1.0}{83.044} + 0.0001455 = 0.01219$$

The ultimate tensile strain of the concrete is calculated as:

$$\epsilon_{ctu} = \frac{l_f}{4l_c} = \frac{50}{4 * 83.044} = 0.150523$$

The above calculated values are summarized in Table 10-4. Normally, DIANA considers only the parts of the stress-strain curve with a negative slope as cracking. So the hardening part of the UHPC curve is not considered as cracking. In reality, the hardening

part cracking and stiffening due to micro fibres. Therefore, an extra point (f_{ct1*} ; ϵ_{ct1*}) is added, to let DIANA consider the softening from this point.

Point	Stress	Strain
f_{ct1} ; ϵ_{ct1}	8.00	0.0001455
f_{ct1*} ; ϵ_{ct1*}	7.99	0.000146
f_{ct2} ; ϵ_{ct2}	9.00	0.002072
f_{ct3} ; ϵ_{ct3}	5.00	0.01219
f_{ctu} ; ϵ_{ctu}	0	0.150523

Table 10-4: Stress and strain values for implementation in the DIANA model

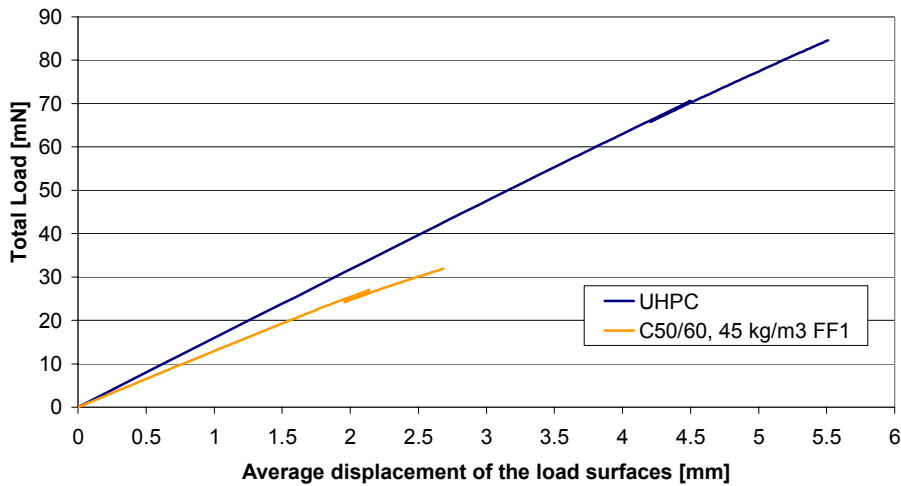


Figure 10-9: Total load vs. average displacement of the loading surfaces for UHPC and C50/60 with 45 kg/m³ FF1 steel fibres

The ultimate load of the analysis with UHPC is approximately 85 mN. This is 2.66 times the ultimate load of the earlier analysed segment with C50/60 concrete and 45 kg/m³ FF1 steel fibres. The crack pattern at ultimate load is displayed in Figure 10-10. This figure shows a very fine, widely distributed crack pattern.

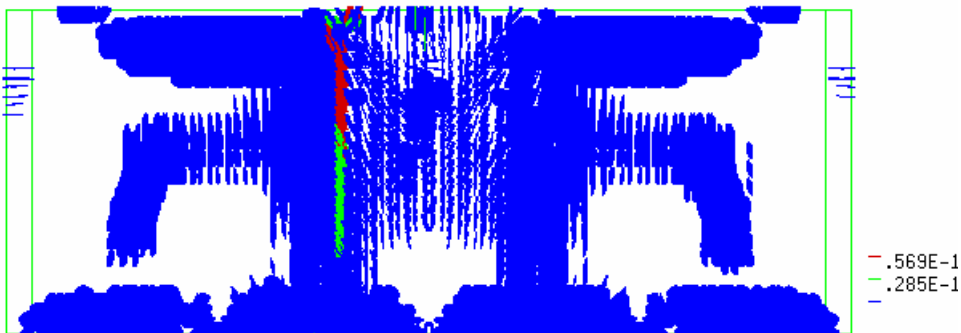


Figure 10-10: Total load vs. average displacement of the loading surfaces for UHPC and C50/60 with 45 kg/m³ FF1 steel fibres

The crack width at ultimate load mN is 7.1 mm. At a total load of 68.6 mN the maximum crack width is 2.375, which is approximately the same crack width as the analysis of the C50/60 concrete with 45 kg/m³ FF1 steel fibres at a total load of 24.3 mN. The load on which this crack width occurs for UHPC is 2.82 times as high as the load of the C50/60 concrete with 45 kg/m³ FF1 steel fibres.

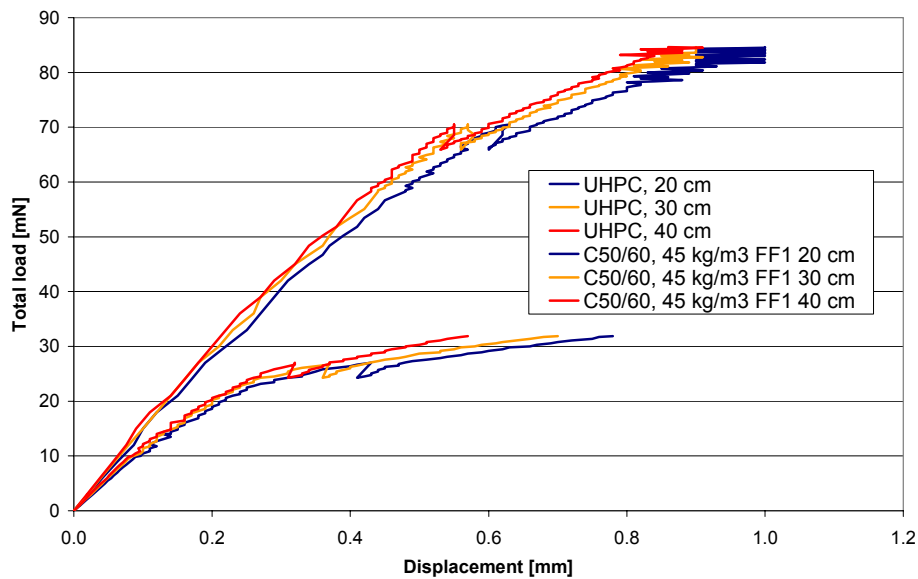


Figure 10-11: Total load vs. relative displacement in the bursting zone for UHPC and C50/60 with 45 kg/m^3 FF1 steel fibres

The comparison of the two types of concrete in the bursting zone is displayed in Figure 10-11. It shows that there is hardly nonlinearity until 70 mN in the UHPC analysis. This means that there are hardly cracks until this load level.

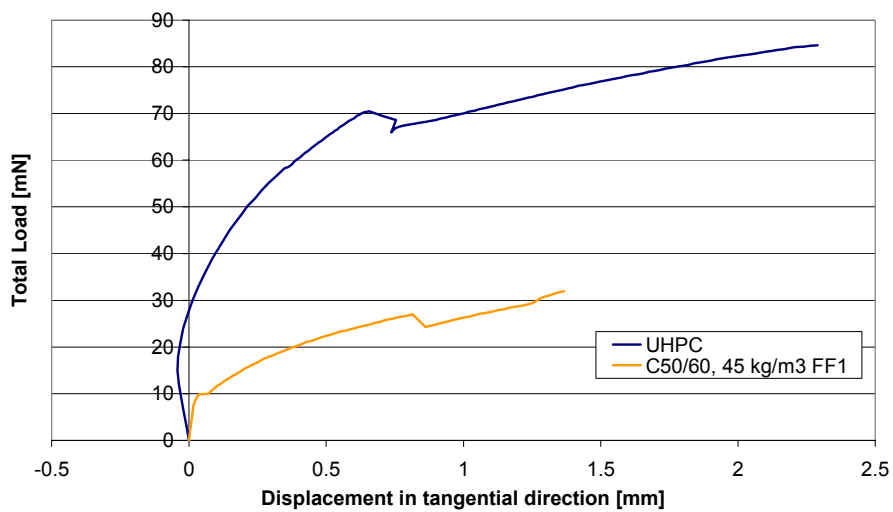


Figure 10-12: Total load vs. relative displacement in the spalling zone for UHPC and C50/60 with 45 kg/m^3 FF1 steel fibres

The spalling zone shows a stiff behaviour until 70 mN too. After this load level, a sudden change of slope occurs.

11 Alternative thrust jack configurations

There are three thrust jack configurations that are generally applied: The German (Figure 11-1), the French (Figure 11-2) and the Japanese (Figure 11-3) thrust jack configuration. The configuration which is applied in the Barcelona line 9 metro tunnel is a combination of the Japanese (support side) and the French (thrust jack side) configuration.

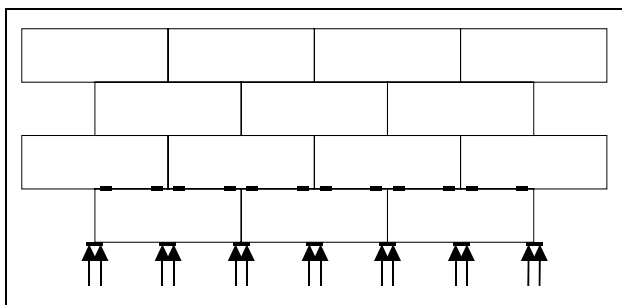


Figure 11-1: Layout of the German configuration (Slenders, 2002)

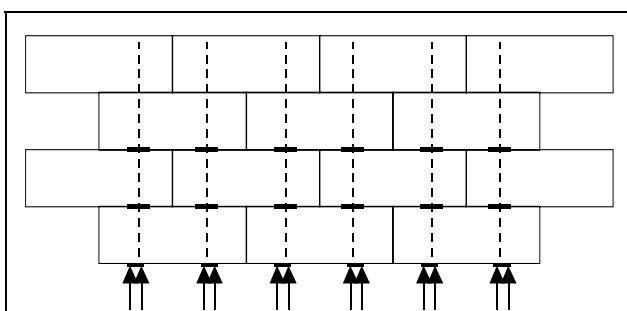


Figure 11-2: Layout of the French configuration (Slenders, 2002)

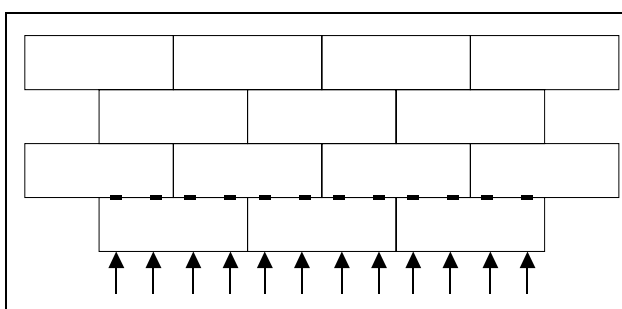


Figure 11-3: Layout of the Japanese configuration (Slenders, 2002)

The Japanese configuration has the advantage that the thrust jack load is equally distributed over the segment, which leads to a higher ultimate load in the normal loading case. The disadvantage of this configuration is that, when the ring joint is not smooth, the support can be partly missing. The last mentioned case can not happen in the French configuration, because it has only two support surfaces, which will always touch the adjoining ring. The disadvantage of the French configuration is that the load is more concentrated, because there are only two load surfaces. The German configuration has a concentrated distribution of the thrust jack forces and the possibility of a missing support. Therefore, when it comes to stresses due to thrust jack forces, no advantages are

expected by this configuration with respect to the others. So this configuration is not considered.

The above mentioned advantages and disadvantages of the French and the Japanese thrust jack configuration are studied in this chapter. The influence of extra stress concentrations due to eccentricity and inclination is studied in the French thrust jack situation, because this configuration is sensitive for stress concentrations. Simulations with missing supports are made for the Japanese configuration, because this is a reasonable situation to occur in this configuration.

11.1 Japanese thrust jack configuration

11.1.1 The normal loading situation

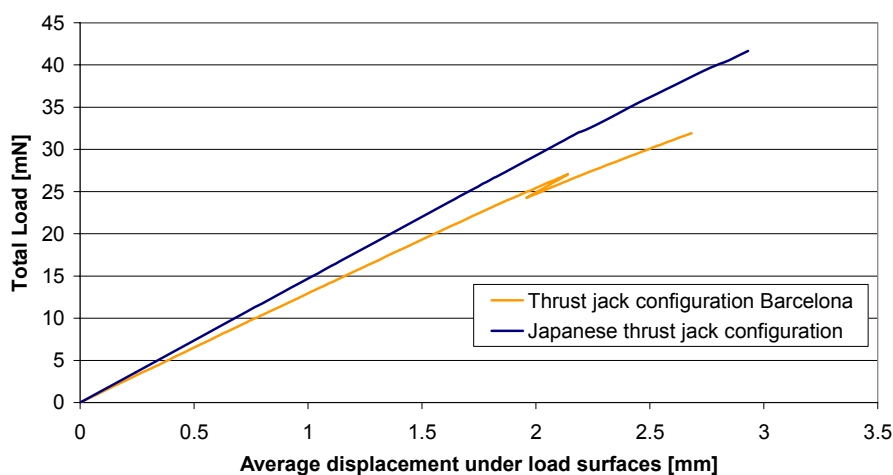


Figure 11-4: Load displacement curves of the normal loading situation for the Barcelona and the Japanese thrust jack configuration

A significantly higher ultimate load is reached when the Japanese thrust jack configuration used. Figure 11-4 shows an ultimate load of 41.6 mN, whereas the Barcelona thrust jack configuration reaches only 30.7 mN.

This is because the thrust jack load is more equally distributed over the segment and the sum of the thrust jack surfaces is larger. This is clearly visible in Figure 11-5. The crack maximum crack width at ultimate load is 0.58 mm, which is much smaller than in the Barcelona configuration (4.45 mm). The analysis probably stops by failure in compression on the load surfaces, because the load pressure is then 59.3 MPa. This is not exactly clear, because the compression stress could be higher than the compression strength when confinement is applied. It is hard to determine if the lateral stresses are sufficient to supply confinement.

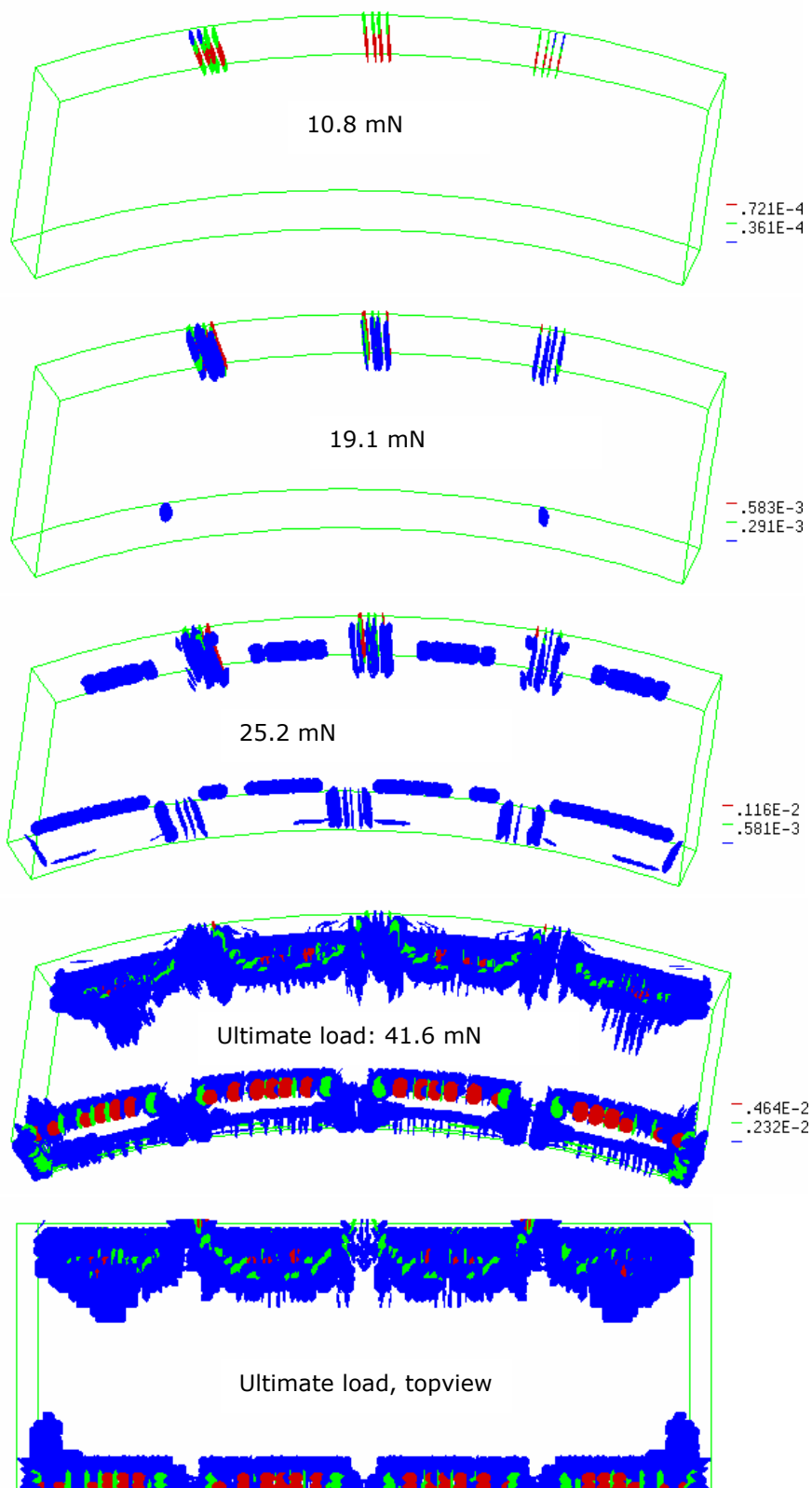


Figure 11-5: Crack development displayed by crack patterns

11.1.2 Missing support at the side of the segment

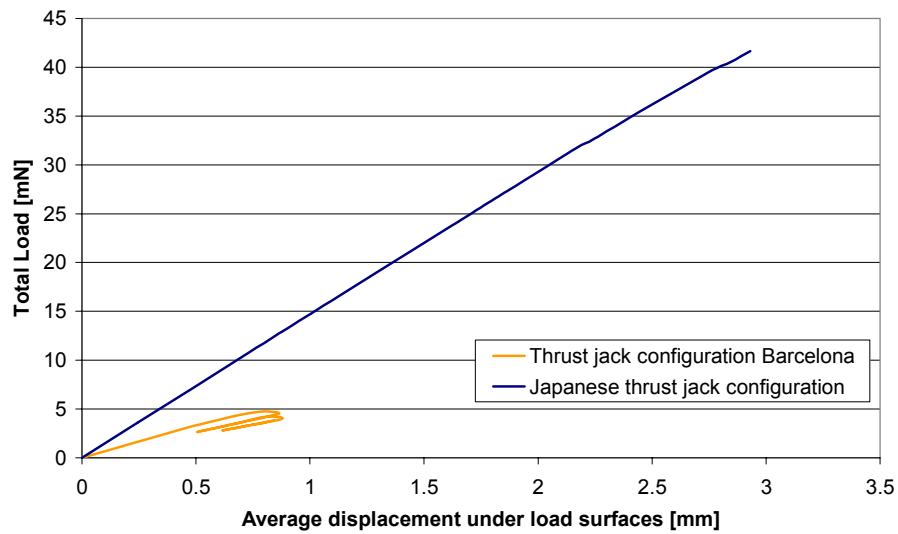


Figure 11-6: Load displacement curves of the normal loading situation for the Barcelona and the Japanese thrust jack configuration

When a missing support at the side is applied, a similar as in the normal loading situation occurs. This is visible in Figure 11-6. The crack pattern, which is displayed in Figure 11-7, shows a mayor crack between near the missing support.

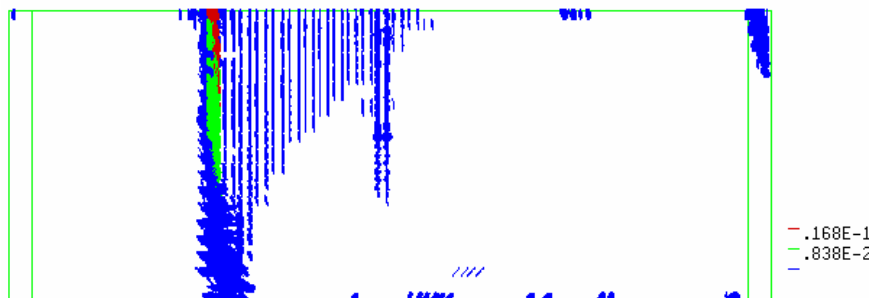


Figure 11-7: Crack pattern at ultimate load

The ultimate load is 4.74 mN. The displacement is then 2.1 mm. It is reasonable to assume that the in practice occurring non-smoothness of the ring joint can be larger than this displacement. The left part of Figure 11-7 will then rotate downwards until the support is touched.

11.2 The French thrust jack configuration

11.2.1 The normal loading situation

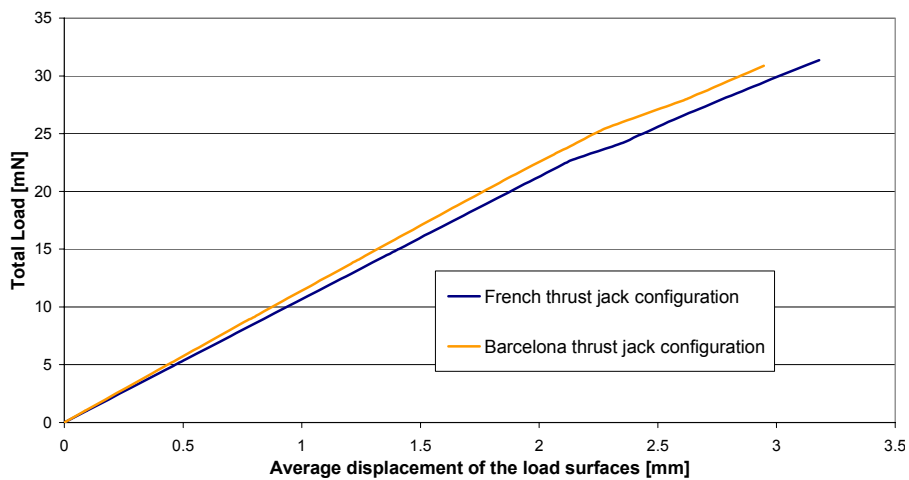


Figure 11-8: Load-displacement curves of the French and the Barcelona thrust jack configuration

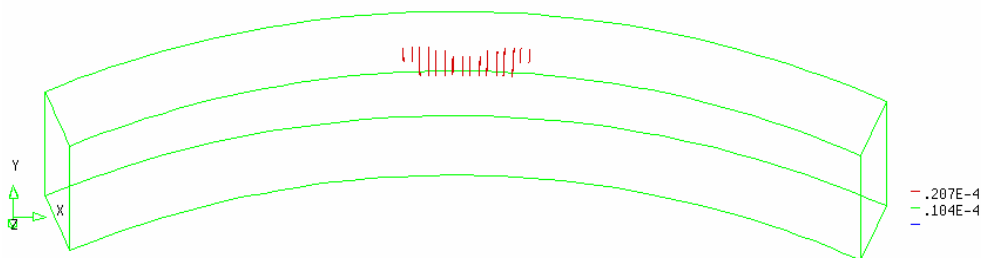


Figure 11-9: First crack: spalling cracks between the thrust jacks

Like in the analysis in Section 9.2, the first crack appears between the thrust jacks. The cracks appear at a load of 8.98 mN (Figure 11-9), which is higher than in Section 9.2 (6.0 mN). This is because the load is in line with the supports, so there do not appear extra tension stresses in this zone due to the earlier explained effects of outward tilting.

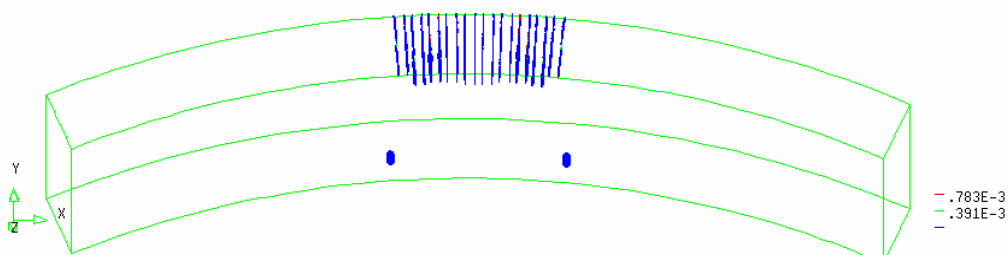


Figure 11-10: Second crack: near the supports at 12.9 mN

Cracks appear near the support surfaces at a load of 12.9 mN. This is slightly higher than in Section 9.2 (14.5 mN), because the stress concentrations are higher with two support surfaces.

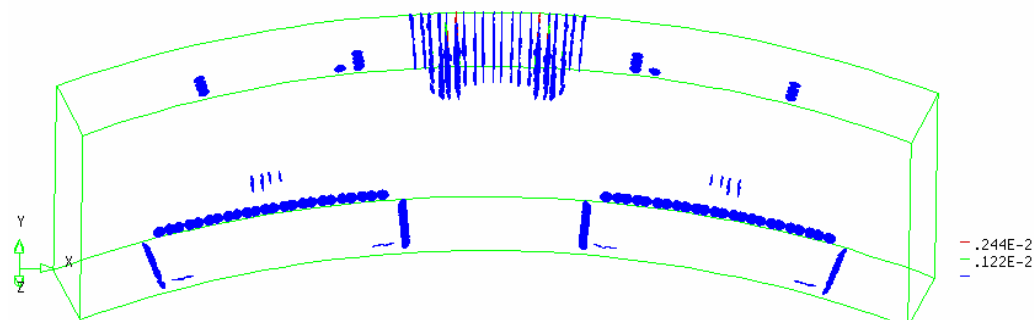


Figure 11-11: Third crack: radial and tangential bursting cracks 20.4 mN

Bursting cracks start to develop at a load of 20.4 mN. They do not only appear near the thrust jack plate, due to radial stresses, but also in the middle of the segment, due to tangential stresses.

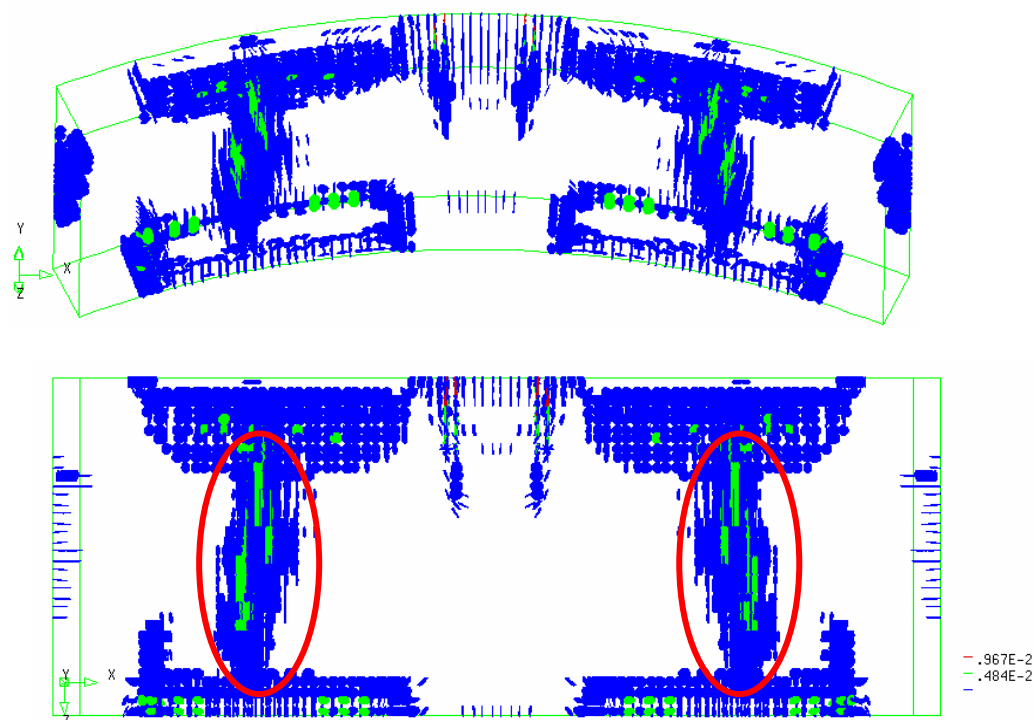


Figure 11-12: Crack pattern at ultimate load

The analysis reaches an ultimate load of 31.4 mN. This is approximately the same as in Section 9.2. An important difference is that the spalling crack between the thrust jacks does not penetrate deeply into the structure.

Furthermore, there occur tangential bursting cracks over a large part of the depth of the segment. These cracks are elucidated by the red ellipses in Figure 11-12. The reason that these cracks do not occur in the Barcelona thrust jack configuration, and do occur here is the difference in support. Every load surface corresponds with two support surfaces in the ring joint in the Barcelona thrust jack configuration. This situation can be schematised as the left image of Figure 11-13, as a concentrated load on a relatively equally distributed support. The right image of Figure 11-13 displays the situation of the French thrust jack configuration, in which as well the load as the support is concentrated. This causes tensile stress trajectories from both sides of the segment. The disturbed zone spreads over a

depth h , see Figure 11-13, which is the width of the compressed member. In case of the tunnel segment, h is approximately 2300 mm and the depth is 1800 mm.

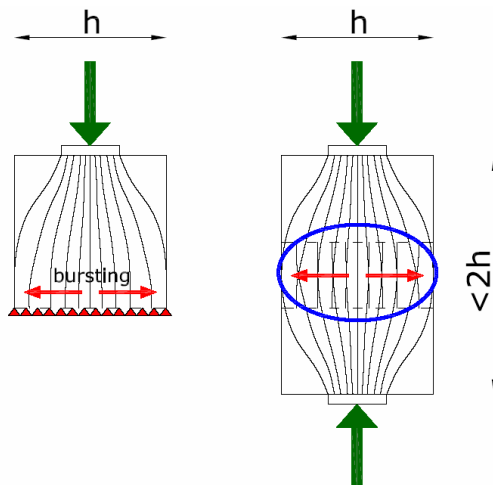


Figure 11-13: Development of bursting stresses

This means that, if the segment is compressed from both sides, the disturbed zones from both the load and the support side overlap. This is displayed by the blue ellipse in Figure 11-13. The bursting stresses in this region are accumulated.

11.2.2 Eccentricity or inclination of the thrust jack

Load situation	Ultimate load French configuration [mN]	Ultimate load Barcelona configuration [mN]
Normal load situation	31.4	30.7
Eccentricity outside	23.1	23.6
Eccentricity inside	23.5	24.0
Inclination outside	16.0	20.0
Inclination inside	17.7	20.4

Table 11-1: Ultimate loads for different load situations

The French configuration is slightly more sensitive for eccentricity and inclination of the thrust jacks. This can be explained by the fact that the distance between the upper and the lower point of the support (Figure 11-14) is smaller in this configuration in comparison to the Barcelona (and Japanese) configuration.

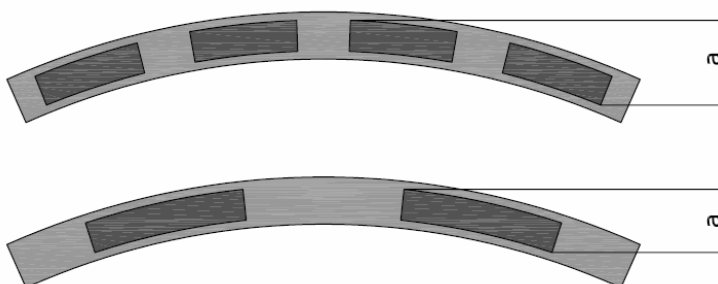


Figure 11-14: Difference in distance between the upper and the lower edge of the support

The smaller distance a in Figure 11-14 causes smaller resistance against tilting. Therefore, the deformations and the stress concentrations are larger.

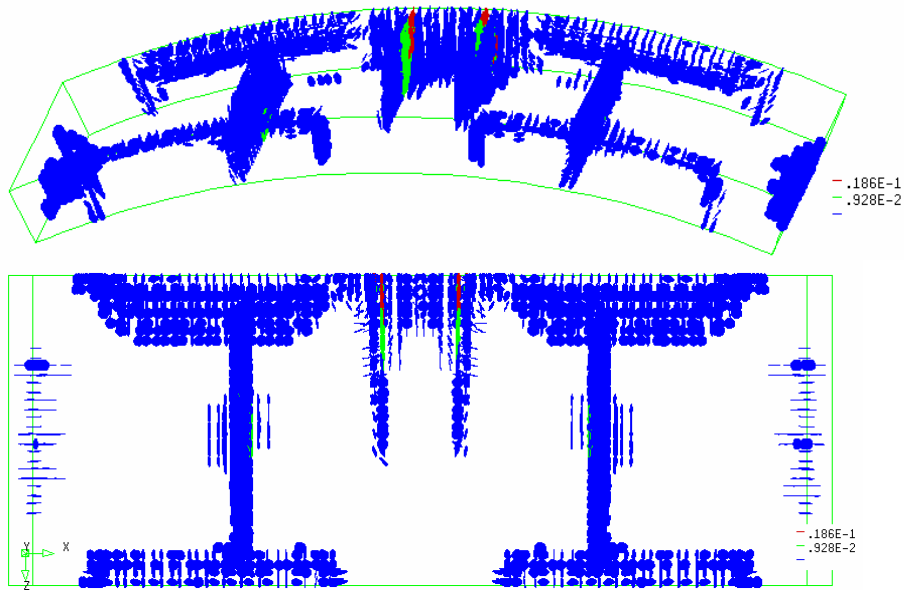


Figure 11-15: Crack pattern of the simulation with eccentricity outside at ultimate load

The analysis with eccentricity stops at a load of 23.1 mN. This is probably due to the increased bursting stresses on the outside of the segment (Figure 11-15). When eccentricity inside is applied, the tangential bursting stresses increase at the inside of the segment. This is visible in Figure 11-16.

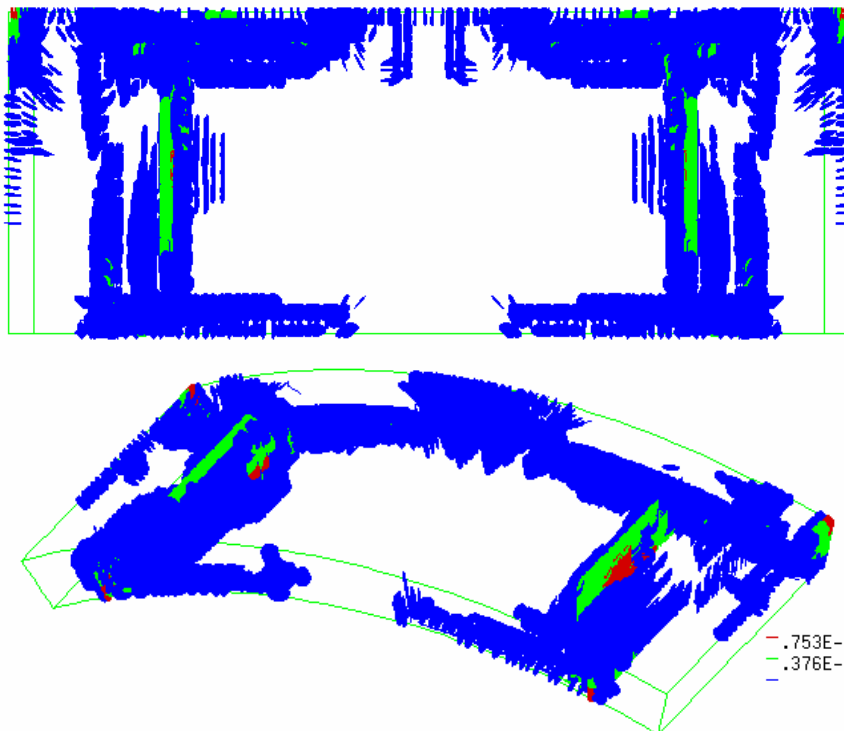


Figure 11-16: Crack pattern of the simulation with eccentricity inside at ultimate load

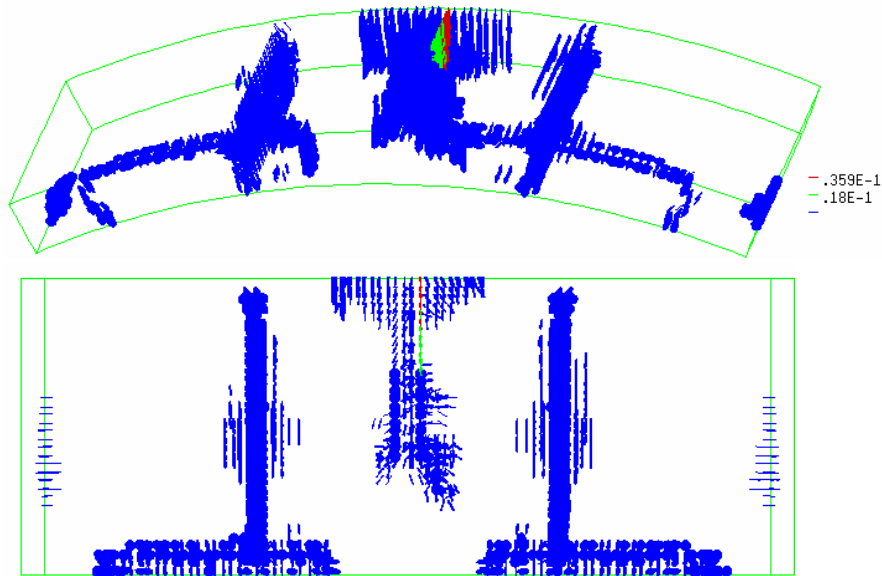


Figure 11-17: Crack pattern of the simulation with inclination outside at ultimate load

When inclination outside is applied, the segment tilts outward, which causes increased support stresses on the centre sides of the support surfaces. Therefore, the tangential bursting cracks occur more on the centre sides of these surfaces and lead to failure at a lower load level than in the normal loading situation.

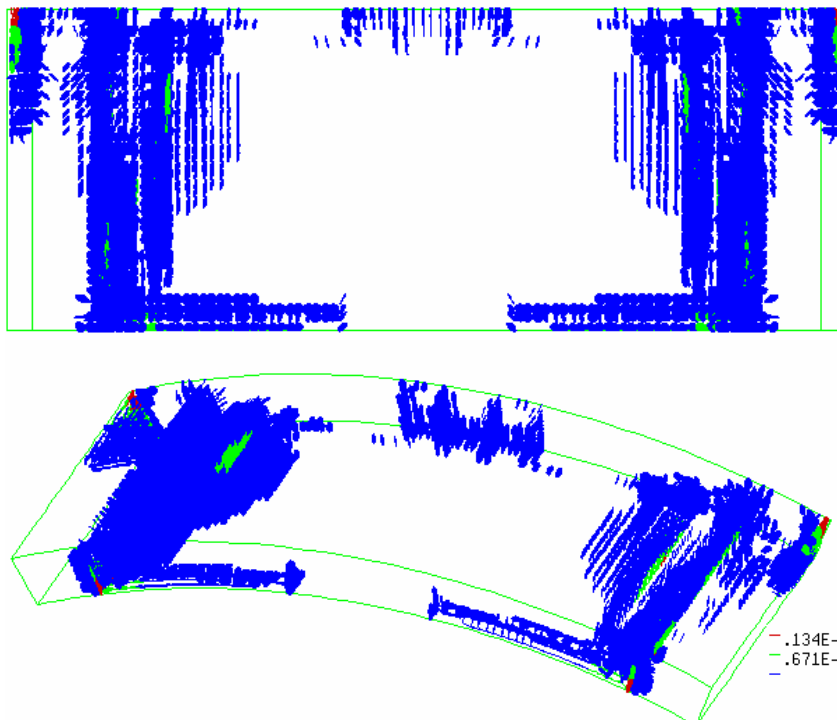


Figure 11-18: Crack pattern of the simulation with inclination inside at ultimate load

The analysis with inclination inside (Figure 11-18) stops at 17.7 mN. The traction inside and the lateral supports cause a bending moment, which causes the collapse. This can best be explained by the deformed shape, which is presented in Figure 11-19. The traction inside causes an out of plane bending moment. The segment deforms in such a

way that it becomes less curved. Together with the tangential bursting stresses, this bending moment leads to failure.

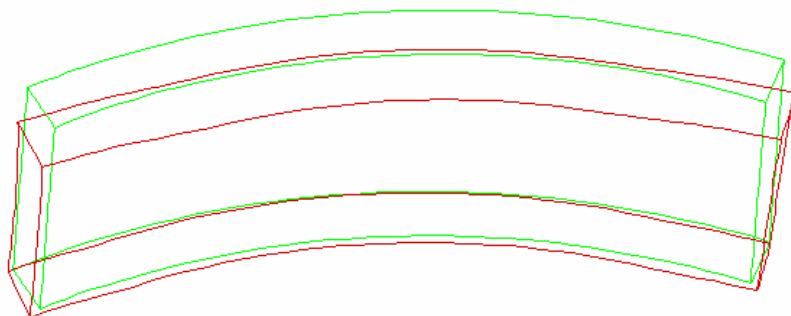


Figure 11-19: Deformed shape of the simulation with inclination inside at ultimate load

11.3 Conclusions with respect to the segment analyses

11.3.1 Conclusions with respect to the application of SFRC in tunnel segments

Even though the crack widths are not all realistic and the analyses are numerically not very stable, the non-linear analyses in Chapter 9 show reasonable results. This chapter gives some possible explanations of the cracks occurring in practice.

Steel fibres reduce the crack widths in steel fibre reinforced tunnel segments. Especially when 60 or 75 kg/m³ of steel fibres is applied, the crack widths decrease significantly. While the ultimate load of a tunnel segment in C50/60 concrete with low amounts of fibres is limited by cracking, the compressive strength is the limiting factor when higher amounts of fibres are applied.

Because of its high compressive and tensile strength and large toughness, a tunnel segment of UHPC can be subjected to very high thrust jack forces and only small cracks occur. Using this material, the lining thickness can be reduced significantly, with respect to the thrust jack forces.

Eccentric or inclined placement of the thrust jack causes higher stresses. The ultimate load reduces significantly and large crack widths occur when these errors in placement are present. When errors in placement can be assured to be small, it is possible to reduce the lining thickness.

A non-smooth support of the ring joint should be mitigated, because this situation causes very high stresses in the segment. These stresses cannot be carried by steel fibres, neither by reinforcement bars.

11.3.2 Conclusions with respect to the thrust jack configuration

The stress distribution is the most equal in the Japanese configuration, so this configuration results in the highest ultimate load. A non-smooth support in the ring-joint gives large cracks in this configuration. When this situation can be avoided, the Japanese configuration is the best option. With respect to thrust jack action, the lining thickness this configuration can be smaller than in the other configurations.

The French configuration has a lower ultimate load, but has no (or less) problems when it comes to a non-smooth support. When an accurate placement and limited deformations during the grout phase can not be expected, this configuration is the best option.

12 General conclusions and future perspectives

12.1 Conclusions

The goal of this study was to study the behaviour of steel fibre reinforced tunnel segments in the assembly phase. Due to the fact that the modelling of concrete cracking in a FEM program is much more complex than was expected, this goal has not been completely fulfilled. It took a lot of time to gain insight into the functioning of the material models, in theory and in practice. Therefore, there was no time to do all the planned simulations. The influence of the irregularities (bolt holes, grout hole and erector holes) in the segment and the torsional deformation due to the grout pressure have not been studied. It should be noted that the definition of a complex model, like a tunnel segment with irregularities, in the DIANA graphical user interface costs a lot of time. It is advisable to define the mesh-model in a different way and then implement it in DIANA, but this is not studied in this thesis. Furthermore, the combination of thrust jack action and torsional deformation requires a phased analysis. This will probably give unrealistic results using the Total Strain rotating crack model. So other ways must be found to model this situation.

The conclusions with respect to the material models are given in Section 7.4 and the conclusions with respect to the segment analyses are given in Section 11.3. The most important ones are summarised below.

12.1.1 *Conclusions with respect to the material models:*

Multi-axial post cracking behaviour

While the Concrete Damaged Plasticity model approaches the real behaviour of concrete the best, it fails in a multi-axial stress state. This is because the scalar damage factor, which multiplies the total stiffness matrix by a factor smaller than one. The constitutive law shows the same softening relation in all directions, which is completely different from the real behaviour of concrete. In a uni-axial stress state, this difference is not experienced, because there is no stress in the directions tangential to the crack. Therefore, the concrete damaged plasticity gives a good result in the simulation of the four-point-bending-test. When it comes to the splitting test with a line load, the concrete damaged plasticity model does not give good results. This is because there is a bi-axial stress situation in this case. There is a compressive stress in the direction of the load and a tensile splitting stress perpendicular to the load-direction. Whereas only the stiffness in the direction perpendicular to the load-direction is multiplied by a softening function in a crack model, all terms of the stiffness matrix are multiplied by the degradation factor in the Concrete damaged plasticity model. The result is softening in the direction of the load, which is in reality not present. Therefore, the Concrete Damaged Plasticity model is not suitable to model concrete cracking in a multi-axial stress state.

The smeared cracking models all have orthotropic softening and are therefore suitable to model a multi-axial stress state. The Drucker/Prager + multi directional fixed crack model has the advantage of choosing between a constant and a linear tension cut off. The linear tension cut off is a safe approach and the constant tension cut off is an unsafe approach. The reality is in-between constant and linear tension cut off.

Numerical stability

When the material models are subjected to analyses, it becomes clear that the shear retention factor, which is present in the Total Strain fixed crack model and the

Drucker/Prager + multi directional fixed crack model, causes problems. The numerical stability increases when an increased value of β is used, but at the same time the approximation becomes worse when β is increased. The use of a material model in which β is present leads either to a bad approximation or numerical difficulties. The Total Strain rotating crack model does not have this problem, because with the rotating crack principle there cannot occur shear stresses along the crack.

Total Strain rotating crack

The Total Strain rotating crack model is a simple model. It is not close to the real behaviour of concrete, because the principle stress directions are uncoupled and the cracks can rotate during the analysis. The simplicity of this model is at the same time a large advantage. It makes the model numerically much more stable than the other mentioned models. The numerical stability is a very important feature of a material model, because instable models take a lot of time from the engineer. The rotations of the cracks are in most cases very small, so they have only little influence on the behaviour of the analysis. The uncoupling of the principle stress directions makes the tension-compression (or tension-tension-compression in 3D) behaviour stronger than the real behaviour of concrete, but, looking at the analyses of the experiments, this seems to have only small influence.

The Total Strain rotating crack model is suitable to model SFRC in a uni-axial and multi-axial stress state. The model is understandable and numerically stable. The model does not give a very close approximation of the real behaviour of concrete, but the approximation is reasonable and in most cases crack simulations are used to show differences and principles, not design calculations.

The limitation of the Total Strain rotating crack model is that large rotations cause an unrealistic behaviour. This makes it impossible to do an analysis in which different loading cases are put subsequently on the mesh-model (phased analysis).

12.1.2 Conclusions with respect to the application of SFRC in tunnel segments:

Even though the crack widths are not all realistic and the analyses are numerically not very stable, the non-linear analyses in Chapter 9 show reasonable results. This chapter gives some possible explanations of the cracks occurring in practice.

Steel fibres reduce the crack widths in steel fibre reinforced tunnel segments. Especially when 60 or 75 kg/m³ of steel fibres is applied, the crack widths decrease significantly. While the ultimate load of a tunnel segment in C50/60 concrete with low amounts of fibres is limited by cracking, the compressive strength is the limiting factor when higher amounts of fibres are applied.

Because of its high compressive and tensile strength and large toughness, a tunnel segment of UHPC can be subjected to very high thrust jack forces and only small cracks occur. Using this material, the lining thickness can be reduced significantly, with respect to the thrust jack forces.

Eccentric or inclined placement of the thrust jack causes higher stresses. The ultimate load reduces significantly and large crack widths occur when these errors in placement are present. When errors in placement can be assured to be small, it is possible to reduce the lining thickness.

A non-smooth support of the ring joint should be mitigated, because this situation causes very high stresses in the segment. These stresses cannot be carried by steel fibres, neither by reinforcement bars.

12.1.3 Conclusions with respect to the thrust jack configuration

The stress distribution is the most equal in the Japanese configuration, so this configuration results in the highest ultimate load. A non-smooth support in the ring-joint gives large cracks in this configuration. When this situation can be avoided, the Japanese configuration is the best option. With respect to thrust jack action, the lining thickness this configuration can be smaller than in the other configurations.

The French configuration has a lower ultimate load, but has no (or less) problems when it comes to a non-smooth support. When an accurate placement and limited deformations during the grout phase can not be expected, this configuration is the best option.

12.2 Future perspectives

Numerical approximation of concrete cracking has not been developed very deeply. There are a few shortcomings on the present material models for concrete cracking. The most important ones are following:

- *Improve the stability of the material models.* The numerical stability is poor for all material models for concrete cracking. This makes an analysis with concrete cracking a time-consuming job. For most engineering companies this is a reason not to do non-linear analyses on concrete structures.
- *Make the behaviour of the material models more similar to the real behaviour of concrete.* The approximation of the Total Strain rotating model is not very close to the real behaviour of concrete. Therefore a certain error in approximation must be expected. This point of interest can be combined with the previous one by developing a new material model, or modifying the Concrete Damaged Plasticity model in such a way that it is stable and shows orthotropic softening.
- *Find a way to make a stable phased analysis.* The Total Strain rotating crack model, which is the most stable model (or least instable model), may give unrealistic results in a phased analysis. This is because the rotations of the cracks may be large in this situation.
- *Make the crack development and crack widths in the model more reliable.* The information about the crack widths and the number of cracks is not very reliable in the present models. Often two numerical cracks must be interpreted as one crack in reality and cracks may open and close during the analysis.

The advantage of the addition of steel fibres in tunnel segments has been proven with respect to the thrust jack phase. Though, there are other points of interest that must be studied in order to conclude if the addition of steel fibres is advantageous for tunnel segments. Important points of interest are:

- *Study the grout phase and the serviceability stage.* This thesis studies only the thrust jack phase. The other two important load situations should also be studied if steel fibre concrete is advantageous.
- *Study the fire safety.* The fire safety is important in tunnels. The fire resistance of the material determines the costs of the fire resistant cover at the inside of the tunnel.
- *Study the economical advantages and disadvantages.* Steel fibre reinforced concrete might be more expensive than traditional reinforced concrete, but, with

respect to the thrust jack forces, the lining thickness can be reduced. A reduction of the lining thickness does not only lead to a reduction of the required volume of concrete, but also leads to several secondary cost reductions, like transportation costs and excavation costs. A comparative study should be carried out in order to know if SFRC is an economical alternative.

- *Verify the behaviour of SFRC in tunnel segments by simplified design models.* The results of this study should be checked by design models and these models could be modified in order to utilize the favourable properties of SFRC in the design.

Literature

- [1] ABAQUS User's manual
- [2] Bekaert N.V. S.A., *Manual industrial floor slabs in steel fibre reinforced concrete* (in Dutch), Zingem, 1996
- [3] Bloemhof, K.C., Geometrical tunnel model; *Damages on a shield tunnel* (in Dutch), Delft, 2001
- [4] Bloemhof, K.C., Literature survey; *Damages on a shield driven tunnel* (in Dutch), Delft, 2001
- [5] Blom, C.B.M., Design philosophy of concrete linings for tunnels in soft soils, Delft, 2002
- [6] De Borst, R and Sluys, L.J. *Computational methods in non-linear solid mechanics*, Delft 2002
- [7] Burgers, R.A. *Literature survey*, Delft, 2006
- [8] Collins, M and Mitchell D., *Prestressed concrete structures*, Toronto, 1997
- [9] DIANA User's manual, Delft 2005
- [10] EuroCode 2, European standard with guidelines and rules for the calculation of concrete structures
- [11] Haring, F.P., Literature survey; *Stresses in assembly phase and serviceability phase of shield driven tunnels* (in Dutch), Delft, 2002
- [12] Haring, F.P., Main Report; *Stresses in assembly phase and serviceability phase of shield driven tunnels* (in Dutch), Delft, 2002
- [13] Den Hollander, J., *Technical Feasibility Study of a UHPC Tied Arch Bridge*, Delft, 2006
- [14] Kooiman, A.G., Literature survey steel fibre reinforced concrete in tunnel linings (in Dutch), Delft, 1997
- [15] Kooiman, A.G. , *Modelling of steel fibre reinforced concrete for structural design*, Delft, 2000
- [16] NEN 6720, *Design codes for concrete structures* (in Dutch)
- [17] Rots, J.G., *Comparative study of crack models*, Delft 2002
- [18] Schnütgen, B and Erdem E., *Splitting of SFRC induced by local forces*, Bochum, 2000
- [19] Slenders, B.M.A., Literature survey; *Modelling of the assembly phase of shield driven tunnels* (in Dutch), Delft, 2002
- [20] Tiberti, G., *Precast tunnel segments in fibre reinforced concrete* (in Italian), Brescia, 2004
- [21] De Waal, R.G.A, *Steel fibre reinforced tunnel segments for the application in shield driven tunnels*, Delft, 1999